TẠP CHÍ KHOA HỌC
JOURNAL OF SCIENCE

CHUYÊN SAN KHOA HỌC TỰ NHIÊN VÀ KỸ THUẬT
ISSUE: NATURAL SCIENCES AND ENGINEERING

MỤC LỤC

Đánh giá khả năng hấp phụ khí H_2 và CO_2 trong MIL-88A-Fe bằng phương pháp mô phỏng Monte Carlo chính tắc lớn

Nguyễn Thị Xuân Huynh[1,*], Trần Thế Nam[1], Đỗ Ngọc Sơn[2]

[1]Khoa Khoa học Tự nhiên, Trường Đại học Quy Nhơn, Việt Nam
[2]Khoa Khoa học Ứng dụng, Trường Đại học Bách Khoa Tp. HCM, Việt Nam

TÓM TẮT

Hai trong những vấn đề mang tính toàn cầu đó là tìm ra nguồn năng lượng mới, sạch thay thế cho nhiên liệu hóa thạch ngày càng cạn kiệt và khắc phục vấn đề ô nhiễm môi trường, biến đổi khí hậu ngày càng trầm trọng. Để góp phần khắc phục những vấn đề trên, trong những năm gần đây, lớp vật liệu khung hữu cơ kim loại được chú ý cho ứng dụng lưu trữ năng lượng như khí H_2 và bắt giữ khí thải như CO_2 dựa trên cơ chế hấp phụ. Trong lớp vật liệu khung hữu cơ kim loại, MIL-88A-Fe được đánh giá là rất bền trong môi trường ẩm và có tính giãn nở và tính xốp cao. Chính vì những lí do đó, chúng tôi quan tâm đánh giá khả năng lưu trữ khí H_2 và bắt giữ khí CO_2 của MIL-88A-Fe bằng phương pháp mô phỏng Monte Carlo chính tắc lớn ở nhiệt độ 77 K và 298 K với vùng áp suất dưới 100 bar. Kết quả cho thấy cách thông số hóa trường một phần bằng cách kết hợp tính điện tích riêng phần bằng phương pháp DDEC cho tương tác tĩnh điện và chọn thông số trường lực phổ quát cho tương tác Lennard-Jones có thể giúp đánh giá nhanh và đáng tin cậy cho khả năng bắt giữ và lưu trữ khí của họ vật liệu xốp. Kết quả cũng cho thấy khả năng lưu trữ H_2 và bắt giữ CO_2 của MIL-88A-Fe theo dung lượng chưa cao lắm nhưng theo dung tích được đánh giá cao. Khí H_2 hấp phụ mạnh ở vị trí hốc của các O và Fe, trong khi đó CO_2 phân bố đều hơn trong chất hấp phụ.

Từ khóa: *MIL-88A-Fe, phương pháp Monte Carlo, lưu trữ hydrogen, bắt giữ CO_2, hấp phụ đẳng nhiệt.*

---

*Tác giả liên hệ chính.
Email: nguyenthixuanhuynh@qnu.edu.vn

Evaluation of H_2 and CO_2 adsorption into MIL-88A-Fe by Grand canonical Monte Carlo simulation

Nguyen Thi Xuan Huynh[1,*], Tran The Nam[1], and Do Ngoc Son[2]

[1]Faculty of Natural Sciences, Quy Nhon University, Vietnam
[2]Faculty of Applied Sciences, Ho Chi Minh City University of Technology, VNU-HCM, Vietnam

ABSTRACT

Two of the global issues are finding new, clean energy sources to replace increasingly exhausting fossil fuels and overcoming the problem of environmental pollution and climate change. In recent years, organic-metal framework series has been considered as a great candidate for H_2 storage and CO_2 capture to provide clean energy and reduce environmental pollution. Among them, MIL-88A-Fe has a stable and flexible structure in moist environments and high porosity. Therefore, in this research, hydrogen (H_2) storage and carbon dioxide (CO_2) capture capacities in MIL-88A-Fe were assessed quantitatively. By the grand canonical Monte Carlo simulation, the adsorption capacities of MIL-88A were elucidated via the adsorption isotherms, heats of adsorption at finite temperatures of 77 K and 298 K and pressures up to 100 bar. The results show that parameterizing force fields by combining DDEC method to calculate atomic partial charges for electrostatic interactions and the universal force field parameters for the Lennard-Jones interactions provide a quick and reliable method to evaluate gas capture and storage capacities of porous materials. The results also indicate that the abilities of H_2 storage and CO_2 capture of MIL-88A-Fe in gravimetric capacities were not very high; however, they were noticeable in volumetric uptakes. The hydrogen molecule is strongly adsorbed in the hollow positions of O and Fe atoms, while the CO_2 molecule is more evenly distributed in the sorbent.

Keywords: *MIL-88A-Fe, grand canonical Monte Carlo, Hydrogen storage, Carbon dioxide capture, adsorption isotherms.*

1. INTRODUCTION

As known, hydrogen gas (H_2) is an abundant, potential and clean energy source. Hydrogen storage is the key to the development of fuel cell technology to reach the DOE gravimetric and volumetric targets. Besides, the globally rapid industrial development has resulted in an increasing amount of toxic gases released into the environment; in which, CO_2 is the main ingredient causing the greenhouse effect and affecting global warming. Therefore, reducing the amount of toxic gas and developing hydrogen

storage technology to provide a clean energy source are two very urgent issues.

In recent years, the technology of gas storage, capture and separation based on the adsorption mechanism of porous materials, especially the metal organic-framework (MOF) materials have gained considerable attention. MOF series is a porous crystalline composed of two main components: (1) inorganic connectors such as metal ions, metal clusters and (2) organic linkers.[1,2] Therefore, MOFs have many outstanding features that are extremely high

---

Corresponding author.
Email: nguyenthixuanhuynh@qnu.edu.vn

specific surface areas, tunable functionalities, large pore sizes, and reversible gas adsorption-desorption. So far, thousands of MOF structures have been successfully synthesized; however, at ambient temperatures and pressures under 100 bar, a few MOFs have been evaluated for H_2 storage and CO_2 capture.

In many MOFs that have not yet been evaluated for H_2 storage and CO_2 capture, we pay attention to MIL-88A-Fe[3] (MIL = **M**aterials from **I**nstitut **L**avoisier) for the following reasons: (1) MOFs must be stable to avoid breaking down the structure in a humid environment. Compared to other MOFs, MIL-88A has strong durability and flexibility, swelling up to 85% of its original volume in solvents;[4] (2) MIL-88A-Fe contains unsaturated metal sites that is one of the most effective strategies to improve gas storage and capture at room temperature;[5–7] (3) Iron (Fe) is a common metal in nature, leading the low cost of this MOF compared to others.

2. CALCULATION METHODS

In order to evaluate the gas storage or capture capacity in porous materials, the grand canonical Monte Carlo (GCMC) technique was performed. This method allows the number of gas molecules entering freely to the rigid MOF during the simulation by the random insertion, deletion, translation, and rotation steps until the equilibrium system. In this work, the GCMC simulation was used to calculate the uptakes of H_2 and CO_2 adsorbed in MIL-88A-Fe through the RASPA simulation software package developed by Snurr group and published in 2014.[8] This software package supports for simulating adsorption and diffusion of molecules in flexible nanoporous materials. It used the newest algorithm for MD and MC simulations with many outstanding features that are: easy to use, simple inputs, diverse output with many different measurements and units to meet the needs of users; surveying the flexibility of the material according to the temperature and pressure. This software package can calculate the Coulomb

interaction by the Ewald summation method for non-orthorhombic unit cells. For these reasons, we use RASPA in this research.

GCMC simulations were performed under the constant condition for volume (V), temperature (T) and chemical potential (μ) (ie. μVT ensemble). The chosen temperatures are 77 K and room temperature (298 K) and pressure up to 100 bar. The simulation steps are 10^5 for equilibrium and 3×10^5 for MC cycles. The simulation box was repeated $3 \times 3 \times 2$ times the primary unit cell ($3 \times 3 \times 2 \times 68$ atoms = 1224 atoms). The interaction between the gas (H_2, CO_2) and MIL-88A-Fe for a pair of the unlike atoms i and j at distance r_{ij} was presented as follows:

$$U(r_{ij}) = U_{LJ}(r_{ij}) + U_{CL}(r_{ij}), \qquad (1)$$

where, the first term in the equation

$$U_{CL}(r_{ij}) = \frac{1}{4\pi\varepsilon_0} \frac{q_i q_j}{r_{ij}} \qquad (2)$$

describes the electrostatic interaction between pairs of the ith and j^{th} atoms, in which q_i is the ith atomic charge (Fe, O, C, H), calculated based on the DDEC (**D**ensity **D**erived **E**lectrostatic and **C**hemical net atomic charge) algorithm by DFT calculation (DFT stands for the density functional theory). This parameterization of the force field improves the accuracy of the Coulomb interaction between the gas and MOF. The electrostatic potential was computed according to the Ewald method with a cut radius of 12 Å. And the second term describes the Lennard-Jones (LJ) interaction.

$$U_{LJ}(r_{ij}) = 4\varepsilon_{ij}\left[\left(\frac{\sigma_{ij}}{r_{ij}}\right)^{12} - \left(\frac{\sigma_{ij}}{r_{ij}}\right)^6\right] \qquad (3)$$

The parameters ε_{ij} and σ_{ij} correspond to the LJ potential depth and diameter for each pair of atoms. These parameters were calculated by the Lorentz–Berthelot mixing rule:

$$\varepsilon_{ij} = \sqrt{\varepsilon_i \varepsilon_j}; \ \sigma_{ij} = \frac{1}{2}(\sigma_i + \sigma_j), \qquad (4)$$

where the parameters σ_i and ε_i for atoms of M-MIL-88A were taken from universal force

fields in the RASPA software, listed in Table 1. The cut-off radius of 12 Å was used for the LJ interactions.

A single LJ interaction site model at the center of mass (H_{com}) was used for the hydrogen molecule. Here, the LJ parameters were taken from the TraPPE force field[9] with $\sigma_{H_{COM}} = 2.96$Å, $\varepsilon_{H_{COM}}/k_B = 36.70$ K, and the H–H_{COM} bond length of 0.37 Å. The CO_2 molecule was utilized by the EPM2 model.[10] This force field parameterization above gives the results with high reliability.[11]

Table 1. LJ parameters and the DDEC partial atomic charges of the MIL-88A-Fe.

Atom	ε/k_B (K)	σ (Å)	Atomic charge (e)
Fe	6.54	2.59	1.22
C1	47.86	3.47	0.73
C2			-0.18
O1	48.16	3.03	-0.57
O2			-0.87
H	7.65	2.85	0.12

The atom types in Table 1 are classified based on their links to the other atoms in the MIL-88A-Fe unit cell consisting of 12 H atoms, 12 C1 atoms, 12 C2 atoms, 24 O1 atoms, 2 O2 atoms at the μ_3-O-centered trimer of Fe metals, and 6 Fe atoms. Figure 1 shows cut from the MIL-88A-Fe unit cell which the partial charges on the MOF calculated using the DDEC algorithm.
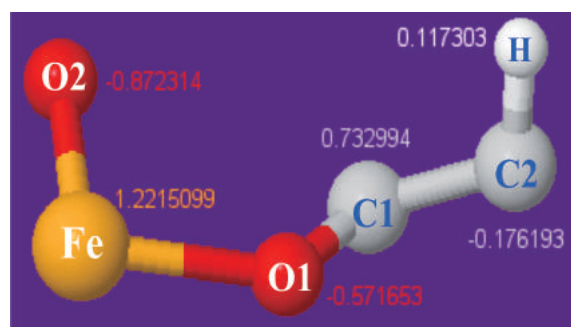

Figure 1. The partial atomic charges calculated using the DDEC method based on the density function theory.

3. RESULTS AND DISCUSSION

3.1. Optimization for MIL-88A-Fe structure

MIL-88A-Fe topology is shown in Figure 2. The unit cell of MIL-88A-Fe with the lattice constants of $a = b \neq c$ and the angles of $\alpha = \beta = 90^\circ$, $\gamma = 120^0$ is in the rhombus frame. After the unit cell was designed based on experimental data,[3] we relaxed all ions and volume of the MOF by using the van der Waals-density functional of Langreth group.[12]
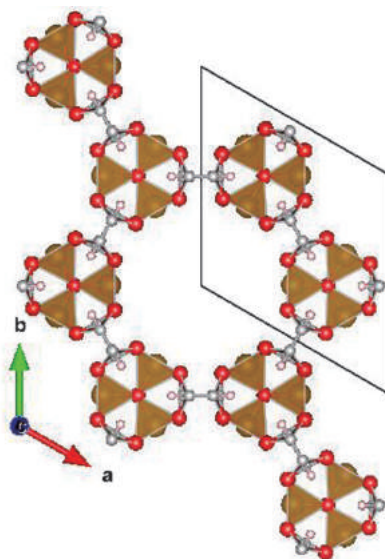

Figure 2. MIL-88A-Fe structure. The section in the frame is a primary unit cell. Brown, red, grey, white pink-coloured balls correspond to Fe, O, C and H atoms.

The unit cell was optimized based on the Murnaghan's equation of state[13] from the total energies calculated by DFT calculations. This approach was indicated in detail in our previous research[11] by changing various lattice constants. The result of fitting the lattice constants versus the total energy is listed in Table 2. From these minimum points of total energy, the values of c/a and a versus the energy is fitted again by Murnaghan method, we find the optimal value pair (c/a, a) for the unit cell that is $a = b = 11.22$ Å and $c = 14.86$ Å, leading to the volume of 1619 Å. This result is quite suitable with the experimental data[3] corresponding to the lattice parameters $a = b = 11.04$ Å and c = 14.80 Å as well as the volume size of 1562 Å.[3]

Table 2. The lattice constants and the minimum energy fitted based on the Murnaghan's equation of state corresponding to the determined values of c/a.

c/a ratio	Lattice constant, *a* (Å)	Minimum energy (eV)
1.25	11.46	-366.86
1.27	11.39	-367.41
1.29	11.32	-367.70
1.31	11.26	-367.88
1.33	11.19	-367.87
1.35	11.13	-367.76
1.37	11.08	-367.45
1.39	11.02	-367.02

3.2. H$_2$ storage capacity of MIL-88A-Fe

To quantitatively assess gravimetric and volumetric H$_2$ storage capability in MIL-88A-Fe, we determine the absolute and excess adsorption isotherms at two common temperatures of 77 K and 298 K according to the increasing pressure up to 100 bar. The results are shown in Figure 3 for gravimetric loadings (left y-axis) and volumetric loadings (right y-axis).

At 77 K (Figure 3a), both absolute and excess isotherms increase strongly at low pressure (below 5 bar) and then increase slowly with increasing pressure. The excess adsorption quickly reaches its saturation value of 4.06 wt% at 15 bar, then decrease slightly. Meanwhile, the total uptake still increases slightly, reaching 4.66 wt% at 100 bar. Remarkably, the total and excess volumetric H$_2$ adsorption capacities are very high, obtaining 44.32 g/L (at 15 bar) and 50.69 g/L (at 100 bar), respectively. At room temperature (Figure 3b), the H$_2$ adsorption capacity of MIL-88A-Fe increases almost linearly with pressure up to 100 bar, especially for the absolute uptake. The obtained results at 100 bar of total and excess storage capacities are 0.22 wt% and 0.63 wt% for gravimetric uptakes; 2.49 g/L and 6.97 g/L for volumetric uptakes. The above results show the noteworthy of the volumetric H$_2$ storage capacity of MIL-88A-Fe compared to the experimental results as well as other calculations.[14] The most noticeable MOF is the Be-BTB material[15] with the chemical

Be$_{12}$(OH)$_{12}$(benzene-1,3,5-tribenzoate)$_4$, which obtained 2.3 wt.% for and 1.01 wt.% for absolute and excess uptakes, while the total and excess volumetric capacities reached 44 g/L at (77 K, 100 bar) and 11 g/L at (298 K, 100 bar).
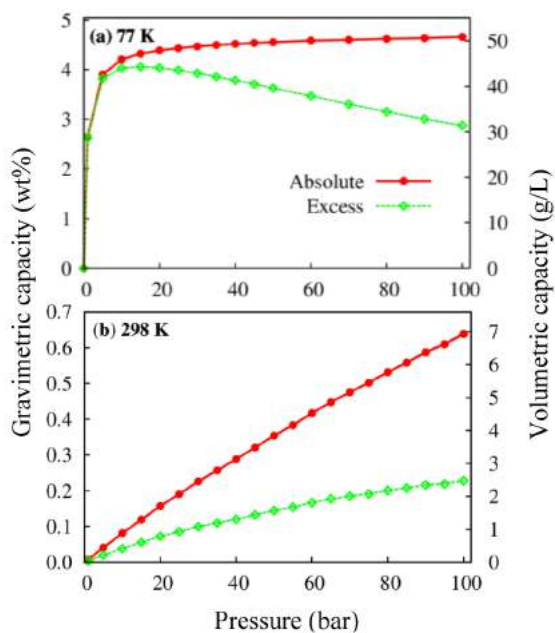
Figure 3. The absolute and excess H$_2$ adsorption isotherms in MIL-88A-Fe at 77 K (a) và 298 K (b), and the pressures up to 100 bar.

Deeper insights into the interaction strength between H$_2$ and MIL-88A-Fe were indicated via the heat adsorption (Q_{st}) of H$_2$ in MIL-88A-Fe at 77 K (Figure 4a) and 298 K (Figure 4b). The average value was calculated at the low-pressure area below 10 mbar with the obtained values of 7.38 kJ/mol at 77 K and 8.78 kJ/mol at 298 K.
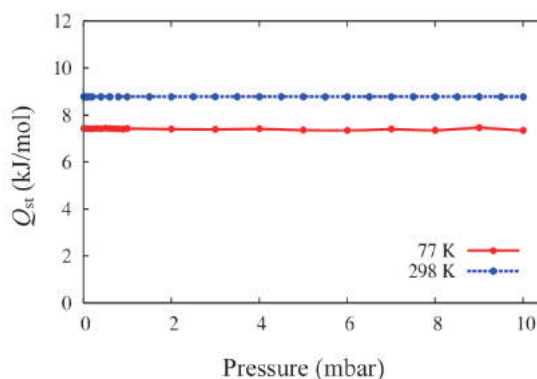
Figure 4. Isosteric heat of adsorption of H$_2$ in MIL-88A-Fe at temperatures 77 K and 298 K, the pressure below 10 mbar.

Figure 5 shows the visualization of the H_2 adsorption in MIL-88A-Fe. The figure indicates that H_2 molecules are preferable in the hollow than other sites of MIL-88A-Fe such as organic linkers or metal sites at both 77 K (Figure 5a) and 298 K (Figure 5b). Besides, the results show that, at low temperature, H_2 adsorption is much stronger. These conclusions are consistent with H_2 adsorption in MIL-88A-Co elucidated by electronic structure calculations.[16]
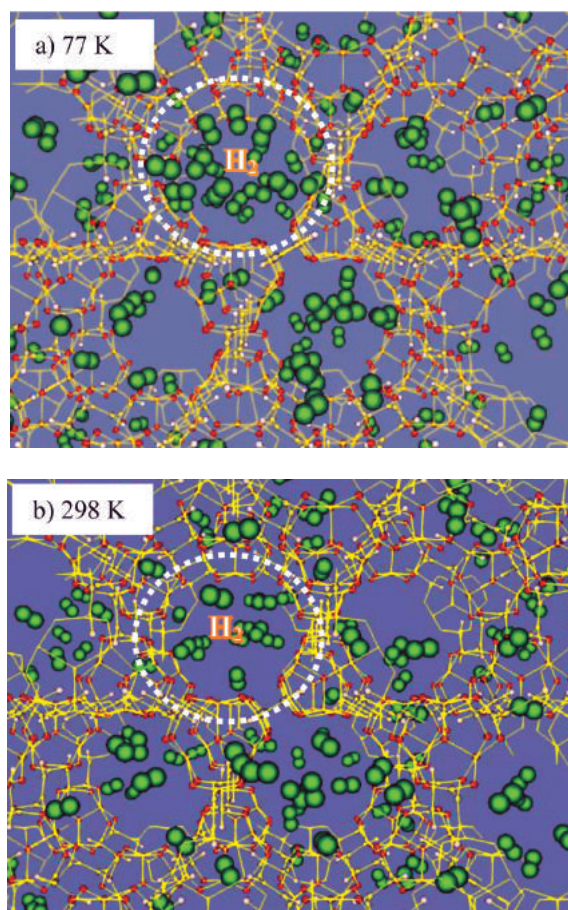
Figure 5. Visualization of H_2 adsorption in MIL-88A-Fe at 77 K (a) and 298 K (b) and the pressure of 1 bar. The H_2 molecule consists of two green balls.

3.3. CO_2 capture capacity of MIL-88A-Fe

For evaluating the CO_2 capture in MIL-88A-Fe, the reliability of the force field parameters was tested. The results showed that, at room temperature and pressure of 1 bar, the excess adsorption capacity of CO_2 in MIL-88A-Fe is 3.42 mmol/g. Meanwhile, at the same condition of pressure and temperature, the Chalati group's

experimental results showed the value of 4.95 mmol/g.[17] The above results presented that the simulation accuracy was approximately 70% compared to the experimental data. The difference between the results is due to the influence of experimental factors such as water vapour and impurities affecting the adsorption capacity compared to the simulation. However, this calculation is enough reliable to predict the CO_2 capture capacity of MIL-88A-Fe and new materials.

We also assessed the CO_2 capture capability of MIL-88A-Fe at room temperature via the adsorption isotherms (Figure 6).
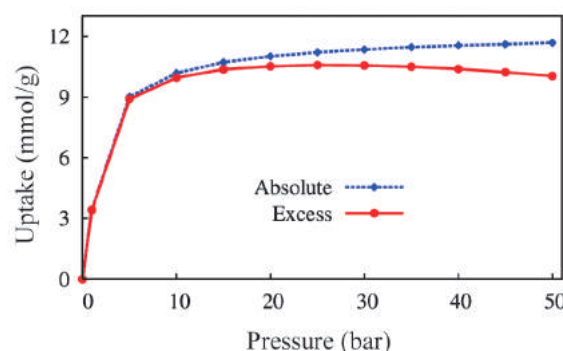
**Figure 6.** The absolute and excess CO_2 adsorption isotherms in MIL-88A-Fe at 298 K and pressures up to 50 bar.

For the investigated pressure below 50 bar, the maximum absolute and excess CO_2 uptakes of MIL-88A-Fe are 514.45 mg/g (11.69 mmol/g) at 50 bar and 465.61 mg/g (10.58 mmol/g) at 25 bar, respectively. The absolute and excess CO_2 amount adsorbed per unit volume of MIL-88A-Fe correspond to 280.57 và 256.83 cm^3(STP)/cm^3. The calculation shows that the CO_2 capture capacity is not higher than the highly appreciated MOF structures until now (such as MOF-200, MOF-210, MOF-205, MOF-177 and MOF-5).[18] However, the CO_2 volumetric uptakes are remarkable. To date, the MOF materials with the highest CO_2 capture capacity are MOF-200 and MOF-210 with 2400 mg/g and 2396 mg/g at 298 K and 50 bar[18] because of their high saturation pressures compared to other sorbents. MOF-117 was also evaluated for the high CO_2

capture capacity with 33.5 mmol/g and 320 $cm^3(SPT)/cm^3$ at 298 K and 35 bar. Details of the MOFs with high CO_2 uptakes are listed in the review journal.[19]

The visualization of CO_2 adsorption capacity in MIL-88A-Fe is also shown in Figure 7. The picture shows CO_2 concentrate more evenly in the adsorbent, *ie.* they concentrate on the hollow sites, organic linkers, and metal sites.
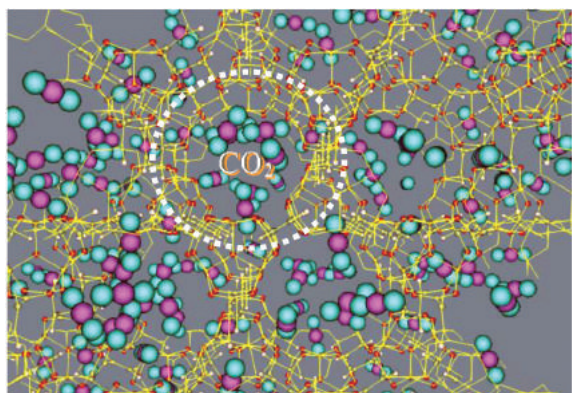

Figure 7. Visualization of CO_2 adsorption in MIL-88A-Fe at 298 K and 1 bar. The CO_2 molecule consists of two turquoise-coloured balls (O atoms) linked to a pink-coloured ball (C atom).

4. CONCLUSIONS

The force field parameterization that combines the DDEC partial atomic charge calculation and the LJ parameters taken in the universal force field leads to reliable results.

The results show that the volumetric capacity of H_2 storage and CO_2 capture in MIL-88A-Fe are noteworthy. These gases are favourable in the hollow sites of MIL-88A-Fe surrounded by O atoms and Fe atoms compared to other positions, especially for H_2 gas.

In the next research, based on the density functional theory, we will clarify and explain the preferred adsorption positions of H_2 and CO_2 in MIL-88A-Fe in more detail.

Acknowledgment

REFERENCES

1. G. Ferey. Hybrid porous solids : past, present, future, *Chemistry Society Reviews,* **2008**, *37*, 191–214.

2. H. Furukawa, K. E. Cordova, M. O. Keeffe, O. M. Yaghi. The chemistry and applications of metal-organic frameworks, *Science*, **2013**, *341*, 1230444-1 – 1230444-12.

3. C. Serre, F. Millange, S. Surblé, G. Férey. A route to the synthesis of trivalent transition-metal porous carboxylates with trimeric secondary building units, *Angewandte Chemie International Edition*, **2004**, *43*, 6286–6289.

4. C. Mellot-Draznieks, C. Serre, S. Surblé, N. Audebrand, G. Férey. Very large swelling in hybrid frameworks: A combined computational and powder diffraction study, *Journal of the American Chemistry Society,* **2005** *127*, 16273–16278.

5. M. P. Suh, H. J. Park, T. K. Prasad, D.-W. Lim. Hydrogen storage in metal - organic frameworks, *Chemical Reviews*, **2012**, *112*, 782–835.

6. L. J. Murray, M. Dinca, J. R. Long. Hydrogen storage in metal-organic frameworks, *Chemistry Society Reviews*, **2009**, *38*, 1294–1314.

7. J. L. C. Rowsell, O. M. Yaghi. Strategies for hydrogen storage in metal-organic frameworks, *Angewandte Chemie International Edition*, **2005**, *44*, 4670–4679.

8. D. Dubbeldam, S. Calero, D. E. Ellis, R. Q. Snurr. RASPA: molecular simulation software for adsorption and diffusion in flexible nanoporous materials, *Molecular Simulation*, **2016**, *42*, 81–101.

9. D. Levesque, A. Gicquel, F. L. Darkrim, S. B. Kayiran. Monte Carlo simulations of hydrogen storage in carbon nanotubes, *Journal of Physics: Condensed Matter*, **2002**, *14*, 9285–9293.

10. J. G. Harris, K. H. Yungt. Carbon dioxide's liquid-vapor coexistence curve and critical properties as predicted by a simple molecular model, *Journal of Physical Chemistry*, **1995**, *99*, 12021–12024.

11. N. T. X. Huynh, O. M. Na, V. Chihaia, D. N. Son. A computational approach towards

understanding hydrogen gas adsorption in Co-MIL-88A, *RSC Advances*, **2017**, *7*, 39583–39593.

12. M. Dion, H. Rydberg, E. Schröder, D. C. Langreth, B. I. Lundqvist. Van der Waals density functional for general geometries, *Physical Review Letters*, **2004**, *92*, 246401-1 – 246401-4.

13. F. D. Murnaghan, *Finite deformation of an elastic solid*, 1st edition, Wiley, New York, 1951.

14. N. T. X. Huynh, V. Chihaia, D. N. Son, Hydrogen storage in MIL-88 series, *Journal of Materials Science*, **2019**, *54*, 3994–4010.

15. W. X. Lim, A. W. Thornton, A. J. Hill, B. J. Cox, J. M. Hill, M. R. Hill. High performance hydrogen storage from Be-BTB metal-organic framework at room temperature, *Langmuir*, **2013**, *29*, 8524–8533.

16. S. Wongsakulphasatch, W. Kiatkittipong, J. Saupsor, J. Chaiwiseshphol, P. Piroonlerkgul, V. Parasuk, S. Assabumrungrat. Effect of Fe open metal site in metal-organic frameworks on post-combustion CO_2 capture performance, *Greenhouse gases: Science and Technology,* **2017**, *7*, 383–394.

17. H. Furukawa, N. Ko, Y. B. Go, N. Aratani, S. B. Choi, E. Choi, A. Ö. Yazaydin, R. Q. Snurr, M. O'Keeffe, J. Kim, O. M. Yaghi. Ultrahigh porosity in metal-organic frameworks, *Science*, **2010**, *329*, 424–428.

18. A. R. Millward, O. M. Yaghi. Metal organic frameworks with exceptionally high capacity for storage of carbon dioxide at room temperature, *Journal of the American Chemistry Society*, **2005**, *127*, 17998–17999.

19. T. T. T. Huong, P. N. Thanh, N. T. X. Huynh, D. N. Son. Metal – organic frameworks: State-of-the-art material for gas capture and storage, *VNU Journal of Science: Mathematics - Physics*, **2016**, *32*, 67–85.

Nghiên cứu nhận dạng vật sử dụng mạng nơ-ron Inception-v3 hoạt động trên Raspberry Pi 3B+

Nguyễn An Toàn*, **Nguyễn Ngọc Thiện**, **Nguyễn Thanh Trực**

Khoa Kỹ thuật và Công nghệ, Trường Đại học Quy Nhơn, Việt Nam

TÓM TẮT

Phân loại ảnh (Image Classification) là bài toán quan trọng bậc nhất trong lĩnh vực thị giác máy tính (Computer Vision). Mặc dù nó đơn giản nhưng lại có rất nhiều ứng dụng thực tế, phân loại hình ảnh có nhiệm vụ gán một nhãn cho ảnh đầu vào từ một nhóm danh mục cố định. Bài báo này đã ứng dụng việc phân loại hình ảnh để nhận dạng vật bằng cách đưa hình ảnh của vật cần nhận dạng sau đó tiến hành gán nhãn cho hình ảnh rồi thông báo tên nhãn (tên vật) qua kênh âm thanh. Việc phân loại dựa trên mô hình mạng nơ-ron Inception-v3 đã được đào tạo sẵn trên Tensorflow và sử dụng hệ điều hành Raspberian chạy trên Raspberry Pi 3B+ tạo ra một thiết bị có khả năng nhận dạng vật nhỏ gọn và tiện lợi có thể ứng dụng trong nhiều lĩnh vực.

Từ khóa: *Nhận dạng vật, Raspberry, mạng nơ-ron tích chập, mạng nơ-ron Inception-v3, Tensorflow.*

Tác giả liên hệ chính.
Email: *nguyenantoan@qnu.edu.vn*

Research of object recognition using neural network Inception-v3 model operating on Raspberry Pi B3+

Nguyen An Toan*, **Nguyen Ngoc Thien, Nguyen Thanh Truc**

Faculty of Engineering and Technology, Quy Nhon University, Vietnam

ABSTRACT

Image Classification is the most important issue in the field of computer vision. It is very simple and has many practical applications. The image classifier is responsible for assigning a label to the input image from a fixed category group. This article has applied image classification to identify objects by giving the image of the object to be identified, then labeling the image and announcing the label name (object name) through the audio channel. The classification is based on the neural network Inception-v3 model that has been trained on Tensorflow and used Raspberian operating system running on the Raspberry Pi 3 B+ to create a device capable of recognizing objects which compact size and convenient to apply in many fields.

Keywords: *Object recognition, Raspberry, convolutional neural network, neural network Inception-v3, Tensorflow.*

1. INTRODUCTION

In the Industry 4.0, the application of recognition technology in the working environment and industry has posed the need for devices capable of image classification to recognize objects completely automatically without human support. With the above requirement, many methods to assist and replace human vision have been developed to recognize surrounding objects such as detecting and vibrating devices when there are obstacles by Sahoo et al.[1] Currently, there is OrCam MyEye 2 device[2] that supports object recognition. It is a costly foreign product written in English language. These devices have partly assisted in identifying objects but it can not meet the needs of object identification for Vietnamese users. Therefore, it is necessary to have a compact device with reasonable cost that supports object recognition to replace the object recognition by human vision.

Many computer vision technologies have been developed today, and one of the technologies that can help with object recognition is image classification.[3] Image classification process can be based on many different convolutional neural network models such as LeNet-5, AlexNet, VGG-16, Inception-v3, ResNet-50... In this study, the authors propose a device that uses a Raspberry Pi 3B+ to recognize images of objects captured from a camera. This study applies the image classification problem using the Inception-v3 model.[4] With this technology, the identification of objects will become easy, accurately responding to information of objects with many modes of operation and flexible support for users.

---

*Corresponding author.

Email: nguyenantoan@qnu.edu.vn

2. CONTENT

2.1. Convolutional neural network

Convolutional neural network (CNN)[5,6] is network architecture for deep learning.[7] CNN are deep artificial neural networks that are used primarily to classify images, cluster them by similarity and perform object recognition [8] within scenes. A CNN is comprised of one or more convolutional layers and then followed by one or more fully connected layers as in a standard multilayer neural network. It learns directly from images. A CNN can be trained to do image analysis tasks including classification, object detection, segmentation and image processing.
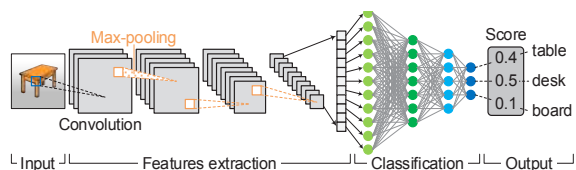

Figure 1. The overall architecture of the CNN.

Figure 1 shows the overall architecture of CNNs consisting of two main parts: Feature extractors and a classifier. In the feature extraction layers, each layer of the network receives the output from its immediate previous layer as its input and passes its output as the input to the next layer. The CNN architecture consists of three types of layers: Convolution, max-pooling, and classification.

2.1.1. Convolutional Layer

In this layer, feature maps from previous layers are convolved with learnable kernels. The output of the kernels goes through a linear or non-linear activation function, such as sigmoid, hyperbolic tangent, Softmax, rectified linear, and identity functions to form the output feature maps. Each of the output feature maps can be combined with more than one input feature map. In general, we have that:

$$x_j^l = f\left(\sum_{i \in M_j} x_i^{l-1} * k_{ij}^l + b_j^l \right) \qquad (1)$$

where:

x_j^l is the output of the current layer

x_i^{l-1} is the previous layer output

k_{ij}^l is the kernel for the present layer

b_j^l are the biases for the current layer

M_j represents a selection of input maps.

For each output map, an additive bias b is given. However, the input maps will be convolved with distinct kernels to generate the corresponding output maps. The output maps finally go through a linear or non-linear activation function (such as sigmoid, hyperbolic tangent, Softmax, rectified linear, or identity functions).

2.1.2. Sub-sampling Layer

The subsampling layer performs the down sampled operation on the input maps. This is commonly known as the pooling layer. In this layer, the number of input and output feature maps does not change. For example, if there are n input maps, then there will be exactly n output maps. Due to the down sampling operation, the size of each dimension of the output maps will be reduced, depending on the size of the down sampling mask. For example, if a 2×2 down sampling kernel is used, then each output dimension will be half of the corresponding input dimension for all the images. This operation can be formulated as:

$$x_j^l = down\left(x_i^{l-1} \right) \qquad (2)$$

Where $down(.)$ represents a sub-sampling function. Two types of operations are mostly performed in this layer: Average pooling or max-pooling. In the case of the average pooling approach, the function usually sums up over $n \times n$ patches of the feature maps from the previous layer and selects the average value. On the other hand, in the case of max-pooling, the highest value is selected from the $n \times n$ patches of the feature maps. Therefore, the output map dimensions are reduced by n times. In some special cases, each output map is multiplied with a scalar. Some alternative sub-sampling layers have been proposed, such as fractional max-pooling layer and sub-sampling with convolution.[9]

2.1.3. Classification Layer

This is the fully connected layer which computes

the score of each class from the extracted features from a convolutional layer in the preceding steps. The final layer feature maps are represented as vectors with scalar values which are passed to the fully connected layers. The fully connected feed-forward neural layers are used as a soft-max classification layer. Figure 2 shows the basic operations in the convolution and sub-sampling of an input image.
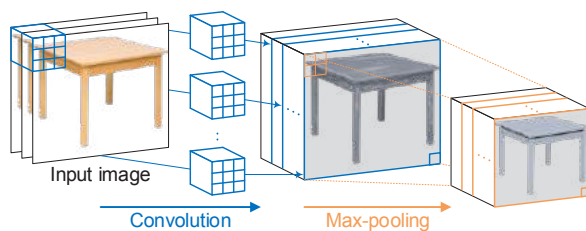

Figure 2. Feature maps after performing convolution and pooling operations.

As the fully connected layers are expensive in terms of computation, alternative approaches have been proposed during the last few years. In most cases, two to four layers have been observed in different architectures, including LeNet, AlexNet, and VGG Net. In this study, the Inception-v3 model has been proposed to be used for image classification with advantages over other models.

2.2. Inception-v3 model

Inception-v3 model is considered one of the CNN architectures for image classification. It was first introduced by Szegedy et al.[4] This model contains more than 25 million of fitted parameters and was trained by the one of the top hardware experts in the industry.
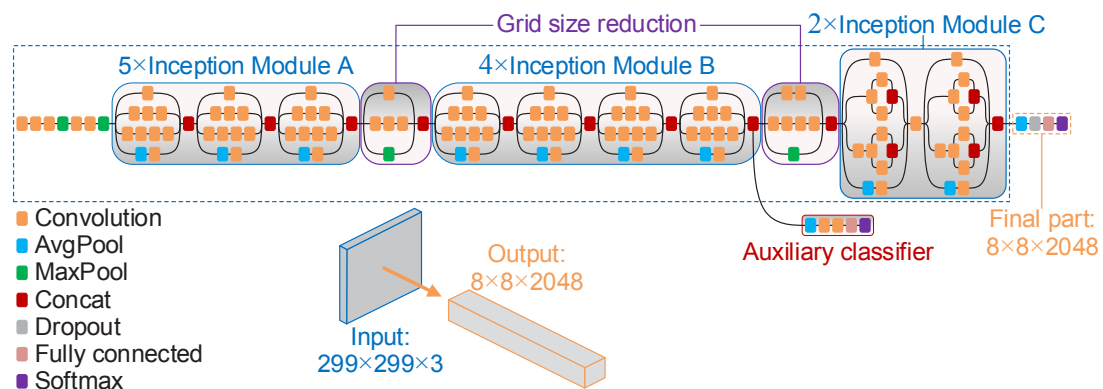
Figure 3. The architecture of the Inception-v3 model.

The CNN models are black boxes that construct image features. The Inception-v3 model uses the image feature extraction module which was trained on ImageNet. The ImageNet is an accessible database for high resolution images designed for developers and researchers in the field of image processing. Generally, the Inception-v3 model consists of two main parts: (1) the CNN to extract image features; and (2) the image classification with the softmax and the fully-connected layers. The softmax layer is used as the final layer of a neural network-based classifier in order to provide normalized class likelihoods for the outputs.

The main difference between Inception-v3 model and traditional neural network[8]

is Inception blocks. They involve input transforming with multiple filters and linking their results together.

Figure 4. Inception Module A using factorization.

The purpose of using Inception blocks is to reduce the number of connections/parameters without decreasing the network efficiency. The architecture of the Inception-v3 model is shown in Figure 3, where:

Inception Module A used filter layers to adjust the image for a smaller size. This used two layers of 3×3 filters (Figure 4) instead of one layer of 5×5 traditional filter and the result was that the parameter is reduced by 28%.[4]
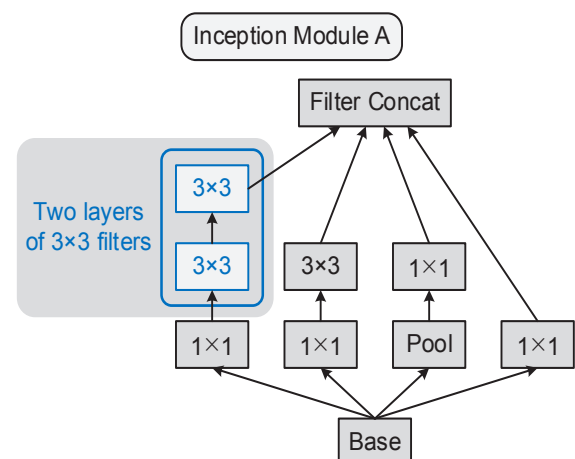
● Similarly, Inception Module B used one layer of 3×1 filter followed by one layer of 1×3 filter (Figure 5) replaces one layer of 3×3 traditional filter and the result was that the parameter is reduced by 33%.[4]
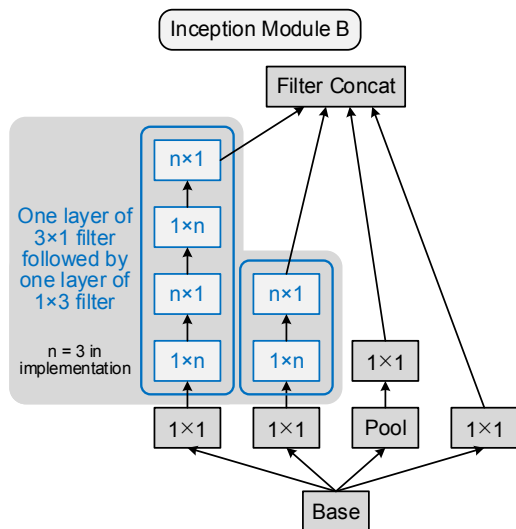

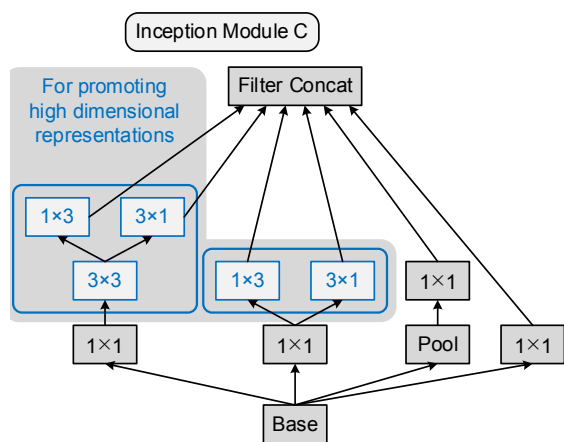**Figure 5.** Inception Module B using asymmetric factorization.

Figure 6. Inception Module C using asymmetric factorization.

● And Inception Module C is also proposed for promoting high dimensional representations (Figure 6) according to the description by Szegedy et al.[4]

Table 1. The output and input sizes of Inception-v3 model.

Type	Patch size/stride	Input size
conv	3×3/2	299×299×3
conv	3×3/1	149×149×32
conv padded	3×3/1	147×147×32
pool	3×3/2	147×147×64
conv	3×3/1	73×73×64
conv	3×3/1	71×71×80
conv	3×3/1	35×35×192
3×Inception A	As in Figure 4	35×35×288
5×Inception B	As in Figure 5	17×17×768
2×Inception C	As in Figure 6	8×8×1280
Pool	8×8	8×8×2048
Linear	logits	1×1×2048
Softmax	classifier	1×1×1000

Table 1 describes in the sizes across each layer of Inception-v3 model. There are three traditional inception modules of Inception Module A at the 35×35 with 288 filters each as depicted in Figure 4. This is reduced to a 17×17 grid with 768 filters using the grid reduction technique. Inception Module A is followed by five instances of Inception Module B as depicted in Figure 5. This is reduced to a 8 × 8 × 1280 grid with the grid reduction technique. At the coarsest 8 × 8 level, there are two Inception modules as depicted in Figure 6, with a concatenated output filter bank size of 2048 for each tile.

2.3. Object recognition method

In this study, we used the Inception-v3 model and Tensroflow 1.9.0 library on the Raspberian operating system running on Raspberry Pi 3B+.

By applying the Tensorflow library[10] and using the Inception-v3 model described above to perform object recognition. This classifier is trained to image classification and then predict the accuracy of the input image. This classifier is considered as a function that takes some data

as inputs (object images) and assigns a value prediction (*Score*) to it as outputs. This is done by an automatic technique called supervised learning. Generally speaking, this technique begins with the following few standard steps:

• Step 1 starts with sample image processing.

• Step 2 is to use the input images to train the classifier using pretrained models and learning algorithms.

• Step 3 is to find patterns in the trained images and then predicting the accuracy levels (*Score*).

Figure 7 shows a canonical data model (CDM) of the three steps in this study. This figure shows the data entities and their relationships in the developed machine learning workflow. Also, Python version 3.7 was used in this study to develop this image classifier by implementing the Inception-v3 model in TensorFlow.
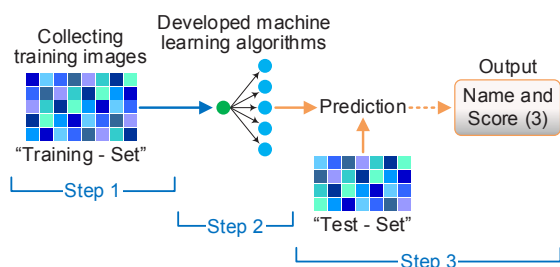

Figure 7. Canonical data model of the developed machine learning workflow.

Firstly, the size of the input image was cropped to 299×299 pixels which is the region of interest in order to be compatible with the ImageNet database, where the Inception-v3 model was created and trained. Subsequently, the image data is fed to the Inception-v3 model to extract and classify from which the result is the object name and the number of correct predictions in the input image.

The number of predictions (*Score*) is calculated by the following formula:[11]

$$Score = \frac{P_{true}}{\sum P_{made}} \qquad (3)$$

where:

P_{true} is number of corret predictions

P_{made} is total number of predictions made.

To perform the recognition, this study installed TensorFlow on a Raspberry Pi 3B+ and ran a simple image classification on the pre-trained Inception-v3 model.

We used the following basic command to install Tensorflow:

pip3 install --user tensorflow

Then, we have downloaded its 1.9.0 model with the following command:

gitclone https://github.com/tensorflow/models.git

After downloading, we access the path *models/tutorials/image/imagenet* with the following command:

cd models/tutorials/image/imagenet

Figure 8. The input image (the desk).

This study ran the python3 program called *classify image.py* to classify the image with the input image (the desk) as shown in Figure 8. This will put the input image into the neural network, which returns predictions about what the image is (the object name) with its number of predictions (*Score*) as shown in Figure 9.
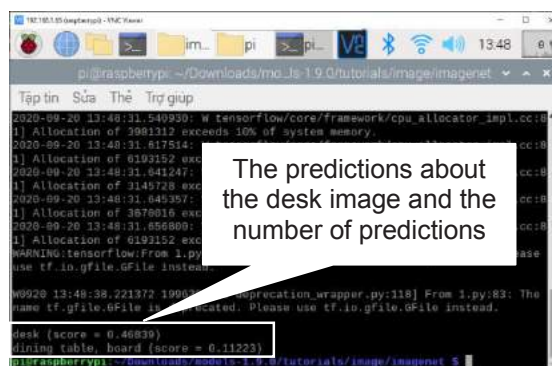

Figure 9. Object recognition program results.

As Figure 9 shows, the neural network predicted correctly, with *Score* = 46,839%. It also gives the result of possible a *dining table*, but has a smaller value than *Score* = 11,223%.

2.3. Develop the program

From the basis of the Inception-v3 model above, we have built an object recognition program with the size of the input image as 299×299, standardized according to the object recognition process. This study presents a state diagram of image classification for recognizing objects as shown in Figure 10.

Initially, the program will initiate the initial conditions. This process takes 5-7 seconds. After the program has finished the initialization process, the program is ready to go. Meanwhile, the program will wait for the user to press the shutter button to operate. When the user presses the shutter button, the program will notify the sound and take picture. This process takes about 2 seconds. After the image is captured, the image data is fed into the Tensorflow library for processing, and the Inception-v3 model performs image classification.

The object name and *Score* will be exported as text data. Only those with the highest *Score* will be output. In this study, we take up to 5 objects with the highest *Score*. After that, the program will output the sound of the object's name in Google Vietnamese voice. The program will stop working when the user presses the OFF button.
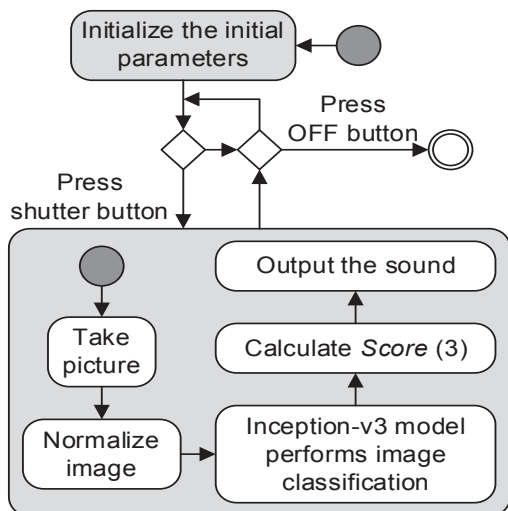
Figure 10. State diagram for recognizing objects.

The state diagram in Figure 10 will be coded in python running on Raspberian (the operating system of Raspberry Pi 3B+).

2.4. Architecture of recognition device

The object recognition model using the Raspberry Pi 3B+ is depicted in the diagram in Figure 11.
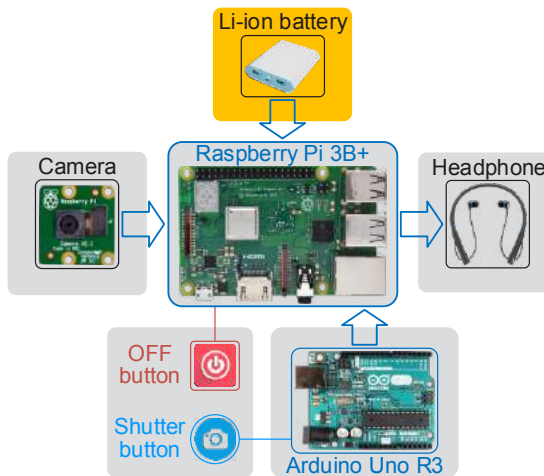
Figure 11. Device overview block diagram.

Raspberry Pi 3B+ is a small, low-cost, energy-saving single computer board. It is the device's processing center with the function of image processing, analysis and classification. It runs on the Raspberian operating system. In addition, the Arduino Uno R3 has the function of connecting to the shutter button and UART communication with the Raspberry Pi 3B+. Moreover, the Arduino Uno R3 is also used to develop device later, depending on the needs of the field, there will be suitable sensors. The Raspberry Pi camera is used to receive images that are transferred to the Raspberry Pi 3B+ by the FFC/FPC 15 pin cable. It uses 5MP resolution OV5647 sensor. It has good picture quality, high resolution with HD quality. This is suitable for practical application. Headphone (speaker) is used to bring audio signals from Raspberry Pi 3B+ out and users can also use Bluetooth headphones. The power supply of the device is a Li-ion battery pack with a voltage of 5V, it has a compact design and large capacity. This study has conducted experiments and results show that the operating time of this source is about 5 hours

of continuous operation. Device model after complete assembling can be seen in Figure 12.
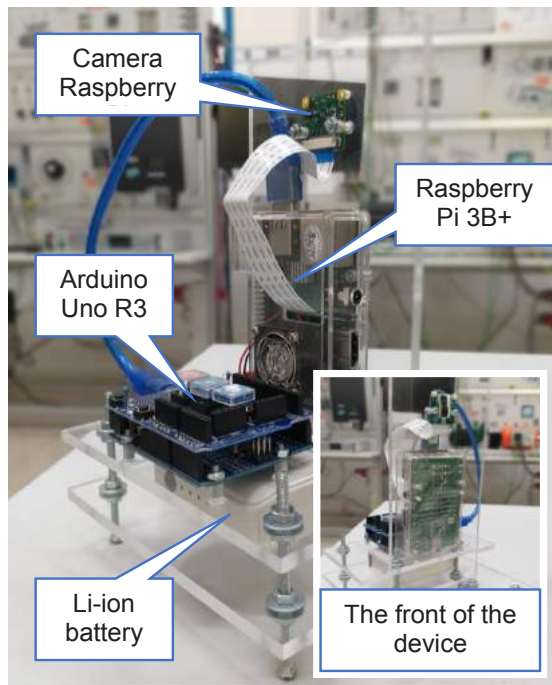
Figure 12. Model of object recognition device.

2.5. Experimental results

After the hardware and software of the device are completed as above, the authors conducted three experiments. In each experiment, the authors placed three random objects on the table and performed manipulations for the device to identify. The operation steps include:

● Step 1: Point the Camera at the object to be recognized.

● Step 2: Press the shutter button 📷 to take pictures.

● Step 3: Wait for the device to output the sound which is the name of the recognized object in Vietnamese.

When the device has recognized the object, the screen (it connected to the Raspberry Pi 3B+ via HDMI) also displays the text of the names of the recognized objects and is accompanied by a value *Score* which indicates accuracy of recognition results. The total Score of all recognized objects is 1. On a multi-object frame, objects are large and clearly have a *Score* value of quite high, and the remaining objects are small with a *Score* value lower.

2.5.1. Experiment 1

In Experiment 1, the authors performed the 3-object recognition device: corn, banana, and flowerpot. Figure 13 shows the implementation process, Figure 14 shows the images and results recognized by the device, and Figure 15 shows the output of a Python program on a Raspberry Pi 3B+.

Figure 13. Conducting recognition in Experiment 1.
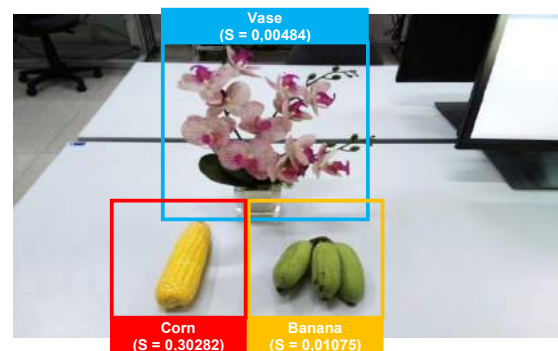
Figure 14. Recognition results of Experiment 1.

As shown in Figure 15, the program has been recognized ear (*Score*=0.58129), corn (*Score*=0.30282), banana (*Score*=0.01075), vase (*Score*=0,00484).
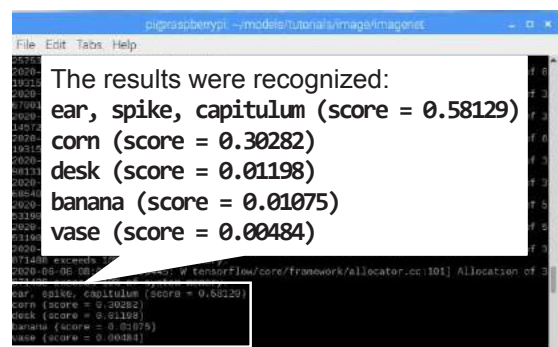
Figure 15. Recognition results in experiment 1 were received on a screen connected to a Raspberry Pi 3B+.

Next, the program uses the Trans library in the Python programming language. This is to convert the above object name text results (English) into Vietnamese. At the same time, the device uses the gTTs library to convert text into speech (Google Vietnamese voice). After, the device converts the text to audio, the audio file will be saved and played. The process of converting from English results to written audio is similar to the other two experimental results. Finally, the device converts the text to audio, the audio file will be saved and played. The process of converting from English results to audio is similar to the other two experimental results.

2.5.2. Experiment 2

In Experiment 2, the authors performed recognition of sharp objects with three subjects, including: meat cleaver, screwdriver and water bottle. Implementation process and experimental results are shown in Figure 16, Figure 17 and Figure 18.

The results returned as expected, the device recognized it as meat cleaver (*Score*=0.39394), screwdrivers (*Score*=0.04013), water bottle (*Score*=0.23964). This makes the device available in situations where hazardous objects are identified.

Figure 16. Conducting recognition in Experiment 2.
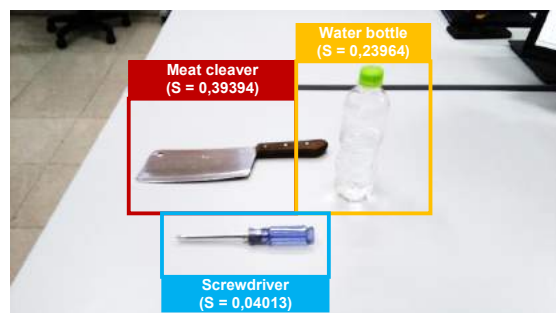
Figure 17. Recognition results of Experiment 2.
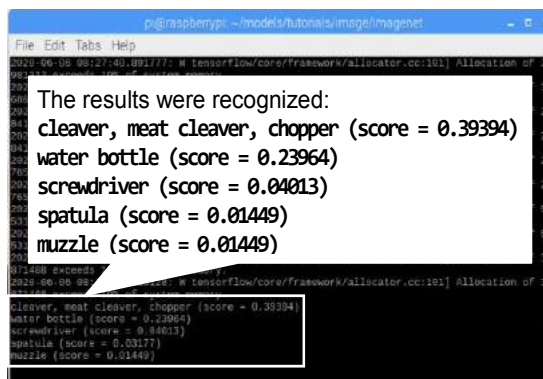
Figure 18. Recognition results in Experiment 2 were received on a screen connected to a Raspberry Pi 3B+.

2.5.3. Experiment 3

In Experiment 3, the authors conducted three objects for the object recognition device, including: monitors, computer mice and computer keyboards. Implementation process and experimental results are shown in Figure 19, Figure 20 and Figure 21.

Figure 19. Conducting recognition in Experiment 3.

Figure 20. Recognition results of Experiment 3.

Figure 21. Recognition results in Experiment 3 were received on a screen connected to a Raspberry Pi 3B+.

The results returned as expected, the device recognized that it was computer mouse (*Score*=0.06297), screen (*Score*=0.27909), computer keyboard (*Score*=0.01894). We finish the experiment.
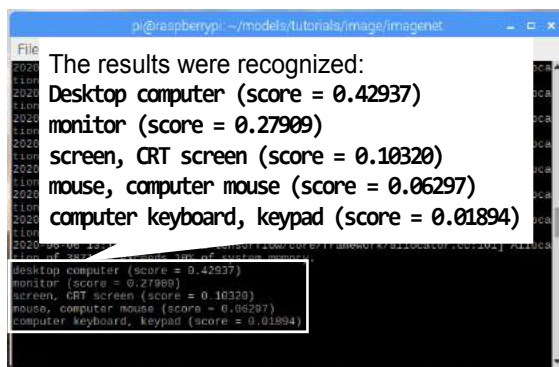
After 3 times of experiments showing that the device is capable of identifying objects with high reliability, the recognition results are also highly accurate.

3. CONCLUSIONS

The study presented the object recognition study using Raspberry Pi 3B+ and the Inception-v3 model. The result is a device that is compact and portable with simple usage, suitable for everyone. The experimental results in this study show that the names of objects recognized have a relatively high accuracy, along with a relatively high predictive value. However, the device's response time is slow, which can be improved by better hardware devices. With the above results, this device can be used in many different fields such as health, society, education, etc. depending on the purpose of use. In addition, the device also combines with different sensors to create a specific device according to the needs of the user.

REFERENCES

1. N. Sahoo, H. W. Lin, Y. H. Chang. Design and implementation of a walking stick aid for visually challenged people, *Sensors MDPI*, **2019**, *19*(130), 17.

2. W. Yip, Z. Stoev. Determining success of the OrCam MyEye/MyReader in patients with visual impairment, *Investigative ophthalmology & Visual science*, **2017**, *58*(8), 3271.

3. X. Xia, C. Xu, B. Nan. *Inception-v3 flower classification*, 2017 2nd International conference on image, Vision and computing, Chengdu, China, 2017.

4. C. Szegedy, V. Vanhoucke, S. Ioffe, J. Shlens, Z. Wojna. *Rethinking the inception architecture for computer vision*, Computer vision and pattern recognition 2016, Cornell University, 2016.

5. N. Srivastava, G. Hinton, A. Krizhevsky, I. Sutskever, R. Salakhutdinov. Dropout: A simple way to prevent neural networks from overfitting, *Journal of machine learning research*, **2014**, *15*(56), 1929−1958.

6. M. D. Zeiler, G. W. Taylor, R. Fergus. *Adaptive deconvolutional networksformid and high level feature learning*, 2011 IEEE International conference on computer vision, Barcelona, Spain, 2011.

7. C. Szegedy, W. Liu, Y. Jia, P. Sermanet, S. Reed, D. Anguelov, D. Erhan, V. Vanhoucke, A. Rabinovich. *Going deeper with convolutions*, The IEEE conference on computer vision and pattern recognition, Cornell University, 2015.

8. P. Ramachandran, B. Zoph, Q. V. Le. *Searching for activation functions*, 6th International conference on learning representations, London, United Kingdom, 2018.

9. M. Z. Alom, T. M. Taha, C. Yakopcic, S. Westberg, P. Sidike, M. S. Nasrin, M. Hasan, B. C. V. Essen, A. A. S. Awwal, V. K. Asari. A state-of-the-art survey on deep learning theory and architectures, *Electronics (Switzerland)*, **2019**, *8*(3), 1-67.

10. N. R. Gavai, Y. A. Jakhade, S. A. Tribhuvan, R. Bhattad. *MobileNets for flower classification using TensorFlow*, 2017 International conference on big data, IoT and Data Science, Pune, India, 2018.

11. O. Albatayneh, L. Forslöf and K. Ksaibati. *Image retraining using tensorFlow implementation of the pretrained inception-v3 model for evaluating gravel road dust*, The ASCE American society of civil engineers, 2020.

Nghiên cứu so sánh các phương pháp dự báo phụ tải ngắn hạn trong lưới điện phân phối

Lê Tuấn Hộ[*], **Lê Quang Hưng, Phan Thanh Hoàng**

Khoa Kỹ thuật và Công nghệ, Trường Đại học Quy Nhơn, Việt Nam

TÓM TẮT

Dự báo phụ tải ngắn hạn đóng một vai trò cực kỳ quan trọng trong việc xây dựng kế hoạch vận hành cũng như đảm bảo độ tin cậy của bất kỳ hệ thống điện nào. Các phương pháp dự báo phụ tải ngắn hạn về cơ bản có thể được phân thành ba loại chính như sau: các phương pháp thống kê, các phương pháp sử dụng trí tuệ nhân tạo và các phương pháp kết hợp giữa hai phương pháp này. Mỗi phương pháp đều có những ưu điểm và nhược điểm riêng. Do đó, mục tiêu của bài báo này là khảo sát hiệu quả của mô hình thống kê ARIMA và sử dụng mạng nơ ron nhân tạo trong dự báo phụ tải ngắn hạn của lưới điện phân phối. Trước tiên, bài báo tiến hành phân tích phụ tải tiêu thụ của lưới điện phân phối Quy Nhơn và Phù Cát. Tiếp theo đó, hai phương pháp dự báo (Arima và mạng nơ ron) được áp dụng để dự đoán phụ tải ngắn hạn của hai lưới phân phối này. Cuối cùng, bài báo tiến hành phân tích, so sánh hiệu quả của hai phương pháp đã sử dụng dựa trên các kết quả có được.

Từ khóa: *Dự báo phụ tải ngắn hạn, mạng nơ ron nhân tạo, mô hình Arima, lưới điện phân phối.*

---

[*] *Tác giả liên hệ chính.*
Email: *tuanhole@qnu.edu.vn*

A comparative study of short-term load forecasting methods in distribution network

Le Tuan Ho*, Le Quang Hung, Phan Thanh Hoang

Faculty of Engineering and Technology, Quy Nhon University, Vietnam

ABSTRACT

Short-term load forecasting plays an important role in building operation strategies and ensuring reliability of any electric power system. Generally, short-term load forecasting methods can be classified into three main categories: statistical approaches, artificial intelligence based-approaches and hybrid approaches. Each method has its own advantages and shortcomings. Therefore, the primary objective of this paper is to investigate the effectiveness of ARIMA model (e.g., statistical method) and artificial neural network (e.g., artificial intelligence based-method) in short-term load forecasting of distribution network. Firstly, the short-term load demand of Quy Nhon distribution network and short-term load demand of Phu Cat distribution network are analyzed. Secondly, the ARIMA model is applied to predict the load demand of two distribution networks. Thirdly, the artificial neural network is utilized to estimate the load demand of these networks. Finally, the estimated results from two applied methods are conducted for comparative purposes.

Keywords: *Short-term load forecasting, artificial neural network, ARIMA, distribution network.*

1. INTRODUCTION

Nowadays, the demand for electricity has increased noticeably due to the expansion of industrial and residential areas. In addition, the Vietnamese government has provided incentives for the huge development of wind and solar energy resources. Therefore, the load forecasting can be considered one of the most urgent issues in planning and development of power system. In power system operation, power load forecasting is an essential task of power companies in order to provide important decisions in operation and planning, load management, reliability evaluation of power system, and load dispatch. Short-term load forecasting ranging from hour, day, or week plays a significant role in daily and weekly operation modes. In the future, short-term load forecasting becomes more and more important as Vietnamese electricity market and renewable energy resources develop since these factors directly affects the spot price.

In order to perform short-term load forecasting, various prediction methods have been proposed such as multiple linear regression method,[1] regression based peak load forecasting using a transformation technique,[2] non-parametric short-term load forecasting,[3] ARIMA model,[4] ARMA model,[5] neural network,[6] fuzzy logic,[7] machine learning,[8] or hybrid method based on these methods.[9-10] Generally, these short-term forecasting methods can be classified into three main types, such as (1) statistical methods, (2) artificial intelligence-based methods and (3) hybrid methods. Each method has its specific

---

*Corresponding author.
Email: tuanhole@qnu.edu.vn

characteristics, implementation and effects in power system forecasting. In this paper, ARIMA model (a statistical method) and neural network (an artificial intelligence based-method) are utilized in short-term load forecasting. In addition, the effectiveness of these forecasting methods is compared.

Binh Dinh power company has 9 electricity branches and one high-voltage grid operation management team, in which each electricity branch is managing a distribution network, such as Quy Nhon, Phu Tai, Tuy Phuoc, An Nhon, Phu Cat, Phu My, Bong Son, Hoai An and Phu Phong. Recently, the load demand has dramatically increased due to the rapid urbanization and expansion of industrial zones. Especially, the short-term load demand of both Quy Nhon and Phu Cat electricity branches has the fastest growth rate[11]. Therefore, the short-term load forecasting of these distribution networks is analyzed in this paper. Based on the forecasted results, the suitable operation strategies with high reliability can be proposed.

The remainder of this paper is organized as follows. The next section will discuss the forecasting methods used in this paper. Section 3 will discuss case studies. The final section will be the conclusion and further studies.

2. FORECASTING METHODS

2.1. ARIMA model

Box & Jenkins (1970) first introduced ARIMA model (autoregressive integrated moving average) in time series analysis, namely Box-Jenkins method. This statistical model is used for forecasting quantitative time series, in which the future value of the variable depends on the movement trend of that object in the past. ARIMA model consists of three main components: AR (auto regression), I (integrated), and MA (moving average). ARIMA model includes p, d and q parameters, non-negative integers, where p is the order (number of time lags) of the autoregressive model, d is the degree of differencing (the number of times the data have

had past values subtracted), and q is the order of the moving-average model[12]. The effectiveness of using ARIMA model in forecasting depends on the estimation of p, d and q. The general equation of ARIMA (p, d, q) model can be represented as follows:

$$y_t = \delta + \alpha_1 y_{t-1} + ... + \alpha_p y_{t-p} + \beta_1 \\ + \varepsilon_{t-1} + ... + \beta_t \varepsilon_{t-q} + e_t \tag{1}$$

where: α is auto regression coefficient; ε is moving average coefficient; $\delta = \mu(\beta_1 + ... + \beta_q)$; μ is the average of the time series; e_t is the forecast error, this error is the difference between the forecasted value and the actual value $(e_t = \hat{y}_t - y_t)$.

2.2. Artificial neural network

2.2.1. Introduction

Recently, artificial neural network (or neural network) has been applied in various aspects of power system, especially in load forecasting. Neural network can be considered a "black – box". The structure of neural network includes three layers: input layer, hidden layer, and output layer. The general structure of a neural network is shown in Figure 1.

The external information is transferred to the input of the input layer. The output of the input layer with different weights and bias becomes the input of the hidden layer. Hidden layer has one or more layers. Each hidden layer has one or more hidden neurons. The output of hidden layer becomes the input of the output layer.
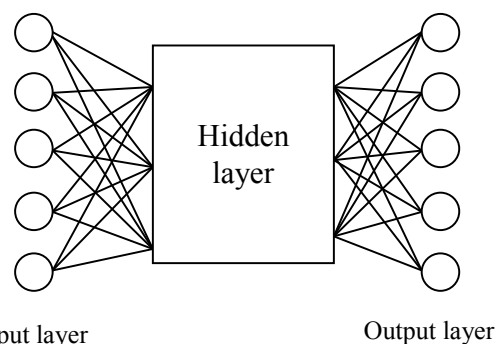

Figure 1. The general neural network structure

The mathematical equation of a neural network is presented as:

$$y(x) = f\left(\sum_{i=1}^{n} w_i x_i\right) \qquad (2)$$

where: $y(x)$ is the output value of x; f is activation function, w_i is connection weight of neuron x_i, x_i is the input value.

2.2.2. Training algorithm

The predicted results of neural networks depend on the application of training algorithms. An appropriate training algorithm will reduce the training time. The selection of training algorithm depends on various factors, including the complexity of the problem, the number of data in the training system, the weights and bias, and the error criteria. Some popular training algorithms commonly used in neural networks can be listed as follows:

- Levenberg-Marquardt (e.g. trainlm)

- BFGS Quasi-Newton (e.g. trainbfg)

- Resilient Backpropagation (e.g. trainrp)

- Scaled Conjugate Gradient (e.g. trainscg)

- Bayesian regularization backpropagation (e.g. trainbr).

The training process can be taken in several cycles (epoch) and repeated until the desired error value is reached.

2.3. Evaluation criteria

In forecasting problem, there is always an error between the actual value and the predicted value. This error is a criterion to evaluate the suitability of the forecasting model. Based on this error, the parameters of forecasting models can be adjusted.

In statistics, there are several criteria to evaluate the forecasting error. However, three typical evaluation criteria are used in this paper as follows:

a. Mean Absolute Error (MAE) criterion

$$MAE = \frac{\sum_{t=1}^{n} |e_t|}{n} = \frac{\sum_{t=1}^{n} |y_t - \hat{y}_t|}{n} \qquad (3)$$

where: n is the number of forecasting points.

b. Mean Absolute Percent Error (MAPE) criterion

$$MAPE = \frac{\sum_{t=1}^{n} \dfrac{|e_t|}{y_t}}{n} = \frac{\sum_{t=1}^{n} \dfrac{|y_t - \hat{y}_t|}{y_t}}{n} \qquad (4)$$

c. Mean Squared Error (MSE) criterion

$$MSE = \frac{\sum_{t=1}^{n} e_t^2}{n} = \frac{\sum_{t=1}^{n} (y_t - \hat{y}_t)^2}{n}. \qquad (5)$$

3. APPLICATION OF ARIMA MODEL AND ARTIFICIAL NEURAL NETWORK IN LOAD FORECASTING OF QUY NHON AND PHU CAT DISTRIBUTION NETWORKS

The load demand of Quy Nhon distribution network and Phu Cat distribution network in two different months (February and August 2020) is investigated in this paper. These are typical months of spring and summer periods. Data of maximum load demand (P_max, MW) and minimum load demand (P_min, MW) in February and August 2020 of Quy Nhon distribution network and Phu Cat distribution network is illustrated in Tables 1 and 2, respectively.[11]

Table 1. Load data in February 2020

Date	Quy Nhon		Phu Cat	
	P_max	P_min	P_max	P_min
Sat, 01/02	56.2	32.9	15.2	6.9
Sun, 02/02	55.5	34.1	17.7	7.3
Mon, 03/02	58.1	33.8	21.7	7.8
Tue, 04/02	61.7	34.1	22.8	9.2
Wed, 05/02	62.6	38.7	22.9	10.8
Thu, 06/02	63.6	35.9	24.1	10.2
Fri, 07/02	68.1	36.9	23.8	11.5
Sat, 08/02	62.9	35.9	24.5	13.0
Sun, 09/02	59.9	36.4	22.6	11.6
Mon, 10/02	60.7	34.6	23.3	11.8
Tue, 11/02	60.3	33.3	25.2	10.3
Wed, 12/02	60.6	37.3	26.3	12.0
Thu, 13/02	60.5	35.5	31.6	13.9
Fri, 14/02	61.0	36.7	27.8	10.9
Sat, 15/02	60.8	38.6	26.8	12.3
Sun, 16/02	59.4	38.9	27.1	12.9
Mon, 17/02	56.1	35.8	25.2	11.7
Tue, 18/02	56.0	32.2	23.9	9.5

Wed, 19/02	61.8	32.6	24.7	12.5
Thu, 20/02	62.3	34.5	24.2	11.4
Fri, 21/02	59.3	37.2	24.7	13.1
Sat, 22/02	58.3	33.9	23.6	11.9
Sun, 23/02	56.3	34.5	23.9	11.7
Mon, 24/02	67.8	36.5	24.3	10.2
Tue, 25/02	64.1	39.5	26.4	11.0
Wed, 26/02	62.0	37.8	26.5	13.1
Thu, 27/02	59.9	37.3	27.5	13.3
Fri, 28/02	59.0	36.6	25.5	14.0
Sat, 29/02	57.5	37.1	25.8	13.9

Table 2. Load data in August 2020

Date	Quy Nhon		Phu Cat	
	P_max	P_min	P_max	P_min
Sat, 01/08	66.3	50.4	24.9	14.1
Sun, 02/08	67.4	46.8	21.7	14.6
Mon, 03/08	78.1	48.1	24.7	12.3
Tue, 04/08	77	49.9	26.8	13.2
Wed, 05/08	77.4	49.8	30.2	15.3
Thu, 06/08	79.6	48.8	26.2	14
Fri, 07/08	69.6	47.4	24.6	12.8
Sat, 08/08	70.3	43.6	25.5	13
Sun, 09/08	68.5	43.0	23.2	13.7
Mon, 10/08	79.2	46.8	26.8	12
Tue, 11/08	78.7	46.9	27.1	16.2
Wed, 12/08	77.7	51.7	27.9	15.9
Thu, 13/08	78.1	50.3	27.3	14.6
Fri, 14/08	79.5	50.7	22.1	14.4
Sat, 15/08	75.5	52.0	26.6	13.3
Sun, 16/08	72.3	46.8	21.2	12.2
Mon, 17/08	78.6	51.0	29.7	13.5
Tue, 18/08	82.2	49.0	26.3	15.5
Wed, 19/08	77.9	51.1	26.2	13.5
Thu, 20/08	73.6	49.5	24.7	15.2
Fri, 21/08	74.3	46.7	26.5	13.5
Sat, 22/08	71.7	39.6	24.9	13.8
Sun, 23/08	75.6	50.3	21.1	14.9
Mon, 24/08	86.9	55.5	27.1	12.4
Tue, 25/08	84.9	53.2	29.7	14.5
Wed, 26/08	88.9	59.8	26.6	16.6
Thu, 27/08	88.1	55.9	26.1	16.3
Fri, 28/08	94.4	59.7	28.3	15.2
Sat, 29/08	86.8	59.4	28.4	16.4
Sun, 30/08	73.7	54.6	24.2	14.2
Mon, 31/08	79.5	49.7	26.8	12.6

In order to estimate the short-term load demand of Quy Nhon distribution network and Phu Cat distribution network, statistical MINITAB software and the MATLAB software are used in this paper. The estimated parameters of ARIMA models by using MINITAB software

for short-term load forecasting with P_max and P_min of Quy Nhon distribution network and Phu Cat distribution network in February and August 2020 are provided in Tables 3 and 4, respectively.

Table 3. The estimated parameters of ARIMA models for short-term load forecasting of Quy Nhon distribution network in February and August 2020

Load	Estimated parameters			
	p	d	q	Iteration
P_max (February)	1	0	3	19
P_min (February)	1	0	4	25
P_max (August)	4	0	3	21
P_min (August)	1	0	4	25

Table 4. The estimated parameters of ARIMA models for short-term load forecasting of Phu Cat distribution network in February and August 2020

Load	Estimated parameters			
	p	d	q	Iteration
P_max (February)	2	0	3	25
P_min (February)	2	0	3	19
P_max (August)	5	0	2	25
P_min (August)	4	0	2	25

Artificial neural networks with one input layer, one hidden layer, and one output layer are used to forecast short-term load demand of Quy Nhon distribution network and Phu Cat distribution network in this paper. The parameters of the trained neural networks by using MATLAB software for short-term load forecasting with P_max and P_min of Quy Nhon distribution network and Phu Cat distribution network in February and August 2020 are provided in Tables 5 and 6, respectively.

Table 5. The parameters of the trained neural networks for short-term load forecasting of Quy Nhon distribution network in February and August 2020

Load	Trained parameters		
	Hidden neuron	Training algorithm	Epoch
P_max (February)	22	trainlm	1
P_min (February)	25	trainrp	20
P_max (August)	25	trainbr	2
P_min (August)	30	trainbr	2

Table 6. The parameters of the trained neural networks for short-term load forecasting of Phu Cat distribution network in February and August 2020

Load	Trained parameters		
	Hidden neuron	Training algorithm	Epoch
P_max (February)	13	trainlm	3
P_min (February)	13	trainlm	3
P_max (August)	30	trainrp	29
P_min (August)	11	trainlm	28

The evaluation criteria of ARIMA model and neural network in short-term load forecasting (P_max) of Quy Nhon distribution network in February are illustrated in Table 7.

Table 7. Evaluation criteria of ARIMA model and neural network in short-term load forecasting (P_max) of Quy Nhon distribution network in February

Criteria	ARIMA model	Neural network
MAE	1.7099	0.8210
MAPE	2.8034	1.3409
MSE	4.7860	1.9393

In this case, the evaluation criteria values including MAE (1.7099), MAPE (2.8034), MSE (4.7860) of ARIMA model and MAE (0.6842),

MAPE (1.3409), MSE (1.9393) of neural network are relatively small. These results showed the effectiveness of both methods using short-term load forecasting. However, the neural network-based forecasting method provided the better solution compared to the ARIMA model based on the statistical criteria. The difference between the actual values and the forecasted values of P_max of Quy Nhon distribution network by using ARIMA model and neural network in February is demonstrated in Figure 2.

In Figure 2, the solid line shows the load values, the dashed – dot line indicates the forecasted values by using ARIMA model and the dashed line indicates the forecasted values by using neural network. In this figure, the forecasted values by using neural network are closer to the load values than the forecasted values by using ARIMA model. This demonstrates the effectiveness of neural network in short-term load forecasting in this case.

The evaluation criteria of ARIMA model and neural network in short-term load forecasting (P_min) of Quy Nhon distribution network in February are illustrated in Table 8.
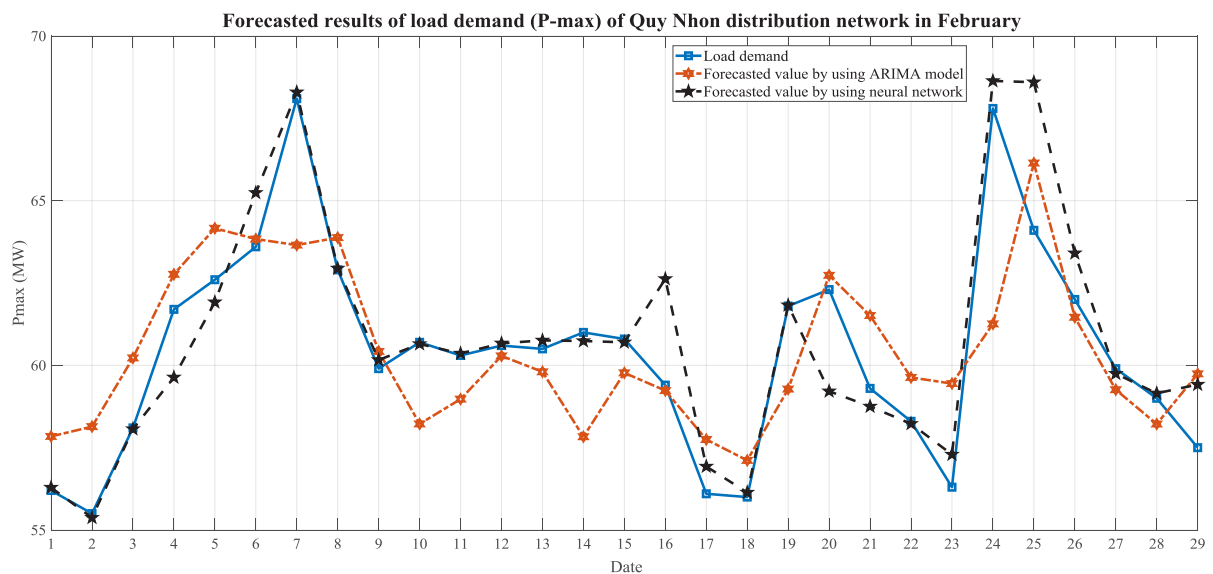

Figure 2. The forecasted results of load demand (P_max) of Quy Nhon distribution network by using ARIMA model and neural network in February
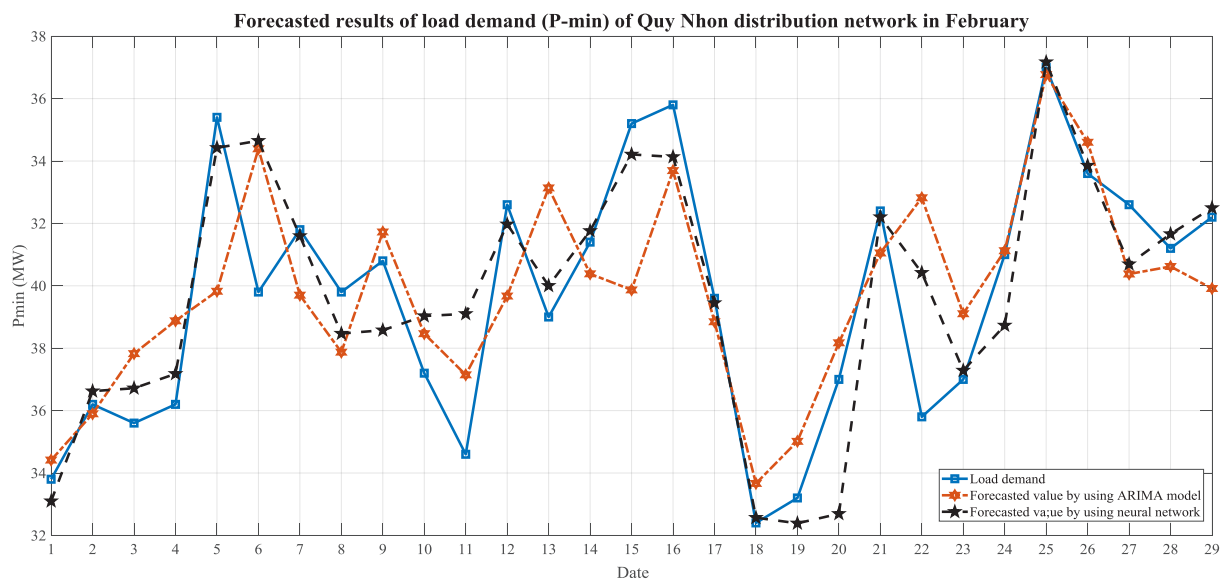
Figure 3. The forecasted results of load demand (P_min) of Quy Nhon distribution network by using ARIMA model and neural network in February

Table 8. Evaluation criteria of ARIMA model and neural network in short-term load forecasting (P_min) of Quy Nhon distribution network in February

Criteria	ARIMA model	Neural network
MAE	1.0723	0.6842
MAPE	2.9915	1.9396
MSE	1.8565	0.9734

In this case, the evaluation criteria values including MAE (1.0723), MAPE (2.9915), MSE (1.8565) of ARIMA model and MAE (0.6842), MAPE (1.9396), MSE (0.9734) of neural network are relatively small. These results also showed the effectiveness of both methods using short-term load forecasting. However, the neural network-based forecasting method provided the better solution compared to the ARIMA model based on the statistical criteria. The difference between the actual values and the forecasted values of P_min of Quy Nhon distribution network by using ARIMA model and neural network in February is demonstrated in Figure 3.

In Figure 3, the solid line shows the load values, the dashed – dot line indicates the forecasted values by using ARIMA model and the dashed line indicates the forecasted values by using neural network. In this figure, the forecasted values by using neural network are closer to the load values than the forecasted values by using ARIMA model. This demonstrates the effectiveness of neural network in short-term load forecasting in this case.

The evaluation criteria of ARIMA model and neural network in short-term load forecasting (P_max) of Quy Nhon distribution network in August are illustrated in Table 9.

Table 9. Evaluation criteria of ARIMA model and neural network in short-term load forecasting (P_max) of Quy Nhon distribution network in August

Criteria	ARIMA model	Neural network
MAE	3.6034	1.7853
MAPE	4.6312	2.2412
MSE	20.0097	6.0907

In this case, the evaluation criteria values including MAE (3.6034), MAPE (4.6312), MSE (20.0097) of ARIMA model and MAE (1.7853), MAPE (2.2412), MSE (6.0907) of neural network are relatively small. These results also showed the effectiveness of both methods using short-term load forecasting. However,

the neural network-based forecasting method provided the better solution compared to the ARIMA model based on the statistical criteria. The difference between the actual values and the forecasted values of P_max of Quy Nhon distribution network by using ARIMA model and neural network in August is demonstrated in Figure 4.

Figure 4. The forecasted results of load demand (P_max) of Quy Nhon distribution network by using ARIMA model and neural network in August

Figure 5. The forecasted results of load demand (P_min) of Quy Nhon distribution network by using ARIMA model and neural network in August

Figure 6. The forecasted results of load demand (P_max) of Phu Cat distribution network by using ARIMA model and neural network in February

In Figure 4, the solid line shows the load values, the dashed – dot line indicates the forecasted values by using ARIMA model and the dashed line indicates the forecasted values by using neural network. In this figure, the forecasted values by using neural network are closer to the load values than the forecasted values by using ARIMA model. This demonstrates the effectiveness of neural network in short-term load forecasting in this case.

The evaluation criteria of ARIMA model and neural network in short-term load forecasting (P_min) of Quy Nhon distribution network in August are illustrated in Table 10.

Table 10. Evaluation criteria of ARIMA model and neural network in short-term load forecasting (P_min) of Quy Nhon distribution network in August

Criteria	ARIMA model	Neural network
MAE	2.4062	0.9738
MAPE	4.9078	1.8997
MSE	10.5720	2.4585

In this case, the evaluation criteria values including MAE (2.4062), MAPE (4.9078), MSE (10.5720) of ARIMA model and MAE (0.9738),

MAPE (1.8997), MSE (2.4585) of neural network are relatively small. These results also showed the effectiveness of both methods using short-term load forecasting. However, the neural network-based forecasting method provided the better solution compared to the ARIMA model based on the statistical criteria. The difference between the actual values and the forecasted values of P_min of Quy Nhon distribution network by using ARIMA model and neural network in August is demonstrated in Figure 5.
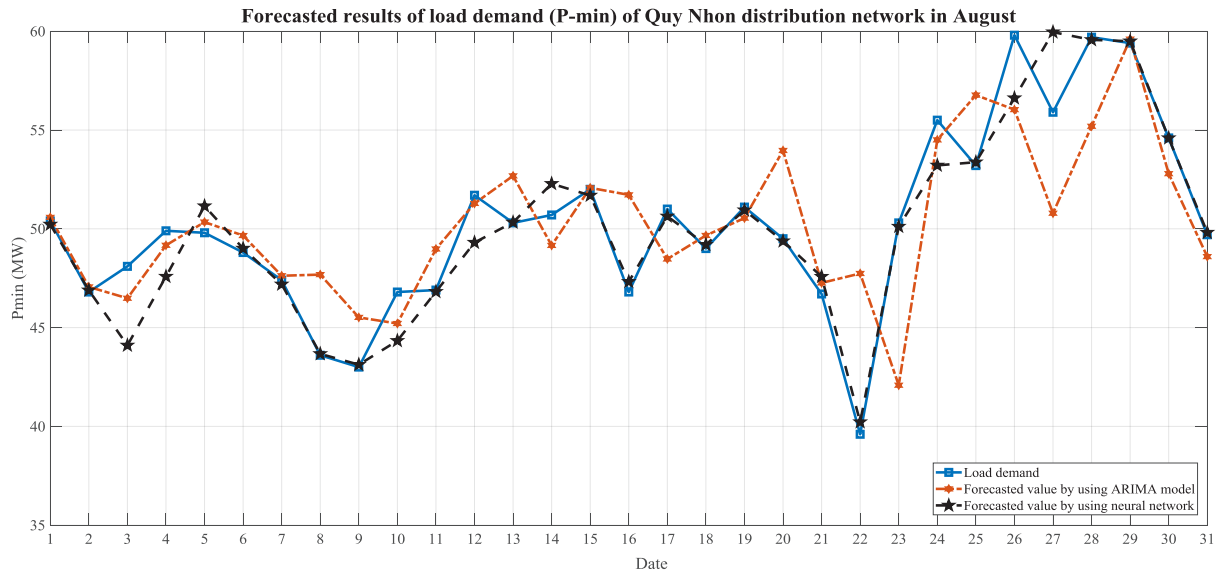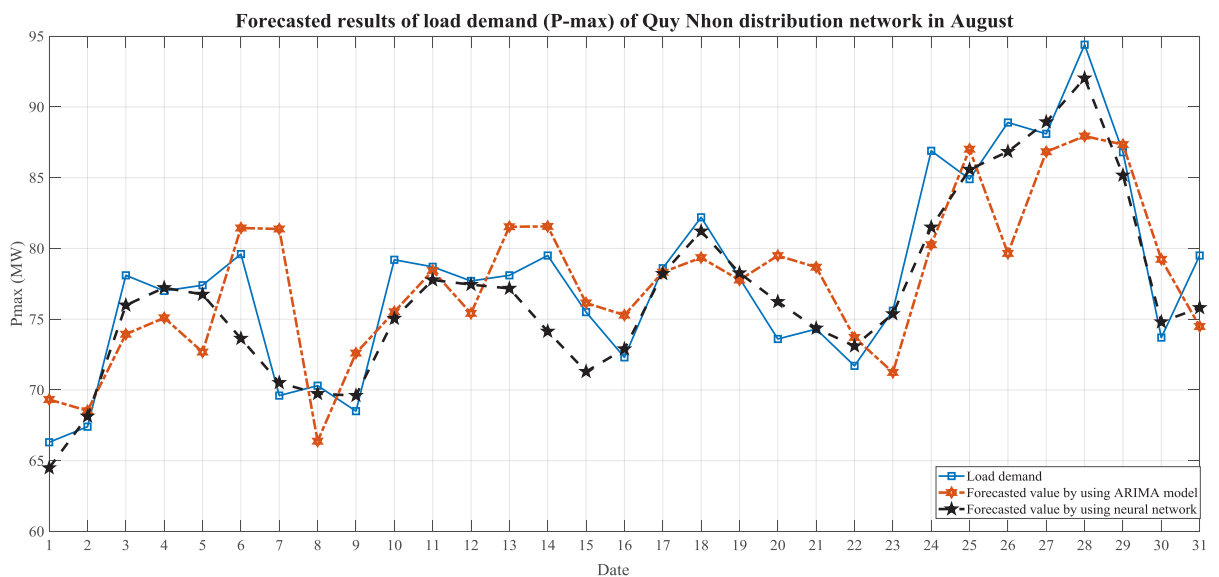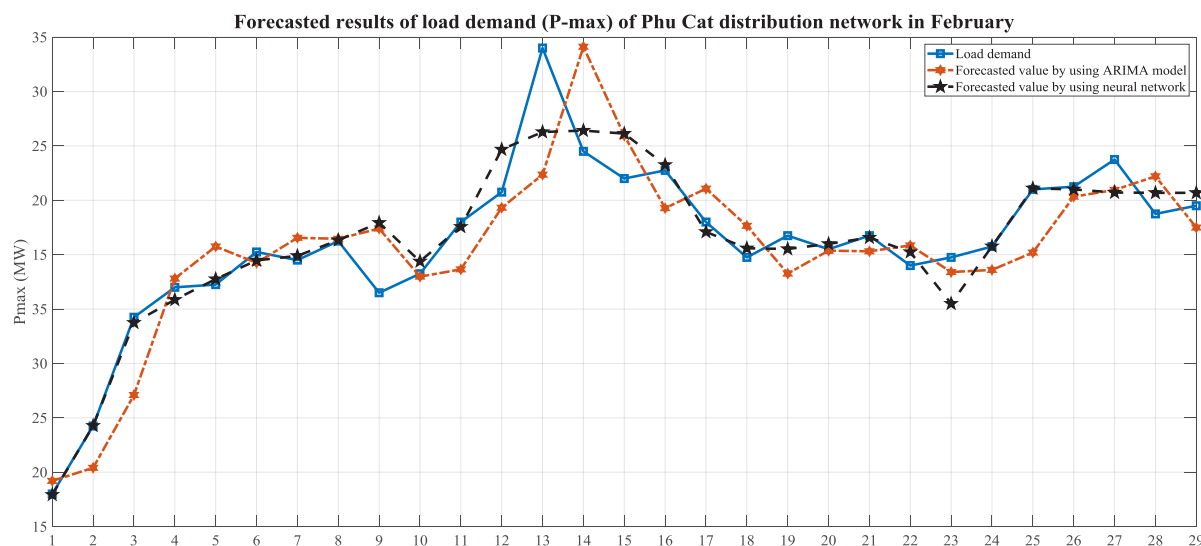
In Figure 5, the solid line shows the load values, the dashed – dot line indicates the forecasted values by using ARIMA model and the dashed line indicates the forecasted values by using neural network. In this figure, the forecasted values by using neural network are closer to the load values than the forecasted values by using ARIMA model. This demonstrates the effectiveness of neural network in short-term load forecasting in this case.

The evaluation criteria of ARIMA model and neural network in short-term load forecasting (P_max) of Phu Cat distribution network in February are illustrated in Table 11.

Table 11. Evaluation criteria of ARIMA model and neural network in short-term load forecasting (P_max) of Phu Cat distribution network in February

Criteria	ARIMA model	Neural network
MAE	1.2655	0.6257
MAPE	5.0768	2.4340
MSE	2.7436	0.9866

In this case, the evaluation criteria values including MAE (1.2655), MAPE (5.0768), MSE (2.7436) of ARIMA model and MAE (0.6257), MAPE (2.4340), MSE (0.9866) of neural network are relatively small. These results also showed the effectiveness of both methods using short-term load forecasting. However, the neural network-based forecasting method provided the

better solution compared to the ARIMA model based on the statistical criteria. The difference between the actual values and the forecasted values of P_min of Quy Nhon distribution network by using ARIMA model and neural network in August is demonstrated in Figure 6.

In Figure 6, the solid line shows the load values, the dashed – dot line indicates the forecasted values by using ARIMA model and the dashed line indicates the forecasted values by using neural network. In this figure, the forecasted values by using neural network are closer to the load values than the forecasted values by using ARIMA model. This demonstrates the effectiveness of neural network in short-term load forecasting in this case.

Figure 7. The forecasted results of load demand (P_min) of Phu Cat distribution network by using ARIMA model and neural network in February

The evaluation criteria of ARIMA model and neural network in short-term load forecasting (P_min) of Phu Cat distribution network in February are illustrated in Table 12.

Table 12. Evaluation criteria of ARIMA model and neural network in short-term load forecasting (P_min) of Phu Cat distribution network in February

Criteria	ARIMA model	Neural network
MAE	1.0147	0.4955
MAPE	9.1955	4.3096
MSE	1.5324	0.5663

In this case, the evaluation criteria values including MAE (1.0147), MAPE (9.1955), MSE (1.5324) of ARIMA model and MAE (0.4955), MAPE (4.3096), MSE (0.5663) of neural network are relatively small. These results also showed the effectiveness of both methods using short-term load forecasting. However, the neural network-based forecasting method provided the better solution compared to the ARIMA model based on the statistical criteria. The difference between the actual

values and the forecasted values of P_min of Phu Cat distribution network by using ARIMA model and neural network in February is demonstrated in Figure 7.

In Figure 7, the solid line shows the load values, the dashed – dot line indicates the forecasted values by using ARIMA model and the dashed line indicates the forecasted values by using neural network. In this figure, the forecasted values by using neural network are closer to the load values than the forecasted values by using ARIMA model. This demonstrates the effectiveness of neural network in short-term load forecasting in this case.
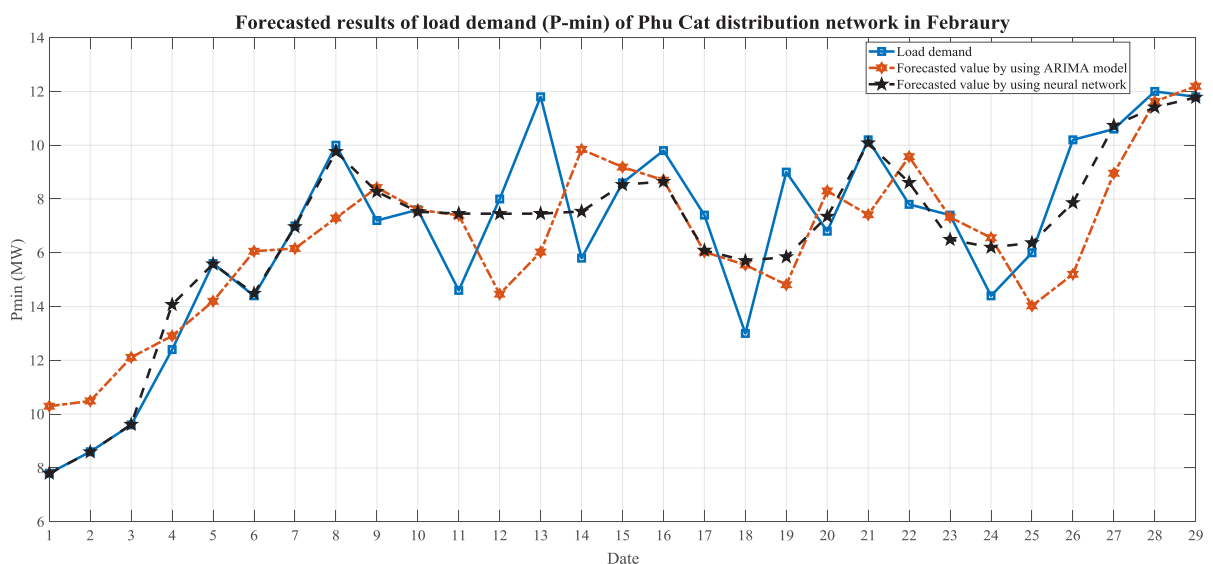
The evaluation criteria of ARIMA model and neural network in short-term load forecasting (P_max) of Phu Cat distribution network in August are illustrated in Table 13.

Table 13. Evaluation criteria of ARIMA model and neural network in short-term load forecasting (P_max) of Phu Cat distribution network in August

Criteria	ARIMA model	Neural network
MAE	1.3281	1.1770
MAPE	5.2385	4.6501
MSE	2.6991	2.6431

In this case, the evaluation criteria values including MAE (1.3281), MAPE (5.2385), MSE (2.6991) of ARIMA model and MAE (1.1770), MAPE (4.6501), MSE (2.6431) of neural network are relatively small. These results also showed the effectiveness of both methods using short-term load forecasting. However, the neural network-based forecasting method provided the better solution compared to the ARIMA model based on the statistical criteria. The difference between the actual values and the forecasted values of P_max of Phu Cat distribution network by using ARIMA model and neural network in August is demonstrated in Figure 8.

Figure 8. The forecasted results of load demand (P_max) of Phu Cat distribution network by using ARIMA model and neural network in August

Forecasted results of load demand (P-min) of Phu Cat distribution network in August

Figure 9. The forecasted results of load demand (P_min) of Phu Cat distribution network by using ARIMA model and neural network in August

In Figure 8, the solid line shows the load values, the dashed – dot line indicates the forecasted values by using ARIMA model and the dashed line indicates the forecasted values by using neural network. In this figure, the forecasted values by using neural network are closer to the load values than the forecasted values by using ARIMA model. This demonstrates the effectiveness of neural network in short-term load forecasting in this case.

The evaluation criteria of ARIMA model and neural network in short-term load forecasting (P_min) of Phu Cat distribution network in August are illustrated in Table 14.

Table 14. Evaluation criteria of ARIMA model and neural network in short-term load forecasting (P_min) of Phu Cat distribution network in August

Criteria	ARIMA model	Neural network
MAE	0.8583	0.5591
MAPE	6.0931	4.0552
MSE	1.2093	0.6976

In this case, the evaluation criteria values including MAE (0.8583), MAPE (6.0931), MSE (1.2093) of ARIMA model and MAE (0.5591), MAPE (4.0552), MSE (0.6976) of neural network are relatively small. These results also

showed the effectiveness of both methods using short-term load forecasting. However, the neural network-based forecasting method provided the better solution compared to the ARIMA model based on the statistical criteria. The difference between the actual values and the forecasted values of P_min of Phu Cat distribution network by using ARIMA model and neural network in August is demonstrated in Figure 9.
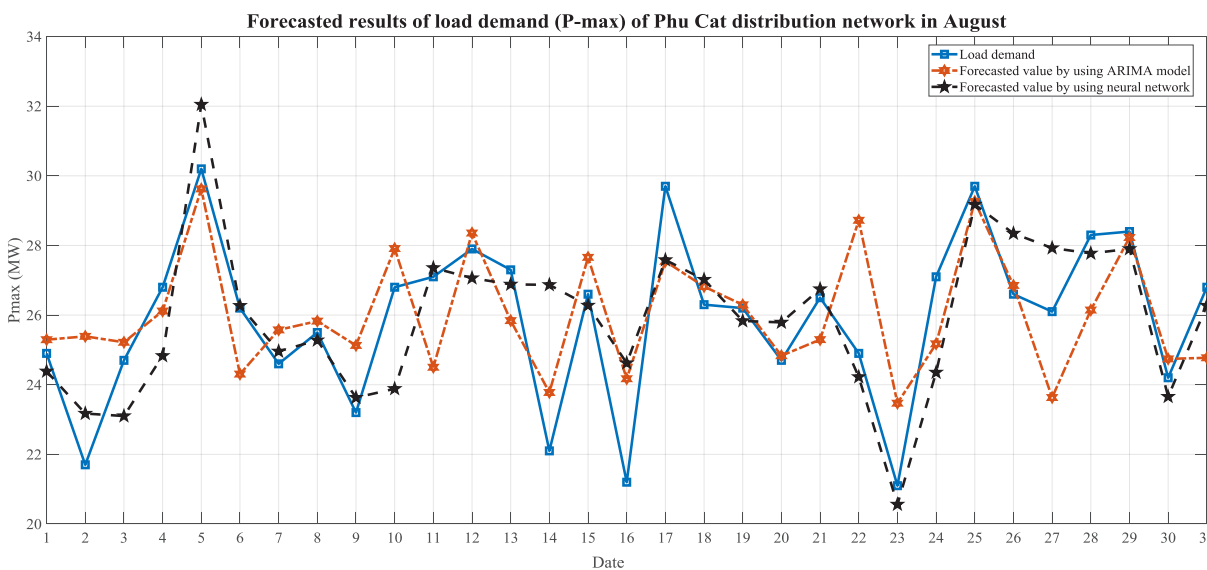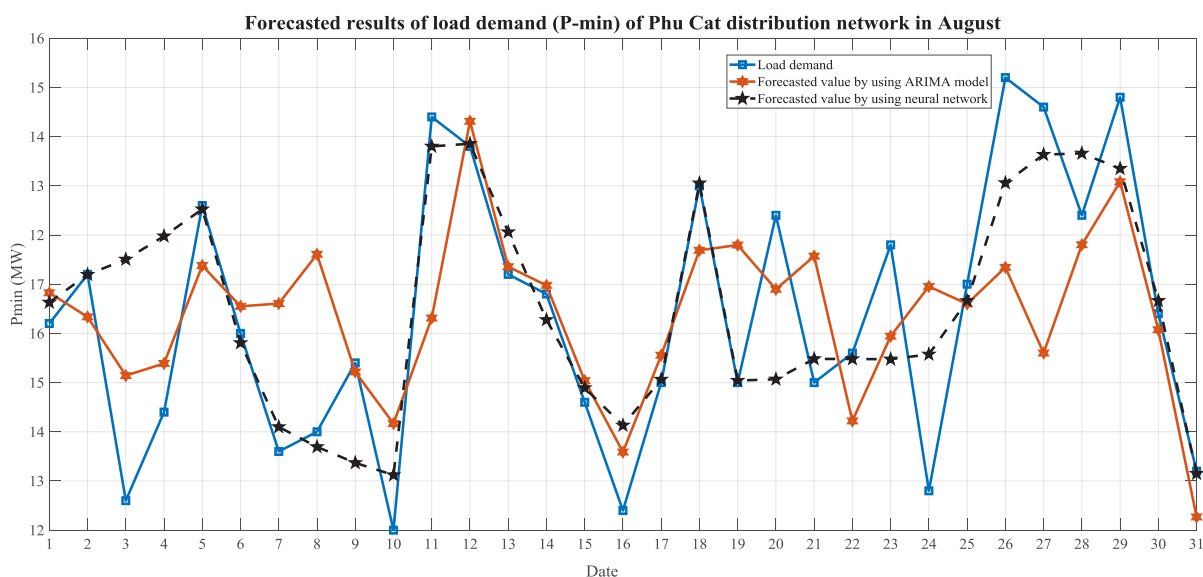
In Figure 9, the solid line shows the load values, the dashed – dot line indicates the forecasted values by using ARIMA model and the dashed line indicates the forecasted values by using neural network. In this figure, the forecasted values by using neural network are closer to the load values than the forecasted values by using ARIMA model. This demonstrates the effectiveness of neural network in short-term load forecasting in this case.

Generally, neural network-based forecasting method provides better solutions in short-term load forecasting compared to ARIMA model in all case studies.

3. CONCLUSION

In this paper, two forecasting methods including ARIMA model and neural network were utilized

in short-term load forecasting of Quy Nhon and Phu Cat distribution networks. These networks have the fastest load growth rates of Binh Dinh Power Company. Maximum load demand and minimum load demand in February and August are used in this paper. The results show that the neural network-based method provides better short-term load forecasting solutions compared to ARIMA model.

For further studies, the two methods can be combined in order to provide better solutions. In addition, the optimal design of neural network structure and ARIMA model is also a fruitful research direction.

REFERENCE

1. N. Amral, C. S. Ozveren, D. King. Short term load forecasting using multiple linear regression, In *2007 42ⁿᵈ international universities power engineering conference*, **2007**, 1192-1198.

2. T. Haida, S. Muto. Regression based peak load forecasting using a transformation technique, *IEEE transactions on power systems*, **1994**, *9*(4), 1788-1794.

3. D. Asber, S. Lefebvre, J. Asber, M. Saad, & C. Desbiens. Non-parametric short-term load forecasting, *International journal of electrical power & energy systems*, **2007**, *29*(8), 630-635.

4. C. M. Lee, C. N. Ko. Short-term load forecasting using lifting scheme and ARIMA models, *Expert systems with applications*, **2011**, *38*(5), 5902-5911.

5. J. F. Chen, W. M. Wang, C. M. Huang. Analysis of an adaptive time-series autoregressive moving-average (ARMA) model for short-term load forecasting, *Electric power systems research*, **1995**, *34*(3), 187-196.

6. S. J. Kiartzis, A. G. Bakirtzis, V. Petridis. Short-term load forecasting using neural networks, *Electric power systems research*, **1995**, *33*(1), 1-6.

7. D. K. Ranaweera, N. F. Hubele, G. G. Karady. Fuzzy logic for short term load forecasting, *International journal of electrical power & energy systems*, **1996**, *18*(4), 215-222.

8. M. Mohandes. Support vector machines for short-term electrical load forecasting, *International journal of energy research*, **2002**, *26*(4), 335-345.

9. C. C. Chiu, D. F. Cook, J. L. Kao, Y. C. Chou. Combining a neural network and a rule-based expert system for short-term load forecasting, *Computers & industrial engineering*, **1997**, *32*(4), 787-797.

10. G. C. Liao. Hybrid chaos search genetic algorithm and meta-heuristics method for short-term load forecasting, *Electrical engineering*, **2006**, *88*(3), 165-176.

11. Binh Dinh power company, https://pcbinhdinh.cpc.vn, accessed on 05/09/2020.

12. G. Box and Jenkin. *Time series analysis, Forecasting and control*, 4 ed., San Francisco: Holden-Day, 1970.

Nghiên cứu chế độ làm việc của máy phát điện cảm ứng kích từ kép khi có ngắn mạch trên lưới gần nhà máy điện gió

Trần Dương Hoàng Phúc, Lê Thái Hiệp*

Khoa Kỹ thuật và Công nghệ, Trường Đại học Quy Nhơn, Việt Nam

TÓM TẮT

Bài báo này nghiên cứu về chế độ làm việc của máy phát điện gió loại máy phát điện cảm ứng kích từ kép (DFIG) để đánh giá khả năng vượt qua sự cố thoáng qua trên lưới điện gần nhà máy. Dựa trên cấu tạo của máy phát điện loại DFIG, việc sử dụng điện trở nối trực tiếp với dây quấn rôto sẽ đưa máy phát hoạt động như một máy phát điện không đồng bộ rôto dây quấn (WRIG) khi có ngắn mạch trên lưới. Theo kết quả mô phỏng trên Matlab thì, khi đó công suất tác dụng được tiêu thụ trên điện trở phụ crowbar làm cho đặc công suất phát chuyển đổi từ cao sang thấp. Nhờ đó lượng công suất cơ dư thừa không nhiều, cho nên máy phát không bị tăng tốc đáng kể. Kết quả mô phỏng này cho thấy việc sử dụng điện trở phụ crowbar để thay đổi đặc tính công suất của DFIG là phù hợp. Chính nhờ cách chuyển đổi này giúp máy phát vẫn kết nối với lưới, vận hành ổn định cả trong và sau sự cố ngắn mạch.

Từ khóa: *Máy phát điện gió, máy phát điện cảm ứng kích từ kép (DFIG), máy phát điện không đồng bộ rôto dây quấn (WRIG), ngắn mạch, crowbar.*

*****Tác giả liên hệ chính.*
Email: lethaihiep@qnu.edu.vn

Study on operating modes of doubly fed induction generator with a short circuit fault on grid near the wind power plant

Tran Duong Hoang Phuc, Le Thai Hiep*

Faculty of Engineering and Technology, Quy Nhơn University, Viet Nam

ABSTRACT

In this paper, the operating mode of a doubly fed induction generator (DFIG) wind turbine is studied in order to evaluate its fault ride-through and transient stability with a grid's short circuit fault at near the wind power plant. Based on the structure of DFIG, external resistors are directly connected to rotor windings, then the generator operates as a wound rotor induction generator (WRIG) when there is a short circuit fault on the grid. According to the simulation results in Matlab, the active power is consumed on the crowbar resistor, causing the active power characteristic of generator changing from high to low. As a result, the amount of excess mechanical energy is not much, so the generator is not accelerated significantly. These simulation results show that it is appropriate to use the crowbar resistor to change the power characteristic of the DFIG. Thanks to this change, the generator is still connected to the grid, and operares stably during and after a short circuit.

Keywords: *Wind power generator, doubly fed induction generator (DFIG), wound rotor induction generator (WRIG), short circuit fault, crowbar.*

1. INTRODUCTION

Electricity is mainly generated by hydroelectric and thermal power using fossil fuels. Currently fossil fuels are increasingly depleted resulting in rising the cost of the products using them. To solve this difficulty, one seeks to replace them by other energy sources, such as solar, wind energy. Wind energy is one of the clean energy researched and applied in the field of electricity generation.

However, during operation of wind power plant, it is inevitable that there is a short circuit outside one. At this time, the wind generators are not allowed to disconnect from the grid in order to participate in supporting this grid to ride through the fault. Doubly Fed Induction Generator (DFIGs), which are variable - speed wind generations, are commonly used in the world, and used at all wind power plants in Vietnam. DFIG's properties is not similar to synchronous generators' ones (synchronous generators are used in hydropower, thermal power, diesel power…). Therefore, it is necessary to have a detailed study of the characteristics and operating modes of the wind generator when there is a short circuit outside the wind power plant.

This problem is expected to give some solutions, to help wind power plants operate safely and stability. Many studies have shown that it is necessary to use a crowbar resistance for DFIG when there is a short circuit.[1-4] There have also been researches indicating how to control for DFIG wind generators to ride-through grid

---

Corresponding author.
Email: lethaihiep@qnu.edu.vn

faults,[1,3-5] for transient stability improvement in grid.[6] Besides, the effects of crowbar resistor on DFIG's power curve have been analyzed.[1] In Vietnam, there have also been research on voltage instability at grid connected wind power plants.[7] However, there has not yet been a detailed review of the state of the power system to consider whether to improve or deteriorate when DFIGs are connected to it. This paper presents research with the aim of finding the answers to the above problems.
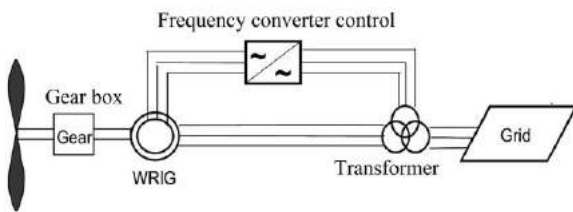
2. THE WIND POWER GENERATOR

2.1. Wind power generator

Figure 1. Basic structure of the DFIG wind turbine. [8-10]

Commonly, a DFIG wind turbine is designed on basic structure as shown in Figure 1 and control structure as shown in Figure 2. The generator is an induction machine with a wound rotor, which is connected via a back-to-back converter, while the stator is directly connected to the grid. The rotor-side converter (RSC) is connected to the grid-side converter (GSC) using a DC link.[8]
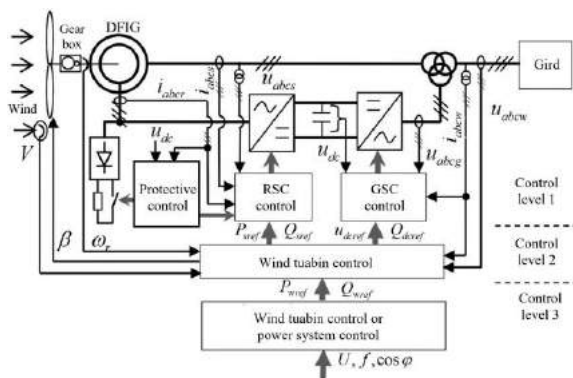

Figure 2. Basic configuration of a DFIG wind turbine connected to a power grid.[11,12]

2.2. Wind power generator model

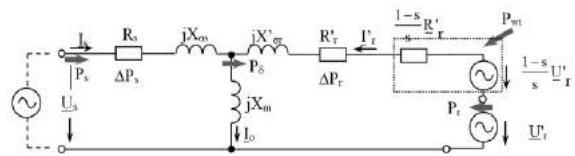The equivalent circuit of DFIG is shown in Figure 3.

Figure 3. Power flow in the DFIG is illustrated with the equivalent circuit. [9]

From the equivalent circuit, the following voltage equations can be written:

$$\underline{U}_s = R_s \underline{I}_s + jX_{\sigma s}\underline{I}_s + jX_m \underline{I}_0 \qquad (1)$$

$$\frac{\underline{U}'_r}{s} = \frac{R'_r}{s}\underline{I}'_r + jX'_{\sigma r}\underline{I}'_r + jX_m\underline{I}_0 \qquad (2)$$

With:

U_s – stator voltage

I_s – stator current

U'_r – rotor voltage related to stator side

I'_r – rotor current related to stator side

R_s – stator winding resistance

R'_r – rotor resistance related to stator side

$X_{\sigma s}$ – stator leakage reactance

$X'_{\sigma r}$ – rotor leakage reactance related to stator side

X_m – magnetizing reactance

s – slip

In Figure 3: ΔP_s, ΔP_r – stator winding losses and rotor winding losses; P_s, P_r – stator power and rotor power; P_{wt} – mechanical power, P_δ – air gap power.

Equation (3) shows the power transmitted through the air gap calculated according to the mechanical power received from the turbine.

$$\begin{aligned} -P_\delta &= P_{wt} + 3\Re e\{\underline{U}'_r \underline{I}'^*_r\} - 3R'_r |\underline{I}'_r|^2 \\ &= P_{wt} + P_r - \Delta P_r \end{aligned} \qquad (3)$$

With:

$\Re\{\underline{X}\}$ – Real part of complex numbers $\underline{X}$;

$\underline{X}^*$ – complex number with $\underline{X}$;

$|\underline{X}|$ – module of complex number $\underline{X}$.

The air gap power is calculated according to the stator-side parameters:

$$P_\delta = P_s - 3R_s |\underline{I}_s|^2 = P_s - \Delta P_s \qquad (4)$$

On the other hand, P_δ can also be represented:

$$P_\delta = 3\frac{R'_r}{s}\left|\underline{I}'_r\right|^2 - 3\Re e\left\{\frac{\underline{U}'_r}{s}\underline{I}'^*_r\right\} \qquad (5)$$

From the above equations we can write:

$$s.P_\delta = 3R'_r\left|\underline{I}'_r\right|^2 - 3\Re e\left\{\underline{U}'_r\underline{I}'^*_r\right\} = \Delta P_r - P_r \qquad (6)$$

If we consider $\Delta P_r \approx s.\Delta P_s$, there is the following representation:

$$P_r = -s.P_s \qquad (7)$$

The mechanical power P_{wt} can be expressed with:

$$P_{wt} = 3\frac{1-s}{s}R'_r\left|\underline{I}'_r\right|^2 - 3\Re e\left\{\frac{1-s}{s}\underline{U}'_r\underline{I}'^*_r\right\} \qquad (8)$$

2.3. Operating mode

In subsynchronous operation the converter feeds power into the rotor. During oversynchronous operation, the rotor supplies power via the converter back to the grid.
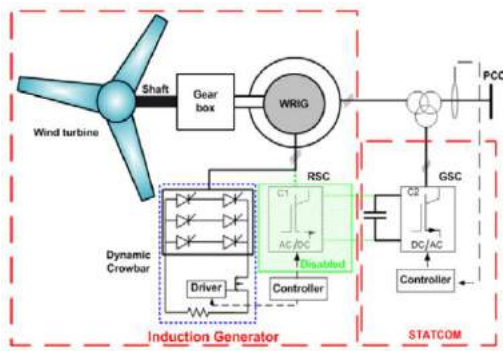

Figure 4. The method to control and operate the wind turbine DFIG when there is a short circuit fault on the grid.[1]

When there is a short circuit fault on grid near the wind power plant, most of the stator power will be consumed at this point and then voltage of the power system will unbalance. When there is a short circuit fault, the power electronics are controlled according to a completely different operating mode from normal operation (as shown in Figure 4). During short circuit fault, the GSC is controlled to support the reactive power demand of the grid as a reactive power source (as a STATCOM) and decoupled operation. The RSC is disabled. A resistor bank, which is commonly known as the crowbar protection, is connected to the rotor of DFIG as an WRIG. At the same time, the DFIG

power curve is changed to WRIG power curve (Figure 5).

The time of short circuit fault is not long enough for the wind speed and pitch angle to change. At the same time, the rotor is connected to the crowbar resistor, so the power in the rotor side (P_r) is consumed on these resistors. It is this reason that the active power characteristic of the WRIG passes through zero at the synchronous speed and is lower than the power characteristic of the DFIG.

In Figure 5, the WRIG power curves will decrease gradually as the $R_{crowbar}$ increases gradually.
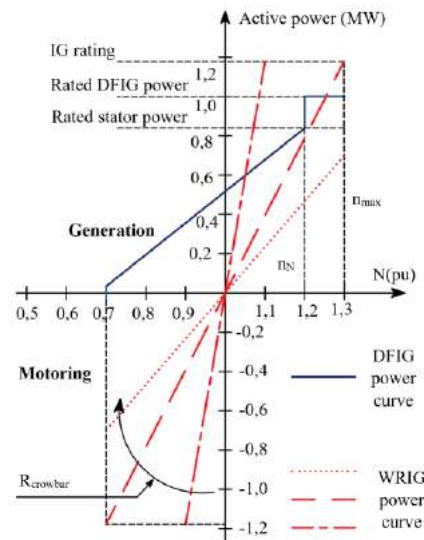
Figure 5. Active power characteristics of DFIG with crowbar resistor connected to rotor in case of short circuit fault on the grid.[1]

3. SIMULATION AND EVALUATION OPERATING MODE OF WIND POWER GENERATOR

3.1. Simulation operating mode of wind power generator with a short circuit fault on grid near the wind power plant

The wind generators at Phuong Mai 3 wind power plant are selected in this paper to survey operating mode of wind power generators in case of short circuit fault on the grid near this plant.

The wind generators in Phuong Mai 3 are DFIG in accordance with the study of the paper.

Table 1. Specification of wind turbine at Phương Mai 3 wind power plant.

Manufacturer	GAMESA EOLICA S.A.U	
Type of generator	DFIG	
Model	CR33-6P	
Stator connection	Δ	
Rotor connection	Y	
Rated voltage	690 V	
Rated frequency	50 Hz	
Rated speed	1120 rpm	
Maximum speed	1800 rpm	
Rated power	3465 kW	
Rated power	3450 kW	3615 kW
Power factor	0,95	0,9842
	1	1
	0,95	0,9842
Max. amb . temp	35 ºC	30 ºC
Short – circuited power	3200 kW	
Short – circuited power factor	0.88	
Poles Nº	6	
Momen of inertia	300 kgm²	

Data of wind power simulation in Matlab is shown in Table 1.
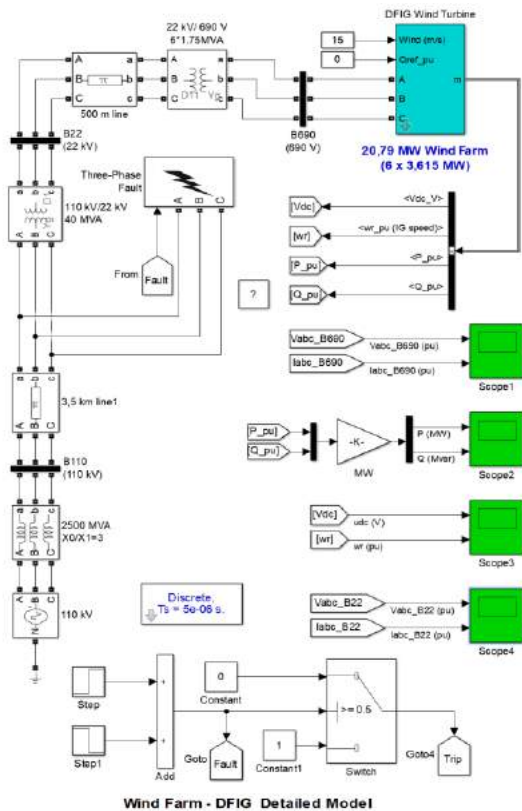
Figure 6. The wind power system simulated in Matlab/ Simulink.
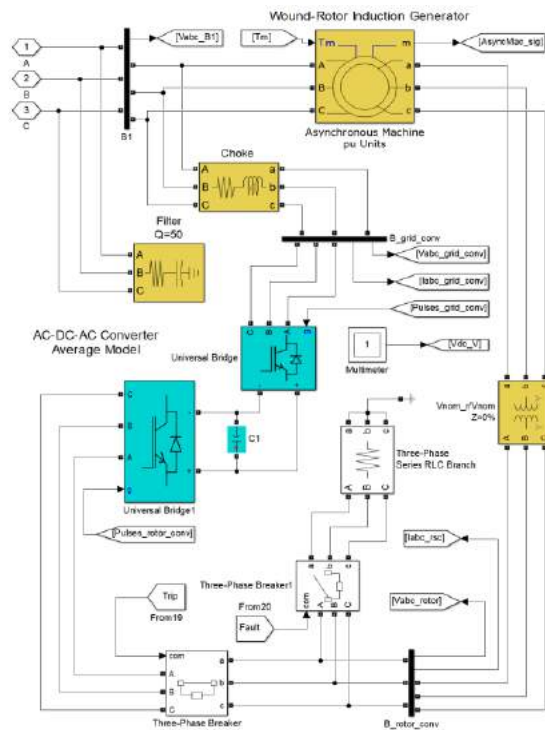
Figure 7. The DFIG with the rotor connected to crowbar resistor.

In the simulation (Figure 6), there are 6 wind turbines and the total active power is 20,79 MW. The output voltage of all generators is 690V. These poles are connected to a 22kV system via a 22kV / 690V transformer. Then the 22kV system is connected to a 110kV system through a 110kV / 22kV transformer. The length of 110kV line to the connection point is 3.5 km. The grid in the simulation has a frequency of 50Hz.

In this simulation model, an operation method as shown in section 2.3 (as shown in Figure 7) is used. This simulation is intended to evaluate low voltage ride-through fault and transient stability.

3.2. Results and discussion

Operating modes of wind power generators are simulated in 5s. The time of short circuit fault on the grid is 0,25s and the wind speed is 15m/s.

Figure 8 and Figure 9 show the power, voltage, current of DFIG when it has a short circuit fault on grid near the wind power plant.

Figure 8 shows that operating mode of DFIG is changed. Hence, the low voltage fault of the grid is supported to ride-through. So, the rotor is connected to crowbar resistor is a useful solution. In addition, the voltage of the grid is recovered quickly after short circuit fault is cleared.

Power characteristics (in Figure 9) in interval from 0.2s to 0.25s show that the active power was dissipated in the crowbar resistor. Therefore, the speed of rotor is controlled at the appropriate value as the speed characteristic (in Figure 10). This operation method makes the system easy to ensure transient stability.
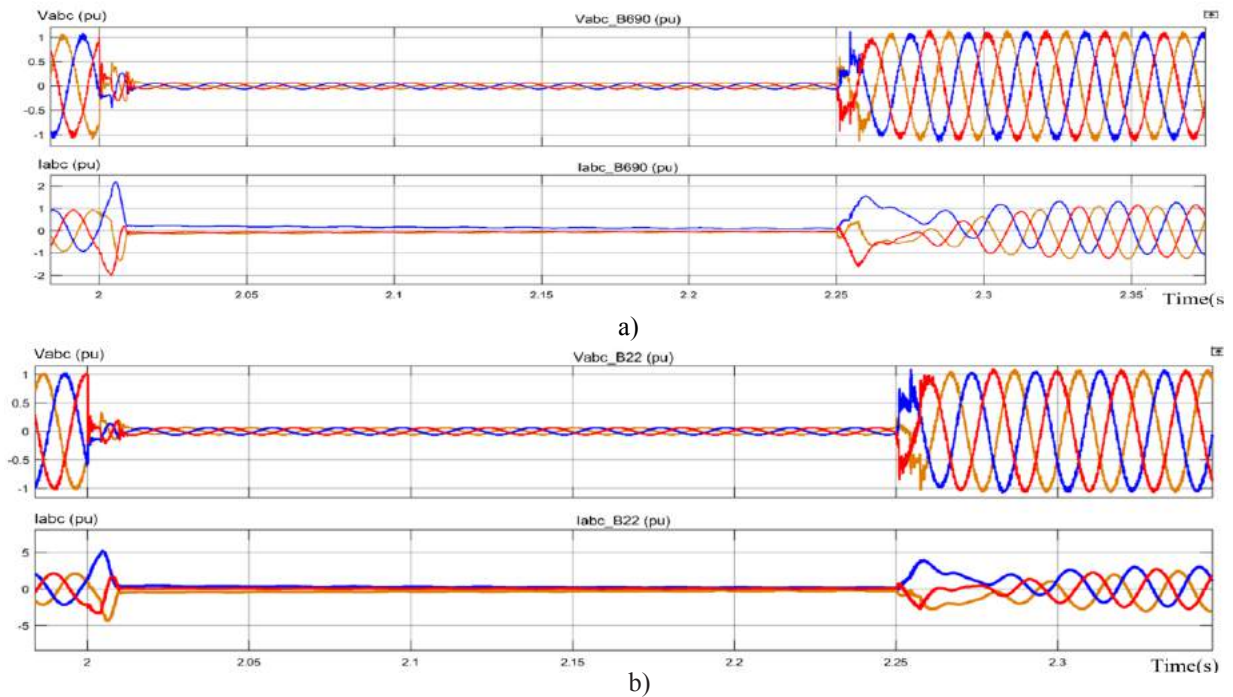

Figure 8. a) Line-voltage and line-current in busbar B690; b) Line-voltage and line-current in busbar B22.
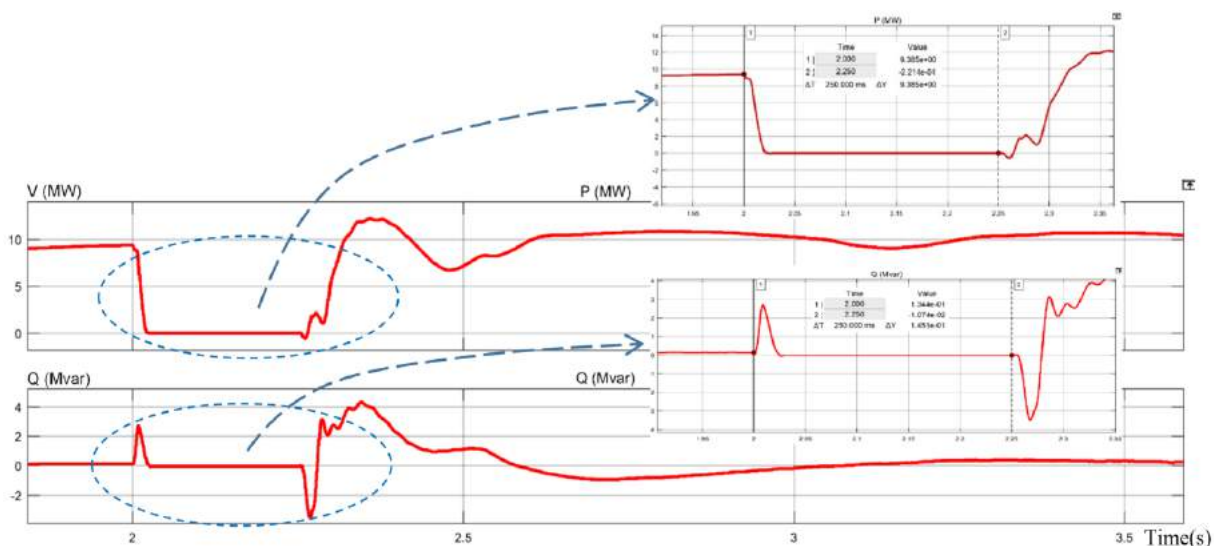

Figure 9. Active power curve and reactive power curve when short circuit fault on grid near the wind power plant.
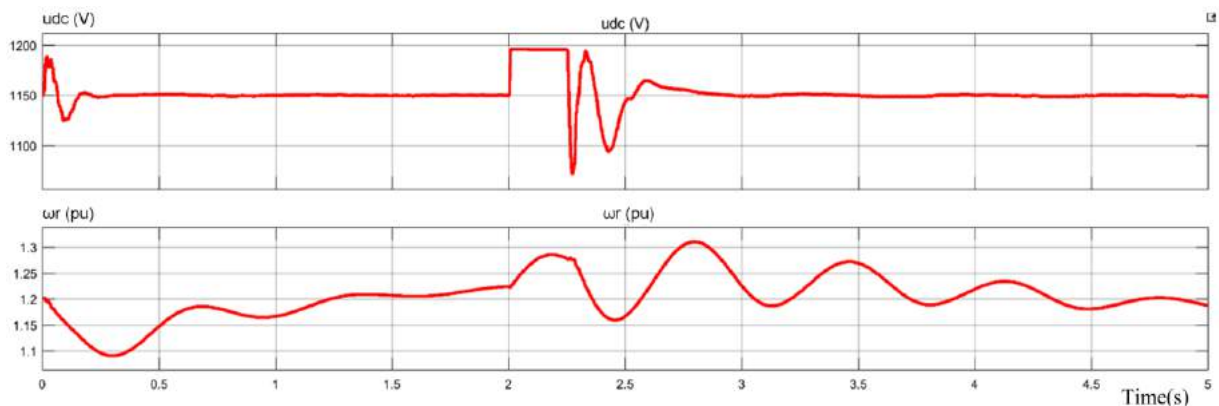
Figure 10. Voltage curve in capacitor u_{dc} and rotor speed curve.

According to Figure 9, power curve is changed to a new steady state, drop a lot from 2s to 2,25s and restore the state almost before the short circuit fault. The time to restore the state is short, so the wind generators are not cut off from the grid and ready to work again after short circuit fault is cleared.

Besides, during the short circuit fault, the GSC supplies reactive power to grid for the purpose of improving stability of this grid. This result is shown in voltage curve u_{dc} at capacitor (Figure 10) and reactive power curve Q (Figure 9).

Other parameters such as voltage and current are also changed a lot. In Figure 8, the voltage curve drops so much, at the same time the current is fluctuated but it keeps low (different from current is height of normal short circuit). This is the result of the transition from DFIG to WRIG. This helps the system minimize the adverse impact when height current flowing in electrical equipment in power systems and fault point.

To optimize the efficiency of operations of the wind turbine at the time short circuit fault on grid near the wind power plant, other parts of it are calculated and controlled according to measuring equipment in this turbine.

When the short circuit fault is cleared, the power system is kept working and ensure service reliability. According to these simulation results, the new operating mode is different from the first one, but it is not much and it assures service reliability.

4. CONCLUSIONS

The paper has analyzed the operation method of DFIG in modes before, during and after a short circuit fault. The special feature of this operation method is that during a short circuit fault, the DFIG is converted to WRIG by the crowbar resistor connected to the rotor and the RSC is disabled.

In the paper, this operation method is tested by simulation on Matlab/ Simulink. The simulation results show that:

- It is this conversion that the amount of active power transmitted to the grid is reduced to a very low level. As a result, the short-circuit current is limited and the rotor speed increases only within the permissible range.

- Thanks to this operation method, generators support the grid to ride through the low voltage fault and ensures good transient stability. Thanks to this, after the fault is cleared, the system quickly achieves a pre-fault operating state.

The results of the paper contribute to the affirmation that the wind generators in the wind power plants can support good transient stability and contribute to reliable grid operation.

REFERENCES

1. L. Meegahapola, T. Littler, D. Flynn. Decoupled-DFIG fault ride-through strategy for enhanced stability performance during grid faults, *IEEE transactions on sustainable energy,* **2010**, *1*(3), 152–162.

2. P. Huang, M. S. E. Moursi, and S. A. Hasen. Novel Fault Ride-Through Scheme and Control Strategy for Doubly Fed Induction Generator-Based Wind Turbine, *IEEE transactions on energy conversion*, **2015**, *30*(2), 635–645.

3. M. Hossain, M. H. Ali. Transient stability improvement of doubly fed induction generator based variable speed wind generator using DC resistive fault current limiter, *IET renewable power generation*, **2016**, *10*(2), 150 – 157.

4. S. M. Ali, M. Jawad, Z. Ullah, B. Khan. Fault-ride-through schemes of grid-interfaced DFIG: a comparative study under symmetrical grid faults, *2017 International symposium on recent advances in electrical engineering (RAEE)*, Islamabad, Pakistan, 2017.

5. R. Islam, J. Hasan, R. R. Shipon, M. A. H. Sadi, A. Abuhussein, and T. K. Roy. Neuro fuzzy logic controlled parallel resonance type fault current limiter to improve the fault ride through capability of DFIG based wind farm, *IEEE access*, **2020**, *8*, 115314–115334.

6. M. Q. Duong, F. Grimaccia, S. Leva, M. Mussetta, and K. H. Le. A hybrid fuzzy-pi cascade controller for transient stability improvement in DFIG wind generators, *2016 IEEE international conference on fuzzy systems (FUZZ-IEEE)*, Vancouver, BC, Canada, **2016**, 1733–1739.

7. T. T. Chuong. Study of voltage collapse charactiristics in grid connected wind power plant, *Science & technology development*, *14*(K2- 2011), 80–93.

8. G. Michalke. *Variable speed wind turbines - modelling, control, and impact on power systems*, PhD thesis, Riso National Laboratory, Denmark, 2008.

9. V. Akhmatov. *Analysis of dynamic behaviour of electric power systems with large amount of wind power*, Technical University of Denmark, 2003.

10. A. D. Hansen, F. Iov, F. Blaabjerg, L. H. Hansen. Review of contemporary wind turbine concepts and their market penetration. *Wind engineering*, **2004**, *28*(3), 247–263.

11. A. D. Hansen, G. Michalke. Fault ride-through capability of DFIG wind turbines, *Sciencedirect*, **2007**, *32*, 1594–1610.

12. P. Tourou, C. Sourkounis. *Review of control strategies for DFIG-based wind turbines under unsymmetrical grid faults*, 2014 Ninth International conference on ecological vehicles and renewable energies (EVER), IEEE, Monaco, 2014, 1–9.

Nghiên cứu chế tạo và tính chất quang của cấu trúc nano phân nhánh ZnO/NiO

Nguyễn Ngọc Khoa Trường, Nguyễn Minh Vương[*]

Khoa Khoa học tự nhiên, Trường Đại học Quy Nhơn, Việt Nam

TÓM TẮT

Vật liệu ZnO/NiO có cấu trúc nano phân nhánh được tổng hợp bằng việc kết hợp giữa các phương pháp phun tĩnh điện, thủy nhiệt và lắng đọng hỗ trợ quang. Ban đầu, sợi ZnO nano được tổng hợp bằng phương pháp phun tĩnh điện rồi oxy hóa nhiệt. Sau đó, ZnO cấu trúc nano phân nhánh được tổng hợp bằng phương pháp thủy nhiệt. Cuối cùng, ZnO/NiO cấu trúc nano phân nhánh được tổng hợp bằng phương pháp lắng đọng hỗ trợ quang nhờ tia cực tím. Đặc trưng về hình thái, cấu trúc và tính chất của vật liệu được xác định nhờ ảnh hiển vi điện tử quét (SEM), phổ tán sắc theo năng lượng (EDS), phổ nhiễu xạ tia X (XRD), phổ quang điện tia X (XPS), phổ huỳnh quang (PL). Kết quả cho thấy vật liệu thu được có cấu trúc nano phân nhánh, tinh thể ZnO có cấu trúc lục giác và không có sự hình thành pha mới của NiO. Phổ huỳnh quang của vật liệu cho thấy có sự dịch chuyển đỉnh phát xạ về phía bước sóng dài hơn trong vùng nhìn thấy khi lắng đọng NiO.

Từ khóa: *ZnO/NiO, cấu trúc nano phân nhánh, tính chất quang.*

---

[*]*Tác giả liên hệ chính.*
Email: nguyenminhvuong@qnu.edu.vn

Fabrication and optical properties of NiO/ZnO hierarchical nanostructures

Nguyen Ngoc Khoa Truong, Nguyen Minh Vuong[*]

Faculty of Natural Science, Quy Nhon University, Vietnam

ABSTRACT

NiO/ZnO hierarchical nanostructures were synthesized by a combination of electrospinning, hydrothermal and ultraviolet (UV)-assisted deposition. Initially, ZnO nanofibers were synthesized by electrospinning method following thermal oxidation. Subsequently, ZnO hierarchical nanostructures were synthesized by hydrothermal method using ZnO nanofibers as templates. Finally, NiO nanoparticles were deposited on ZnO surface by UV-assisted deposition method. Morphology and characteristics of the material were determined by scanning electron microscopy (SEM), energy dispersion spectroscopy (EDS), X-ray diffraction (XRD), X-ray photoelectron spectrum (XPS) and photoluminescence spectrum (PL). The results showed that the NiO/ZnO hierarchical nanostructures with high open space were obtained. NiO/ZnO crystals showed hexagonal structure of ZnO without phase formation of NiO. PL spectra of the NiO/ZnO material showed emission peaks shift towards longer wavelengths in the visible region with increasing the content of NiO nanoparticles.

Keywords: *ZnO/NiO, hierarchical nanostructure, optical properties.*

1. INTRODUTION

Semiconductor materials in general and metal-semiconductor oxides (SMOs) in particular have been attracting great interest due to their advantages such as relatively simple fabrication, good stability, low cost, small size... Therefore, over the past decades, SMOs materials such as SnO_2, ZnO, CuO, V_2O_5, WO_3, In_2O_3, TiO_2... have been widely studied for the development of electronic, sensitive components gas.[1] Among SMOs, ZnO is preferred in many studies because of its advantages such as simple syntheses, low cost and low crystallization temperature.[2] In addition, the surface modification of ZnO materials by other materials results in improvement of the optical properties of the

material. Recently, the optical properties, conductivity and surface catalytic properties of ZnO nanomaterials have been changed thanks to the surface modification of ZnO with other components such as metal nanoparticles (Au, Ag, Pt, Pd...) or metal oxides (NiO, CuO...).[2-6] R. Elilarassi *et al.* synthesized Ni-doped ZnO nanoparticles by "explosive method" at low temperature. The PL spectra of Ni doped ZnO showed a shift from the blue emission peak to the red emission peak.[7] Y. Wang *et al.* fabricated spherical Ni-doped ZnO material with an average diameter of 3 μm by heating a mixture of ZnO and Nickel citrate at 500 °C for 2 hours. The results showed that ZnO/Ni material had higher photocatalytic activity compared to pure ZnO.[8]

[*]Corresponding author.
Email: nguyenminhvuong@qnu.edu.vn

W. Wang *et al.* synthesized ZnO/Ni nanorods on Si substrate by magnetic sputtering combined with hydrothermal at 100 °C. PL spectra of ZnO/Ni nanorods showed a narrow band in the UV region with an emission peak at 370 nm and a wide band in the yellow-green region with a peak at 560 nm. Compared with the pure ZnO, the emission peak intensity of ZnO/Ni in the UV region decreases as the concentration of doped Ni increases.[9]

Currently, there were several ways to fabricate ZnO nanostructure materials such as physical vapor deposition (PVD), chemical vapor deposition (CVD), solution method, electrospinning method, hydrothermal method, etc. In this paper, the NiO/ZnO hierarchical nanostructures were fabricated by combining electrospinning following oxidation, hydrothermal and UV-assisted deposition.

2. EXPERIMENTAL

2.1. Synthesis of ZnO nanofibers

ZnO nanofibers were synthesized by electrospinning method on Al_2O_3 sensing substrate, zinc acetatedihydrate (ZnAc) and polyvinylpyrrolidone (PVP) were dissolved in a solvent N-dimethylformamide (DMF) and ethanol. The solution was stirred during 6 hours. The solution was injected into a syringe and sprayed at a rate of 0.01 mL/hour. Al_2O_3 substrate was heated at 90°C using DC power supply; Nozzle and sample holders were connected to a DC voltage of 12 kV at distance of 12 cm. ZnAc/PVP nanofibers formed on the Al_2O_3 substrate were oxidized in an air environment at 500°C for 2 hours at a heating rate of 1°C/min to remove PVP and form ZnO nanofibers on the sensing substrate.

2.2. Synthesis of ZnO hierarchical nanostructure

ZnO hierarchical nanostructure was synthesized by hydrothermal method. The substrates containing ZnO nanofibers were placed in a mixture of zinc nitratehexahydrate ($Zn(NO_3)_2.6H_2O$) and hexamethylenetetramine (HMTA) in a 1:1 ratio that was hydrated at 90°C for 4 hours. ZnO nanofibers act as the seed for ZnO nanorods to grow around the ZnO nanofiber. After the hydrothermal process, ZnO hierarchical nanostructure on the substrate was obtained.

2.3. Synthesis of ZnO/NiO hierarchical nanostructure

NiO/ZnO hierarchical nanostructures were synthesized by UV-assisted deposition in Ni salt solution. Nickel acetate (NiAc) salts were dissolved in an ethanol solvent at room temperature. The sensing substrates containing the ZnO hierarchical nanostructure were placed in the NiAc salt solution under UV irradiation at different times of 2, 4, 8, 16 and 24 minutes. Next, samples were taken out following dry process naturally and oxidation at 350 °C for 30 minutes at a heating rate of 5°C/min. Finally, samples were cooled to room temperature naturally to obtain NiO/ZnO hierarchical nanostructures.

2.4. Morphology and Characterization

The morphological, structural and optical properties of the fabricated samples were studied by field emission scanning electron microscopy (FE-SEM; JSM 700F; JEOL), Energy-dispersive X-ray spectroscopy (EDS), X-ray diffraction (XRD; D8 DISCOVER; Bruker AXS, Germany, with a Cu K radiation), X-ray photoelectron spectroscopy (XPS; VG Multilab 2000; ThermoVG Scientific, UK) and photoluminescence measurements using an FP-6500 spectrofluorometer (JASCO, Tokyo, Japan) utilizing an excited wavelength of 325 nm.

3. RESULTS AND DISCUSSION

Figure 1 shows SEM images with a magnification of × 100k of ZnO nanofiber (a) and hierarchical structures of ZnO (b) and NiO/ZnO with Ni deposition time of 16 min (c). Figure 1a shows the relatively uniform distribution of ZnO nanofibers, which was formed by the ZnO nanoparticles. The space between the nanofibers

is quite large. Figure 1b shows radial, symmetrical ZnO rods around ZnO fibers, with an average length of ~ 1μm and a relatively smooth surface. Figure 1c shows that the hierarchical structure of ZnO remains unchanged but the ZnO nanorods surface is slightly rough due to the deposition of NiO particles.
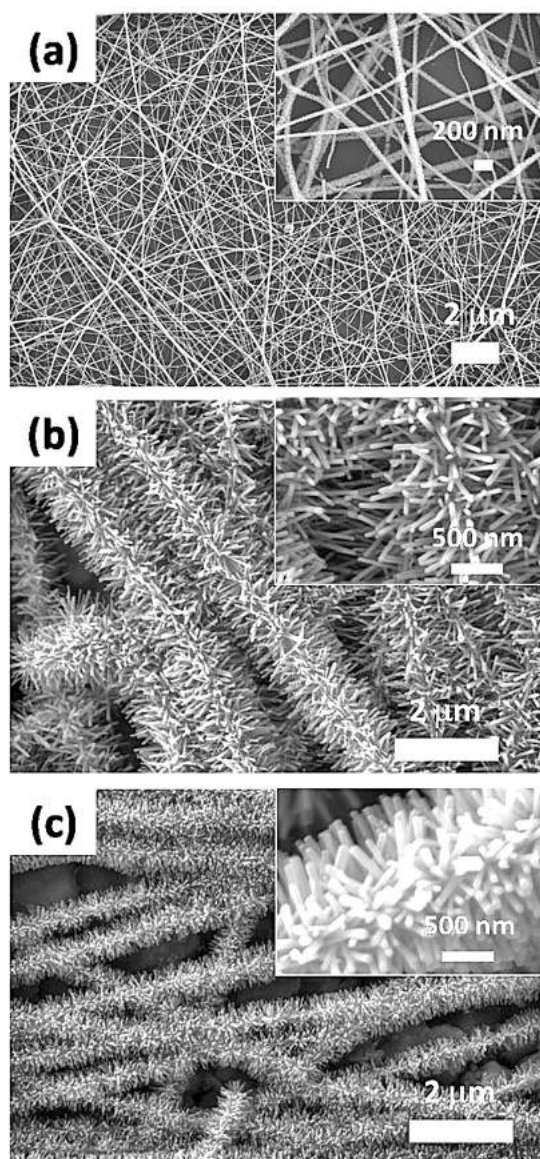

Figure 1. SEM images of ZnO nanofibers (a), ZnO hierarchical structures of pure ZnO (b) and NiO/ZnO with Ni deposition time of 16 minutes (c).

Figure 2 shows the spatial distribution of Zn, O, Ni elements and EDS spectrum of the NiO/ZnO hierarchical nanostructure with a NiO deposition time of 16 minutes. NiO/ZnO materials contain only the elements Zn, O and Ni. The elements Zn, O, Ni are distributed relatively evenly throughout the space of the material. This proves that the synthetic material is completely pure. The percentage content of O, Ni, Zn atoms in the sample are 48.56%, 0.61% and 50.83%, respectively. On another hand, the Ni content in the fabricated nanostructure is low in compared to Zn and O.
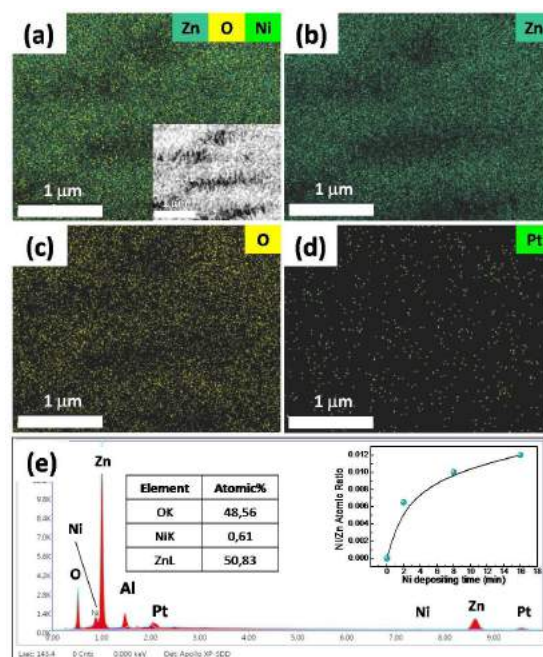
Figure 2. Distribution of the elements Zn, Ni and O (a), Zn (b), O (c), Ni (d) and EDS spectrum (e) of NiO(16)/ZnO nanostructure. Insert in (a) is the corresponding SEM image. Insert in (e) shows the dependence of the Ni/Zn atom ratio on the Ni deposition time determined from the EDS spectrum.

Figure 3 shows total XPS spectrum (a) and high magnification Ni2p (b) of NiO/ZnO hierarchical structure with Ni deposition time of 16 minutes. The composition and chemical states of the elements present in the NiO/ZnO sample show that the fabricated material contains only Zn, O, Ni and C. There are two peaks with strong strength at binding energies of 1020 eV and 1040 eV corresponds to the 2p3/2 and 2p1/2 state of Zn. Two peaks at the binding energies were located at 856 eV and 873 eV corresponding to the 2p3/2 and 2p1/2 states of Ni.
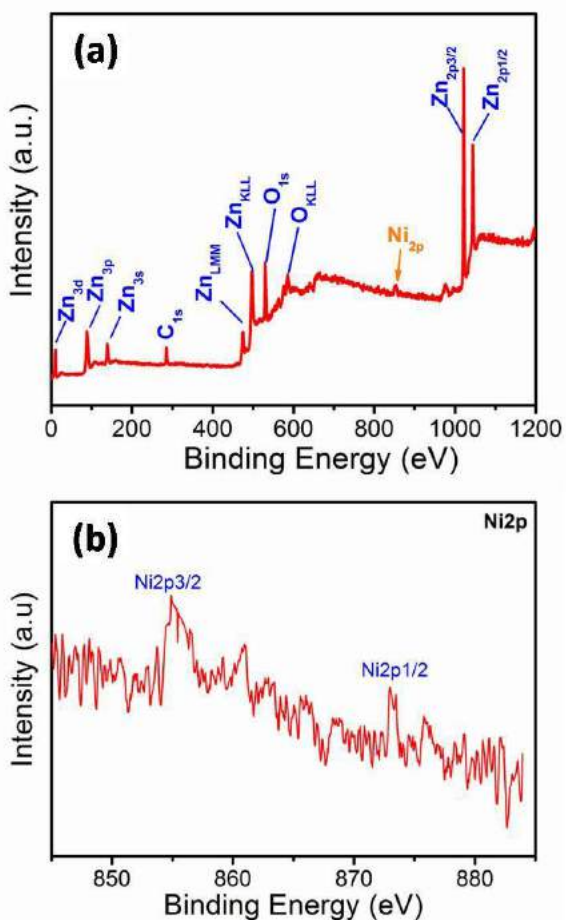
Figure 3. The total XPS spectrum (a) and high manification of Ni2p (b) in NiO(16)/ZnO structure.
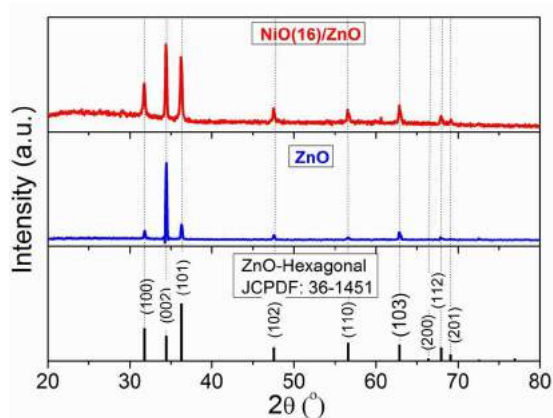
Figure 4. XRD spectrum of ZnO and NiO(16)/ZnO materials.

Figure 4 shows the X-ray diffraction spectrum (XRD) of ZnO and NiO/ZnO with a Ni deposition time of 16 minutes. Hierarchical structures of ZnO and NiO/ZnO showed the diffraction peaks corresponding to diffraction plans of (100), (002), (101), (102), (110), (103), (200), (112) and (201) (file JCPDF No. 36-1451). This result shows that ZnO has hexagonal structure with lattice constants of a = 3,294 Å and c = 5,206 Å. The fabricated structures show the diffraction peak with the strongest intensity at 2θ = 34,5°. This indicates that the growth of ZnO is highly oriented in the direction <002>. The NiO/ZnO structure did not see the diffraction peak of NiO. This can be explained by the low NiO concentration of this sample which is not enough to cause appearance of the diffraction peaks.

Figure 5 shows the PL spectra of ZnO and NiO/ZnO nanostructures with NiO deposition times of 2 minutes, 8 minutes and 16 minutes under the 325 nm excitation wavelength at 300 K. PL spectra of ZnO and NiO/ZnO materials include a narrow emission band in the ultraviolet region and a wide emission band in the visible light. The emission peak at 380 nm is considered to be the characteristic emission peak of ZnO related to the band - band recombination. At the wavelength value of this emission peak, we can estimate the band gap of ZnO and NiO/ZnO materials to be about 3.26 eV. Emission in the visible region is believed to originate from lattice defects such as: vacancy oxygen (V_O), interstitial oxygen (O_i), vacancy zinc (V_{Zn}), interstitial zinc (Zn_i)...

Figure 5. PL spectrum of ZnO (a), NiO(2)/ZnO (b), NiO(8)/ZnO (c) and NiO(16)/ZnO (d) materials.

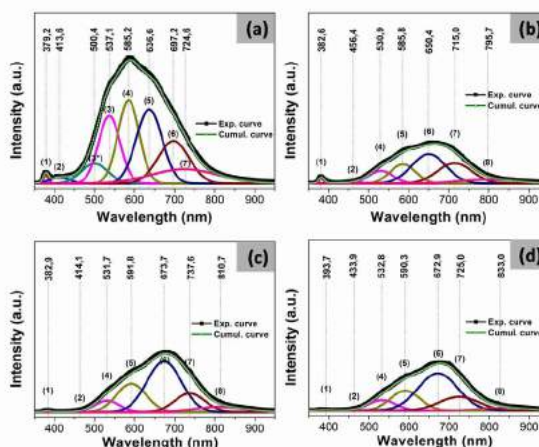The PL intensity of NiO/ZnO hierarchical structures is lower than that of the ZnO hierarchical structure. This is explained by the deposition of NiO particles (p-type semiconductor) on the surface of the ZnO rods (n-type semiconductor) forming a p-n junction, which prevents the recombination of photogenerated electrons and holes. The results show that the NiO deposition time prolong causing the decreasing of the intensity of emission peak in the UV region. Moreover, the spectral peak in the visible region is reduced and shifted towards longer wavelengths. The emission peaks is located at 650.4 nm, 673.7 nm and 672.9 nm for structures of NiO(2)/ZnO, NiO(8)/ZnO and NiO(16)/ZnO. NiO(8)/ZnO shows the strongest emissive peak intensity in the visible light region. This is explained by the increasing of donor impurity levels due to the formation of oxygen vacancies on the ZnO surface during NiO deposition.

4. CONCLUSION

NiO/ZnO hierarchical nanostructures were synthesized by electrospinning, hydrothermal and UV-assisted deposition. The study results showed that when ZnO was decorated by NiO nanoparticles, the morphology and structure of the material were not changed compared to pure ZnO nanostructure but the optical properties of the material changed significantly. The emission peaks shifted towards longer wavelengths in the visible light region with increasing the NiO deposition time on the ZnO surface. The emission peak intensity in visible region is the highest as NiO deposition time of 8 minutes. This opens up the application direction of NiO/ZnO materials for optoelectronic devices.

REFERENCES

1. A. Mirzaei, S. G. Leonardi, and G. Neri. Detection of hazardous volatile organic compounds (VOCs) by metal oxide nanostructures-based gas sensors: A review, *Ceramics international*, **2016**, *42*(14), 15119-15141.

2. N. M. Vuong, N. M. Chinh, N. H. T. Duc, Bui, and LeeYong-ill. CuO-decorated ZnO Hierarchical Nanostructures as efficient and established sensing materials for H_2S gas sensors, *Scientific report*, **2016**, *6*(1), 1-13.

3. Y. Xiao et al. Highly enhanced acetone sensing performances of porous and single crystalline ZnO nanosheets: High percentage of exposed (100) facets working together with surface modification with Pd nanoparticles, *ACS Applied Materials Interfaces*, **2012**, *4*(8), 3797-3804.

4. C. Liu et al. Acetone gas sensor based on NiO/ZnO hollow spheres: Fast response and recovery, and low (ppb) detection limit, *Journal of colloid and interface science*, **2017**, *495*, 207-215.

5. N. Kaur et al. Branch-like NiO/ZnO heterostructures for VOC sensing, *Sensors actuators B chemical*, **2018**, *262*, 477-485.

6. C. Liu et al, Facile synthesis and gas sensing properties of the flower-like NiO-decorated ZnO microstructures, *Sensors actuators B chemical*, **2016**, *235*, 294-301.

7. R. Elilarassi and G. Chandrasekaran, Synthesis and optical properties of Ni-doped zinc oxide nanoparticles for optoelectronic applications, *Optoelectronics letters*, **2010**, *6*(1), 0006-0010.

8. Y. Wang, T. Liu, Q. Huang, C. Wu, D. Shan. Synthesis and their photocatalytic properties of Ni-doped ZnO hollow microspheres, *Journal of materials research*, **2016**, *31*(15), 2317-2328.

9. W. Wang, S. Hui, F. Zhang, X. Wang, S. Zhang, J. Yan and W. Zhang. Fabrication and Study on Magnetic-Optical Properties of Ni-Doped ZnO Nanorod Arrays, *Micromachines*, **2019**, *10*(9), 1-11.

Chùm quỹ đạo tuần hoàn của một tự đẳng cấu hyperbolic trên xuyến $\mathbb{T}^2$

Huỳnh Minh Hiền*, Võ Văn Nam, Lê Tính, Nguyễn Thị Đài Trang

Khoa Toán và Thống kê, Trường Đại học Quy Nhơn, Bình Định, Việt Nam

TÓM TẮT

Bài báo nghiên cứu chùm quỹ đạo tuần hoàn của tự đẳng cấu T_A trên xuyến $\mathbb{T}^2$ cảm sinh bởi ma trận $A = \begin{bmatrix} 2 & 1 \\ 1 & 1 \end{bmatrix}$. Chúng tôi chứng minh T_A thỏa mãn tiêu đề A. Chùm quỹ đạo tuần hoàn của T_A được nghiên cứu thông qua khái niệm '*p-gần nhau*' giữa các dãy tuần hoàn của hệ động lực ký tự tương ứng. Chúng tôi cũng đưa ra số chùm tuần hoàn các dãy tuần hoàn có chu kỳ cho trước trong trường hợp *p-gần* nhau.

Từ khóa: *Chùm quỹ đạo tuần hoàn, tự đẳng cấu hyperbolic, động lực học ký tự, xuyến 2 chiều.*

---

*Tác giả liên hệ chính.
Email: huynhminhhien@qnu.edu.vn

Clustering of periodic orbits of a hyperbolic automorphism on the torus $\mathbb{T}^2$

Huynh Minh Hien, **Vo Van Nam, Le Tinh, Nguyen Thi Dai Trang**

Department of Mathematics and Statistics, Quy Nhon University, Binh Dinh, Vietnam

ABSTRACT

This paper deals with clustering of periodic orbits of the hyperbolic toral automorphism induced by matrix $A = \begin{bmatrix} 2 & 1 \\ 1 & 1 \end{bmatrix}$. We prove that T_A satisfies the Axiom A. The clustering of periodic orbits of T_A is investigated via the notion of 'p-closeness' of periodic sequences of the respective symbolic dynamical system. We also provide the number of clusters of periodic sequences with given periods in the case of 2-closeness.

Keywords: *Clustering of periodic orbits, hyperbolic toral automorphism, symbolic dynamics, 2-torus*

1. INTRODUCTION

Symbolic dynamics is a powerful tool to investigate general dynamical systems. A dynamical system having a Markov partition will be represented as a symbolic dynamical system, which is the shift map on a set of bi-infinite sequences of symbols.

The construction of Markov partition for Axiom A diffeomorphisms given by R. Bowen[1] has many applications. Working on symbolic dynamics has several advantages since the theory of symbolic dynamics is almost complete.[2] Furthermore, since subshift of finite types are related to adjacency matrices and digraphs, we have many choices of tools to work on symbolic dynamics.

Clustering of periodic orbits is a beautiful phenomenon. B. Gutkin and V.A. Osipov[3] show that periodic orbits of the baker's map form clusters and have hierarchical structures, using symbolic dynamics. The corresponding symbolic dynamics of the baker's map is trivial with no grammar rule, i.e., each symbol can be followed by any other symbols.

In this paper, we consider the automorphism on the 2-torus $\mathbb{T}^2 = \mathbb{R}^2/\mathbb{Z}^2$ induced by matrix $A = \begin{bmatrix} 2 & 1 \\ 1 & 1 \end{bmatrix}$. We prove that T_A is an Axiom A diffeomorhism[4] and introduce symbolic dynamics provided by L. Barreira.[5] The corresponding symbolic dynamics is a subshift of finite type. The adjacency matrix is a 5×5 matrix with entries 0 and 1. This means that the respective symbolic dynamics has forbidden sequences. A periodic orbit of

---

Corresponding author.
Email: huynhminhhien@qnu.edu.vn

T_A corresponds to a periodic sequence up to a shift cycle. This paper deals with the clustering of periodic orbit based on the notion of 'p-closeness' introduced by Gutkin and Osipov. This is an equivalence relation and groups periodic sequences into clusters. One cluster can involve one or many orbits. We give a necessary and sufficient condition for sequences to be in the same cluster.

This paper is organized as follows. In the next section, we present symbolic dynamics of T_A and prove that T_A satisfies Axiom A. Section 3 studies clusters of periodic orbits of T_A via the notion of p-closeness and provides the number of 2-clusters.

2. SYMBOLIC DYNAMICS OF T_A

Consider $T_A : \mathbb{T}^2 \to \mathbb{T}^2$ induced by matrix

$$A = \begin{bmatrix} 2 & 1 \\ 1 & 1 \end{bmatrix}, \text{ i.e.}$$

$$T_A(\mathsf{x}) = A\mathsf{x}, \text{ for all } \mathsf{x} \in \mathbb{T}^2.$$

The map T_A is a diffeomorhism on $\mathbb{T}^2$ and is called hyperbolic since matrix A has two eigenvalues

$$\lambda_1 = \frac{3+\sqrt{5}}{2} \quad \text{and} \quad \lambda_2 = \frac{3-\sqrt{5}}{2},$$

which are not in the unit circle. The corresponding eigenvectors are

$$u_1 = \left(\frac{1+\sqrt{5}}{2}, 1 \right) \text{ and } u_2 = \left(\frac{1-\sqrt{5}}{2}, 1 \right).$$

The unstable manifold (resp. stable manifold) at $\mathsf{x} = x+\mathbb{Z}^2 \in \mathbb{T}^2$ is the projection of the line in $\mathbb{R}^2$ passing through x and in direction u_1 (resp. u_2) on $\mathbb{T}^2$. Therefore, u_1 and u_2 are called unstable direction and stable direction, respectively.

The automorhism T_A is also called Arnold's cat map (see Figure 1). This map was used by Arnold and Avez[6] in 1968 to indicate ergodicity of the dynamical system. Later, people use 'CAT' to short for 'Continuous Automophirms on Torus'. The Arnold's cat map is also used to illustrate chaos property in chaos theory.
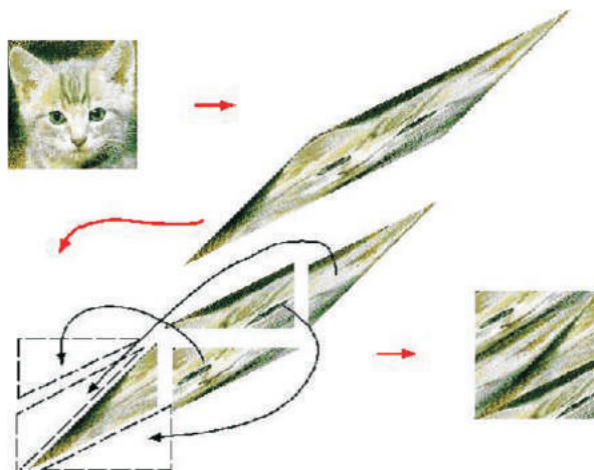
Figure 1. The Arnold's cat map

Next we recall some notions which will be used later. Let $f : M \to M$ is a diffeomorphism on a Riemannian manifold M.

Definition 2.1. A closed set $\Lambda \subset M$ is called *hyperbolic* if $f(\Lambda) = \Lambda$ and for $x \in \Lambda$, the tangent space $T_x M$ has the splitting

$$T_x M = E^u(x) \oplus E^s(x)$$

such that

(i) $d_x f\left(E^s(x)\right) = E^s\left(f(x)\right), d_x f\left(E^u(x)\right) = E^u\left(f(x)\right)$;

(ii) there exist $c > 0$ and $\lambda \in (0, 1)$ such that

$$\|d_x f^n(v)\| \le c\lambda^n \|v\|, \text{ khi } v \in E^s(x), n \ge 0$$

and

$$\|d_x f^{-n}(v)\| \le c\lambda^n \|v\|, \text{ khi } v \in E^u(x), n \ge 0;$$

If $\Lambda = M$ then we say f is hyperbolic.

Definition 2.2. A point $x \in M$ is called *non-wandering* if for any neighbourhood U of x, one has

$$U \bigcap \left(\bigcup_{n>0} f^n(U) \right) \neq \emptyset.$$

The set of non-wandering points of f is denoted by $\Omega(f)$.

Definition 2.3. A point $x \in M$ is called *periodic* if there exists $n > 0$ such that $f^n(x) = x$. The set of periodic points of f is denoted by $\mathcal{P}(f)$. Then x is called periodic with period n or n-periodic.

Proposition 2.1. $\overline{\mathcal{P}(f)} \subset \Omega(f)$.

Proof. Let $x \in \overline{\mathcal{P}(f)}$ and let U be a neighbourhood of x. Then there exists a point $y \in U \cap \mathcal{P}(f)$. Since y is a periodic point, there exists $n > 0$ such that $f^n(y) = y$. Then $y \in f^n(U)$ implies $y \in U \cap \left(\bigcup_{n>0} f^n(U) \right)$ or $U \cap \left(\bigcup_{n>0} f^n(U) \right) \neq \emptyset$. Hence $x \in \Omega(f)$.

$\square$

Proposition 2.2. [7] *The set of periodic of T_A is* $\mathcal{P}(T_A) = \mathbb{Q}^2/\mathbb{Z}^2$.

This implies that the set of periodic points of T_A is dense in $\mathbb{T}^2$.

Definition 2.4. The diffeomorphism f is said to satisfy the *Axiom A* if $\Omega(f)$ is a hyperbolic set and
$$\Omega(f) = \overline{\mathcal{P}(f)}.$$

Theorem 2.1. *The diffeomorphism T_A satisfies the Axiom A.*

Proof. According propositions 2.1 and 2.2,
$$\Omega(T_A) = \overline{\mathcal{P}(T_A)} = \mathbb{T}^2.$$

It remains to show that $\mathbb{T}^2$ is a hyperbolic set. For $x \in \mathbb{T}^2$, let $E^u(x) = < u_1 >$ and $E^s(x) = < u_2 >$, which are eigenspaces. Then
$$E^u(x) \oplus E^s(x) = \mathbb{R}^2 = T_x\mathbb{T}^2.$$

Let $L_A : \mathbb{R}^2 \to \mathbb{R}^2$, $L_A(x) = Ax$, $x \in \mathbb{R}^2$. Since T_A is a linear map, $d_x T_A = L_A$. Then
$$d_x T_A \big(E^u(x) \big) = E^u \big(T_A(x) \big)$$
and
$$d_x T_A \big(E^s(x) \big) = E^s \big(T_A(x) \big).$$

We obtain that T_A satisfies (i).

Next, since again $d_x T_A = L_A$, $d_x T_A{}^n = d_x T_{A^n} = L_{A^n}$ for all $n \in \mathbb{Z}$. Then , for $n \in \mathbb{N}$, we have
$$d_x T_A^n(v) = A^n v = \lambda_2^n v \quad \text{for all} \quad v \in E^s(x)$$
and
$$d_x T_A^{-n}(v) = A^{-n}v = \lambda_1^{-n}v = \lambda_2^n v$$
for all $v \in E^u(x)$. This yields that for $n \geq 0$ one has
$$\|d_x T_A^n(v)\| = \lambda_2^n \|v\| \quad \text{for } v \in E^s(x)$$
and
$$\|d_x T_A^{-n}(v)\| = \lambda_2^n \|v\| \quad \text{for } v \in E^u(x).$$

This means that (ii) holds.

$\square$

Remark 2.1. (a) Since $\Omega(f) = \mathbb{T}^2$, $\mathbb{T}^2$ is a hyperbolic set of T_A and hence T_A is hyperbolic by Definition 2.1.

(b) The theorem is still true for any automorhism on $\mathbb{T}^2$ induced by $\begin{bmatrix} a & b \\ c & d \end{bmatrix} \in$ $SL(2, \mathbb{Z})$ with eigenvalues not in the unit circle. Then we call them hyperbolic automorphisms. $\diamond$

Since T_A satisfies the Axiom A, it admits a Markov partition[1]. A Markov partition of T_A is constructed by Katok and Hasselblatt[8] including five rectangles R_0, R_1, R_2, R_3, R_4 (see Figure 2).
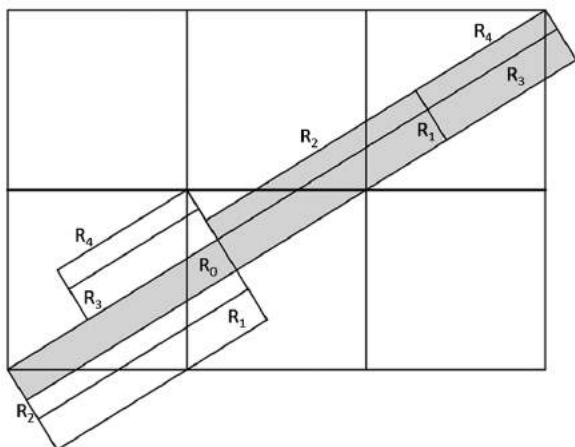
Figure 2. A Markov partion of T_A.

Rectangles R_i are the projections of rectangles in $\mathbb{R}^2$ with edges in directions u_2 and u_1; note that u_1 and u_2 are orthogonal. According to the property of Markov partition, $\cup_{i=0}^4 R_i = \mathbb{T}^2$ and the rectangles intersect only on the boundaries. Furthermore, if $\text{int} T_A(R_i) \cap R_j \neq 0$ then $T_A(R_i)$ intersects R_j along the stable direction, and if $\text{int} T_A^{-1}(R_i) \cap R_j \neq 0$ then $T_A^{-1}(R_i)$ intersects R_j along the unstable direction; see Figure 3.
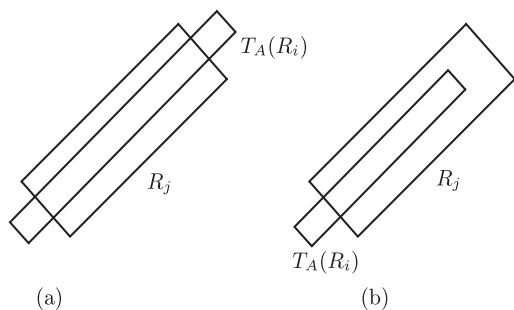

Figure 3. (a) possible, (b) impossible

The adjacency matrix $\mathcal{A} = (a_{i,j})_{i,j=0}^4$ is defined by

$$a_{i,j} = \begin{cases} 1 \text{ if int } T_A(R_i) \cap \text{ int } R_j \neq \emptyset, \\ 0 \text{ if int } T_A(R_i) \cap \text{ int } R_j = \emptyset \end{cases} \quad (1)$$

and explicitly

$$\mathcal{A} = \begin{pmatrix} 1 & 1 & 0 & 1 & 0 \\ 1 & 1 & 0 & 1 & 0 \\ 1 & 1 & 0 & 1 & 0 \\ 0 & 0 & 1 & 0 & 1 \\ 0 & 0 & 1 & 0 & 1 \end{pmatrix}.$$

The definition of a_{ij} in (1) can be explained as follows. If an orbit of T_A passes through $\text{int} R_i$ and then passes through $\text{int} R_j$, then $a_{i,j} = 1$, otherwise $a_{i,j} = 0$.

Denote

$$\mathscr{A} = \{0, 1, 2, 3, 4\}$$

and

$$\mathscr{A}^{\mathbb{Z}} = \{x = (x_i)_{i \in \mathbb{Z}} : x_i \in \mathscr{A} \text{ for all } i \in \mathbb{Z}\}.$$

Definition 2.5. The map $\sigma: \mathscr{A}^{\mathbb{Z}} \longrightarrow \mathscr{A}^{\mathbb{Z}}$ defined by

$$(\sigma x)_i = x_{i+1} \text{ for all } i \in \mathbb{Z}$$

is called the *shift map*.

The distance in $\mathscr{A}^{\mathbb{Z}}$ is given by

$$d(x, y) = \sum_{n=-\infty}^{\infty} 2^{-n}|x_n - y_n|,$$

$x = (x_n)$, $y = (y_n) \in \mathscr{A}^{\mathbb{Z}}$. Then $(\mathscr{A}^{\mathbb{Z}}, d)$ is a compact metric space and σ is a diffeomorphism on $\mathscr{A}^{\mathbb{Z}}$.

Define

$$\Lambda_{\mathcal{A}} = \{(x_n) \in \mathscr{A}^{\mathbb{Z}} : a_{x_i, x_{i+1}} = 1, \forall i \in \mathbb{Z}\}.$$

The symbols can follow 0,1,2 are 0,1,3; and the symbols can follow 3,4 are 2 and 4. Then $\Lambda_{\mathcal{A}}$ is a closed set of $\mathscr{A}^{\mathbb{Z}}$ and invariant under σ, i.e. $\sigma(\Lambda_{\mathcal{A}}) = \Lambda_{\mathcal{A}}$. The map $\sigma_{|\Lambda_{\mathcal{A}}}: \Lambda_{\mathcal{A}} \to \Lambda_{\mathcal{A}}$ is called *subshift of finite type* induced by $\mathcal{A}$.

Definition 2.6. Sequence $x = (x_n)_{n=-\infty}^{\infty} \in \mathscr{A}^{\mathbb{Z}}$ is called periodic of period n if

$$\sigma^n(x) = x,$$

i.e.

$$x_{i+n} = x_i, \forall i \in \mathbb{Z}.$$

Then we write $x = [x_0 x_1 \ldots x_{n-1}]$. The set of all periodic sequences of period n in $\Lambda_{\mathcal{A}}$ is denoted by P_n.

For $n \geq 1$ denote by

$$X_n = \{x_0 \ldots x_{n-1} : x_0, \ldots, x_{n-1} \in \mathscr{A},$$
$$a_{x_i, x_{i+1}} = 1, i \in \{0, \ldots, n-2\}\}$$

the set of all subsequences of n symbols in $\Lambda_{\mathcal{A}}$. For $n = 2$, we have $X_2 = \{00, 01, 03, 10, 11, 13, 20, 21, 23, 32, 34, 42, 44\}$.

Next we find the number of P_n and X_n via $\mathcal{A}^n$. One has

$$\mathcal{A} = P\mathrm{diag}(\lambda_1, \lambda_2, 0, 0, 0)P^{-1}$$

with

$$P = \begin{pmatrix} \frac{1-\sqrt{5}}{2} & \frac{1+\sqrt{5}}{2} & -1 & -1 & 0 \\ \frac{1-\sqrt{5}}{2} & \frac{1+\sqrt{5}}{2} & 1 & 0 & 0 \\ \frac{1-\sqrt{5}}{2} & \frac{1+\sqrt{5}}{2} & 0 & 0 & -1 \\ 1 & 1 & 0 & 1 & 0 \\ 1 & 1 & 0 & 0 & 1 \end{pmatrix}.$$

Then

$$\mathrm{tr}(\mathcal{A}^n) = \lambda_1^n + \lambda_2^n$$

and

$$\mathcal{A}^n = \begin{pmatrix} a_n & a_n & b_n & a_n & b_n \\ a_n & a_n & b_n & a_n & b_n \\ a_n & a_n & b_n & a_n & b_n \\ b_n & b_n & c_n & b_n & c_n \\ b_n & b_n & c_n & b_n & c_n \end{pmatrix},$$

where

$$a_n = \frac{5+\sqrt{5}}{10}\lambda_1^n + \frac{5-\sqrt{5}}{10}\lambda_2^n,$$

$$b_n = -\frac{5+3\sqrt{5}}{10}\lambda_1^n + \frac{-5+3\sqrt{5}}{10}\lambda_2^n,$$

$$c_n = \frac{5+2\sqrt{5}}{5}\lambda_1^n + \frac{5-2\sqrt{5}}{5}\lambda_2^n.$$

Proposition 2.3. (a) The number of subsequences of length n in $\Lambda_{\mathcal{A}}$ is

$$\mathrm{card}(X_n) = \frac{25-11\sqrt{5}}{10}\lambda_1^{n-1} + \frac{25+11\sqrt{5}}{10}\lambda_2^{n-1}.$$

(b) The number of P_n is

$$\mathrm{card}(P_n) = \mathrm{card}\{x \in \Lambda_{\mathcal{A}} : \sigma^n(x) = x\} = \lambda_1^n + \lambda_2^n.$$

Proof. We use Proposition 2.2.12².

(a) The number of subsequences of length n in $\Lambda_{\mathcal{A}}$ is the sum of all entries in matrix $\mathcal{A}^{n-1}$, namely

$$9a_{n-1} + 12b_{n-1} + 4c_{n-1}$$
$$= \frac{25-11\sqrt{5}}{10}\lambda_1^{n-1} + \frac{25+11\sqrt{5}}{10}\lambda_2^{n-1}.$$

(b) The number of n-periodic sequences in $\Lambda_{\mathcal{A}}$ is equal to $\mathrm{tr}(\mathcal{A}^n)$, that is $\lambda_1^n + \lambda_2^n$. $\qquad\square$

For $x = (x_n)_{n \in \mathbb{Z}} \in \Lambda_{\mathcal{A}}$. Using the property of Markov partition, we can show that

$$\bigcap_{n \in \mathbb{Z}} T_A^{-n} R_{x_n}$$

is a single point in $\mathbb{T}^2$ [5]. We define

$$h : \Lambda_{\mathcal{A}} \to \mathbb{T}^2, \ h(x) = \bigcap_{n \in \mathbb{Z}} T_A^{-n} R_{x_n}. \quad (2)$$

Then h is a continuous surjection and satisfies

$$h \circ \sigma = T_A \circ h. \quad (3)$$

Then

$$h \circ \sigma^n = T_A^n \circ h, \text{ for all } n \geq 1. \quad (4)$$

Note that h is not injective, but finite to one. This does not influence the study of periodic orbits. The number of n-periodic points of T_A is given by the following result.

Proposition 2.4. [7] The number of n-periodic points of T_A is

$$\mathrm{card}\{\mathsf{x} \in \mathbb{T}^2 : T_A^n(\mathsf{x}) = \mathsf{x}\} = \lambda_1^n + \lambda_2^n - 2.$$

Remark 2.2. (a) For $x = (x_i) \in P_n, h(x) = \mathsf{x} \in \mathbb{T}^2$ satisfies $T_A^n(\mathsf{x}) = \mathsf{x}$ and

$$T_A^k(\mathsf{x}) \in R_{x_k}, k = 0, \ldots, n-1.$$

(b) If follows from (4) that if $x \in \Lambda_A$ is an n-periodic point of σ then $h(x)$ is an n-periodic point of T_A. Therefore,

$$h : P_n \backslash \{[0], [1], [4]\} \to \{\mathsf{x} \in \mathbb{T}^2 : T_A{}^n(\mathsf{x}) = \mathsf{x}\} \backslash \{0 + \mathbb{Z}^2\}$$

is a bijection. Hence, instead of studying periodic points of T_A, we consider periodic sequences of $\Lambda_\mathcal{A}$. ◇

3. CLUSTERING OF PERIODIC ORBITS

To define clustering of periodic orbits, we need some following notions.

For $\mathsf{x} \in \mathbb{T}^2$ is an n-periodic point of $\mathsf{T_A}$. The orbit of $\mathsf{T_A}$ through x is defined by

$$\mathcal{O}(\mathsf{x}) = \{T_A^i(\mathsf{x}), i = 0, 1, \ldots, n-1\}.$$

Definition 3.1. Let x and y be n-periodic points of $\mathsf{T_A}$ and $p \in \mathbb{N}^*$. We say that $\mathcal{O}(\mathsf{x})$ and $\mathcal{O}(\mathsf{y})$ are p-*close* if there exists a permutation $\alpha : \{0, 1 \ldots, n-1\} \to \{0, 1 \ldots, n-1\}$ such that $d(T_A^k(\mathsf{x}), T_A^{\alpha(k)}(\mathsf{y})) < 2^{-p}, \forall k = 0, \ldots, n-1.$

Roughly speaking, for any point in the orbit of x we can find a point in the orbit of y such that the distance between them is less than 2^{-p}. This means that the two orbits enter the same parts of $\mathbb{T}^2$ but with different orders. We say that these two orbits are in the same p-cluster.

Next we define an equivalence relation $\sim$ in P_n as follows. We say $x \sim x'$ if there is $k \in \{0, \ldots, n-1\}$ such that $\sigma^k(x) = x'$, i.e. x and x' are different up to a shift map. Denote $\mathcal{P}_n = P_n / \sim$. To simplify, we also write $x = [x_0 x_1 \ldots x_{n-1}] \in \mathcal{P}_n$.

Definition 3.2. Let $1 \leq p \leq n$. Two periodic sequences $x = [x_0 \ldots x_{n-1}], y = [y_0 \ldots y_{n-1}] \in \mathcal{P}_n$ are called p-*close* if any subsequence of p consecutive symbols $a_1 a_2 \ldots a_p \in X_p$ appears the same number of times in both x and y.

We write $x \overset{p}{\sim} y$ if x and y are p-close. It is obvious that $\overset{p}{\sim}$ is an equivalence relation.

Proposition 3.1. [3] If $x \overset{p+1}{\sim} y$ then $x \overset{p}{\sim} y$.

Since $\overset{p}{\sim}$ is an equivalence relation on $\mathcal{P}_n$, the set $\mathcal{P}_n$ is decomposed into disjoint equivalence classes $\mathcal{C}_1^{(p)}, \ldots, \mathcal{C}_{\mathcal{N}_p}^{(p)}$. Each equivalence class consists of p-close sequences and is called a p-cluster.

Example 3.1. We consider $n = 7$.

(a) For p = 1, five sequences [0000132], [0000321], [0001032], [0003201], [0010032] belong to the same cluster since the number of times $0, 1, 2, 3, 4$ appear in these sequences are $4, 1, 1, 1, 0$, respectively. This cluster is separated into three 2-clusters: [0000132] and [0000321] are independent clusters, and three sequences [0001032], [0003201], [0010032] belong to one cluster since 00 appears twice in the three sequences, 01, 10, 03, 32, 20 all appear once in the three sequences, while 34, 43, 44, 21, 23 do not appear. When $p = 3$, this third cluster is divided into three 3-clusters, each cluster contains only one sequence; see Figure 4 (b).

(b) For p = 1, six sequences [0011342], [0013421], [0101342], [0103421], [0110342], [0034211] are in the same cluster. For $p = 2$, they form six single 2-clusters; see Figure 4 (a).

Remark 3.1. (a) From Proposition 3.1, the periodic sequences in $\mathcal{P}_n$ can be represented as a line chart as in Figure 2[3]. For $p = 3$, only two clusters have more than one element, including the cluster [0001011], [0100011] and cluster [0010111], [0011101]. ◇
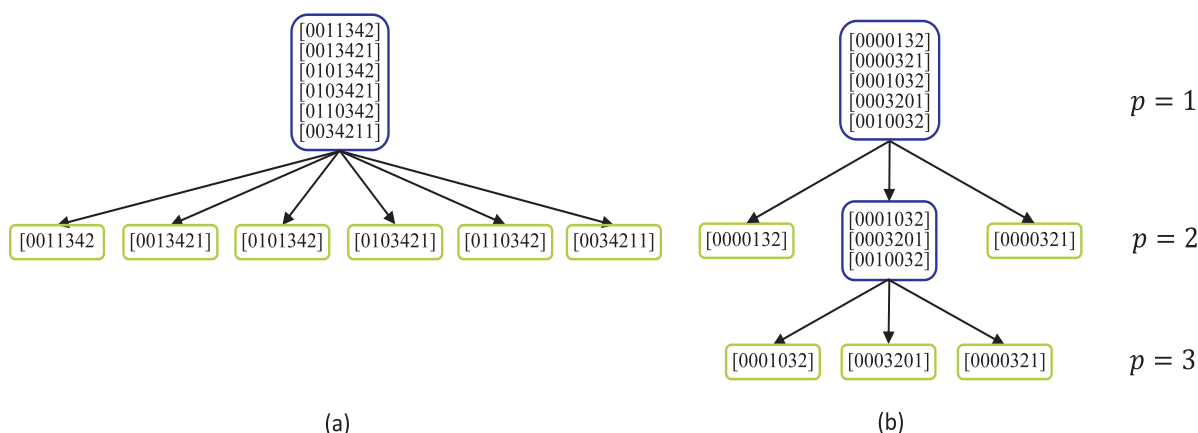
$p = 1$

$p = 2$

$p = 3$

(a)   (b)

Figure 4. Some clusters with $n = 7$

According to Remark 2.2, each n-periodic sequence in $x \in \Lambda_{\mathscr{A}}$ corresponds to an n-periodic point of T_A by the map h defined in (2). Hence, each element x in $\mathcal{P}_n$ corresponds to the n-periodic orbit $\mathcal{O}(h(x))$ of T_A. The next result allows us to consider clusters of periodic sequences in $\mathcal{P}_n$ instead of working on clusters of periodic orbits of T_A.

Proposition 3.2. [3] *If x, $y \in \mathcal{P}_n$ are 2p-close in $\mathscr{A}^{\mathbb{Z}}$ then two orbits $\mathcal{O}(h(x))$, $\mathcal{O}(h(y))$ of T_A are p-close in $\mathbb{T}^2$.*

The problem of counting clusters of periodic orbits is equivalent to the one of counting classes of closed paths in the de Bruijn graph G_p.

Definition 3.3. The *de Bruijn graph* G_p is defined by:

- each vertex corresponds to a sequence $x_0 x_1 \ldots x_{p-2} \in X_{p-1}$;

- each directed edge connecting vertex $x_0 x_1 \ldots x_{p-2}$ to vertex $x_1 x_2 \ldots x_{p-1}$ corresponds $x_0 x_1 \ldots x_{p-1} \in X_p$.

We see that the the set of vertices and the set of edges of de Bruijn graph G_p are X_{p-1} and X_p, respectively. The edges of G_p are the vertices of G_{p+1}. For instance, graph G_p has

vertices $0, 1, 2, 3, 4$ and edges 00, 01, 03, 10, 11, 13, 20, 21, 23, 32, 34, 42, 44; see Figure 5 (a), while edges of G_2 are vertices of G_3, which has 34 edges; see Figure 5 (b).

Each closed path in G_p visiting n edges is represented by a sequence $x = x_0 x_1 \ldots x_{n-1}$ in X_n. This finite sequence induces periodic orbit $[x_0 x_1 \ldots x_{n-1}] \in \mathcal{P}_n$. In this way, the ith edge of G_p corresponds to the code $x_i x_{i+1} \ldots x_{i+p-1}$ of x. Denote by g_x the corresponding closed path in G_p represented by x.

Next we calculate the number of 2-cluster, i.e. the number of equivalence classes of $\overset{2}{\sim}$ in $\mathcal{P}_n$.

Theorem 3.1. The number of 2-clusters in $\mathcal{P}_n$ is the number of vectors $N = (n_a)_{a \in X_2}$ satisfying

$$\sum_{a \in X_2} n_a = n \qquad (5)$$

and

$$S_2 N = R_2^T N, \qquad (6)$$

where S_2 and N_2 are given by

$$R_2^T = \begin{pmatrix} 1 & 1 & 1 & 0 & 0 & 0 & 0 & 0 & 0 & 0 & 0 & 0 & 0 \\ 0 & 0 & 0 & 1 & 1 & 1 & 0 & 0 & 0 & 0 & 0 & 0 & 0 \\ 0 & 0 & 0 & 0 & 0 & 0 & 1 & 1 & 0 & 0 & 0 & 0 & 0 \\ 0 & 0 & 0 & 0 & 0 & 0 & 0 & 0 & 1 & 1 & 1 & 0 & 0 \\ 0 & 0 & 0 & 0 & 0 & 0 & 0 & 0 & 0 & 0 & 0 & 1 & 1 \end{pmatrix}$$
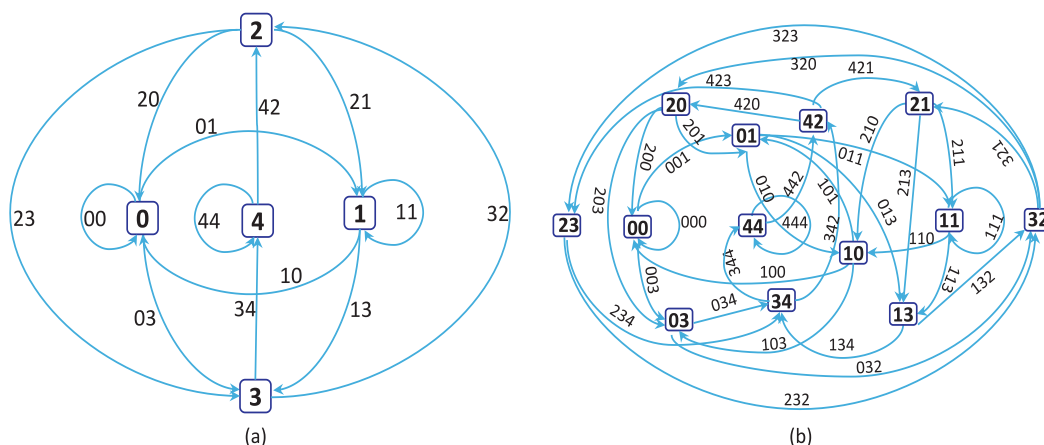
Figure 5. Edges of G_2 (a) are vertices of G_3 (b)

and

$$S_2 = \begin{pmatrix} 1 & 0 & 0 & 1 & 0 & 0 & 0 & 0 & 1 & 0 & 0 & 0 & 0 \\ 0 & 1 & 0 & 0 & 1 & 0 & 0 & 0 & 0 & 1 & 0 & 0 & 0 \\ 0 & 0 & 1 & 0 & 0 & 1 & 0 & 0 & 0 & 0 & 1 & 0 & 0 \\ 0 & 0 & 0 & 0 & 0 & 0 & 1 & 0 & 0 & 0 & 0 & 1 & 0 \\ 0 & 0 & 0 & 0 & 0 & 0 & 0 & 1 & 0 & 0 & 0 & 0 & 1 \end{pmatrix}.$$

Proof. For p ≥ 2. Denote by $N = (n_a)_{a \in X_p}$ the vector in which n_a is the number of times the closed path g_x according to $x \in \mathcal{P}_n$ passes through the edge $a \in X_p$. Then, two sequences x, $y \in X_n$ are p-close (i.e. $x \overset{p}{\sim} y$) if and only if two respective paths g_x, g_y in G_p visit each edge of G_p the same number of times, i.e. $N(x) = N(y)$. Therefore, each equivalence class of p-close sequences is uniquely determined by vector $N = (n_a)_{a \in X_p}$. Each equivalence class in $\mathcal{P}_n/\overset{p}{\sim}$ is identified with a vector $N = (n_a)_{a \in X_p}$, where n_a is the number of times the corresponding path visits the edge a of graph G_p. For $p = 2$, since vector N corresponds to a periodic orbit of period n, its coordinates must satisfy:

(i) the length of closed path is equal to n, so (5) holds;

(ii) the number of times a periodic orbit visits a vertex of G_2 is equal to the number of times this orbit exits that vertex. This is illustrated by equation (6). The theorem is proved. □

Example 3.2. The number of 2-clusters in P_7 is represented by vector $N = (n_{00}, n_{01}, n_{03}, n_{10}, n_{11}, n_{13}, n_{20}, n_{21}, n_{23}, n_{42}, n_{44})$ satisfying the following system

$$\begin{cases} n_{00} + n_{01} + n_{03} + n_{10} + n_{11} + n_{13} + n_{32} \\ \quad + n_{34} + n_{20} + n_{21} + n_{23} + n_{42} + n_{44} = 7 \\ n_{01} + n_{03} - n_{10} - n_{20} = 0 \\ -n_{01} + n_{10} + n_{13} - n_{21} = 0 \\ n_{03} + n_{13} + n_{23} - n_{32} - n_{34} = 0 \\ n_{20} + n_{21} + n_{23} - n_{32} - n_{42} = 0 \\ n_{34} - n_{42} = 0. \end{cases}$$

By solving this system to find non-negative integer solutions, one has 94 solutions, corresponding to 94 2-clusters. There are 76 clusters including single element, 14 clusters including two elements and four clusters including three elements. The 2-clusters with three elements are

$$\{[0001011], [0010011], [0001101]\},$$

$$\{[0010111], [0011011], [0011101]\},$$

$$\{[0001032], [0003201], [0010032]\},$$

$$\{[0111321], [0113211], [0132111]\}.$$

4. CONCLUSION AND OUTLOOK

The paper studies clustering of periodic orbits of the automorphism T_A via symbolic dynamics. We only consider the case $p = 2$, although the de Brujin graph is defined for $p \geq 2$. Furthermore, Theorem 3.1 gives us the information of the number of clusters. The number of elements in the same cluster has not been given. The matrices S_p and R_p for general p as well as algorithms to list all p-clusters will be investigated in the near future.

REFERENCES

1. R. Bowen. Markov partitions for Axiom A diffeomorphisms, *Amer. J. Math.,* **1970**, *95*(3), 725-747.

2. D. Lind, B. Marcus. *An introduction to symbolic dynamics and coding,* Cambridge University Press, 1995.

3. B. Gutkin, V.A. Osipov. Clustering of periodic orbits in chaotic systems, *Nonlinearity,* **2013**, *26,* 177-200.

4. S. Smale. Differential dynamical systems, Bull. *Amer. Math. Soc.,* **1967**, *73,* 747-817.

5. L. Barreira. *Ergodic theory, Hyperbolic dynamics and dimension theory,* Springer Verlag Berlin - Heidelberg, 2012.

6. V. Anorld, A. Avez. *Ergodic problems in classical mechanics*, W.A. Benjamin, Inc., New York-Amsterdam, 1968.

7. M. Pollicott, M. Yuri. *Dynamical systems and ergodic theory*, Cambridge University Press, 1998.

8. A. Katok, B. Hasselblatt. *Introduction to modern theory of dynamical systems,* Cambridge University Press, 1995.

Thành lập lưới khống chế trắc địa
khu vực Trường Đại học Quy Nhơn

Trương Quang Hiển[1,*], Ngô Anh Tú[1], Cù Thị Hiên[2]

[1]Khoa Khoa học Tự nhiên, Trường Đại học Quy Nhơn, Việt Nam
[2]Khoa Kinh tế - Nông lâm, Trường Cao đẳng Cộng đồng Kon Tum, Việt Nam

TÓM TẮT

Lưới khống chế trắc địa khu vực Trường Đại học Quy Nhơn (ĐHQN) được thành lập bằng công nghệ GNSS và công nghệ toàn đạc điện tử, kết hợp với phương pháp đo cao hình học từ giữa, mốc lưới được xây dựng bằng bê tông vững chắc, có nắp sứ định tâm. Lưới gồm 11 điểm, trong đó có 2 điểm được dẫn chuyển từ điểm địa chính cấp I, dùng làm các điểm khởi tính cho đường chuyền. Lưới được xây dựng theo phương pháp toàn đạc với 2 lượt đo đi và đo về; độ cao thủy chuẩn của lưới được đo đạc theo phương pháp đo cao hình học từ giữa, đảm bảo theo đúng quy trình, quy phạm của Bộ Tài nguyên và Môi trường. Kết quả nghiên cứu gồm hệ thống các điểm lưới ổn định vững chắc, kèm theo tọa độ và độ cao thủy chuẩn được bình sai chặt chẽ bằng các phần mềm chuyên ngành, sơ đồ lưới khống chế. Lưới khống chế trắc địa khu vực trường ĐHQN có ý nghĩa quan trọng trong việc thành lập bản đồ, bình đồ, quy hoạch, xây dựng và phục vụ công tác giảng dạy, nghiên cứu khoa học của trường.

Từ khóa: *Lưới khống chế, tọa độ, trắc địa, bản đồ, bình sai.*

Tác giả liên hệ chính.
Email: truongquanghien@qnu.edu.vn

Establishment of geodetic control network for Quy Nhon University area

Truong Quang Hien[1,*], Ngo Anh Tu[1], Cu Thi Hien[2]

[1]Faculty of Natural Sciences, Quy Nhon University, Vietnam
[2]Faculty of Economics - Agricultural and Forestry, Kon Tum Community College, Vietnam

ABSTRACT

Geodetic control network of Quy Nhon University (QNU) is established based on GNSS technology and electronic total station technology in combination with the middle geometrical elevation surveying method, bench mark of network built with firm concrete installed with a centralized insulator cap. The network consists of 11 points, of which 2 points are traversed from the cadastral point of class I, used as the starting points for the traverse. The network is built based on total station method with 2 turns of forward and backward surveying. The network's leveling height is measured by the middle geometrical elevation surveying method, ensuring compliance with the procedures and rules of the Ministry of Natural Resources and Environment. The research result includes a system of stable and solid network points together with the coordinates and the leveling height that are closely adjusted by specialized software, control network diagram. Geodetic control network of the QNU is important in setting up map, general plan, planning, construction and serving for teaching and scientific research of the university.

Keywords: *Control network, coordinates, surveying, map, adjustment.*

1. INTRODUCTION

Geodetic control network plays an important role in setting up map, general plan, planning, and construction, etc. In teaching and scientific research, geodetic control network plays an important role in facilitating students in practicing the surveying, data processing, building cadastral map and topographic surveying. Quy Nhon University (QNU) offers a number of majors such as Land Management, Natural Resources and Environment Management and Construction. However, in the university campus, there is currently no fixed geodetic control network system with the coordinates and leveling height of the points, so it is very difficult for the process of teaching subjects related to geodesy, and it is

quite hard for lecturers to check the result after students practice the surveying. Therefore, the construction of a fixed geodetic control network for Quy Nhon University is a necessary and meaningful job.

The research result includes a system of stable and solid network points together with the coordinates and the leveling height closely adjusted by specialized software, control network diagram. This will be an important document not only for teaching and scientific research but also it is an important source of data with high accuracy for the planning and construction of works in the campus of Quy Nhon University.

2. RESEARCH METHODS

The article uses the following research methods:

---

*Corresponding author.
Email: truongquanghien@qnu.edu.vn

- *Investigation and collection of data and documents* to investigate, and collect necessary data and information for the research such as cadastral map, high-level coordinating elevation points, conditions of surveying area, etc.

- *Surveying:* Use GNSS surveying method (static and dynamic surveying), total stastion method, middle geometrical elevation surveying method to establish the geodetic control network for Quy Nhon University. The given result is the unrefined result, which is the basis for data processing to give the result as coordinates and elevation with 11 network points.

Static surveying method uses 2 national coordinates to pass the coordinates and elevation to 2 cadastral points built for Quy Nhon University, namely DHQN and DHQN-A5, the surveying time for each station is 60 minutes. Each surveying turn consists of 3 points forming a triangular network, meeting the regulations on cadastral network surveying of the Ministry of Natural Resources and Environment.

The coordinates and elevation traverse survey from the cadastral points QNU-A5 for 2 points QNU.01 and QNU.02 uses the method of dynamic surveying, real-time RTK, using clamps to ensure accuracy for surveying results.

Total station method is used to determine the angles and edges of the traverse. The survey at each surveying station consists of 2 turns of forward and backward survey with 2 halves of a surveying turn, taking the average of the survey result will give value for adjustment.

Geometrical elevation surveying method is used to determine the elevation between two surveying points. Level gauge is placed between two surveying stations with relatively equal distance, minimizing errors caused by surveying instruments and external conditions.

- *Data processing:* Used in processing surveyed data in field and assessing error of surveying result. For data processing, specialized software such as TBC, PRONET, DPSurvey will be used to adjust surveying results, give final data and evaluate the error level of such results.[1]

- *Mapping:* Used to edit geodetic control network diagram under the specified specifications and scale. Network diagram will be edited on Microstation SE software at 1: 500 scale, for later detailed surveying.[1,2]

- *Field:* After surveying, data processing and edition of the network diagram, the field check will be conducted so that the study can be adjusted accurately and in accordance with the reality.

3. RESEARCH RESULT

3.1. Design of geodetic control network for Quy Nhon University

Quy Nhon University is located in Nguyen Van Cu ward, Quy Nhon city, Binh Dinh province. The university has a quite beautiful location and a wide campus close to Quy Nhon beach with an area of more than 14 hectares, with its East borders the East Sea, its West borders Nguyen Thi Dinh Street, its South borders Quy Nhon College of Engineering and Technology, its North borders the residential area. The topography of the university is relatively flat, which is a favorable condition for the design and surveying process of geodetic control network.

3.1.1. Investigation and collection of documents and data

In order to serve the surveying of the geodetic control network of Quy Nhon University, an investigation of the surveying area is conducted to assess the advantages and disadvantages of the topography and geophysics for the surveying process. In general, the topography is not too complicated, so the arrangement of the network is not quite difficult.

Through the investigation, collection of documents and data, there are 2 high-level points, belonging to the National coordinate network with numbers 875408 and 875413, which is the basis for passing the coordinates and the elevation to the geodetic control points built within the campus of Quy Nhon University.

Table 1. National coordinate points

Ordinal	Point Symbol	Coordinate		Elevation	Point position
		X (m)	Y (m)	H (m)	
1	875408	1524516.834	603058.892	127.943	Ba Hoa Mountain
2	875413	1518732.226	603855.356	98.386	Qui Hoa Slope pass

(*Source: Department of Natural Resources and Environment of Binh Dinh Province*)

3.1.2. Control point passing

The surveying and passing for two control points of Quy Nhon University are conducted based on the GNSS network establishment standard of the Ministry of Natural Resources and Environment. The surveying and passing of the coordinates and the elevation are conducted for 2 points to be the control points, namely QNU and QNU-A5. These two control points are traversed in May 2016.

Prior to the survey, it is required to conduct scheduling for the surveying area with the minimum simultaneous surveying time on a point of surveying station. The GNSS receiver used for the surveying of traverse points is two-frequency Trimble R4. The survey is carried out under the static survey method with 3 receivers. Each surveying turn satisfies the following conditions:

+ Minimum simultaneous surveying time: 60 minutes

+ Minimum number of continuous strong satellites: 4 satellites

+ PDOP selects when maximum surveying value does not exceed 4.0

+ Threshold of satellite elevation angle is larger than: 15º

Surveying result is saved in each receiver, then transferred to a computer by each file to serve for the adjustment.[3,4]

❖ *Adjustment of traverse points*

The traverse points for Quy Nhon University are processed and calculated by the software Trimble Business Center (TBC), which is allowed by the Ministry of Natural Resources and Environment to be used to adjust the GNSS surveying result, achievement of coordinates and elevation calculation under VN-2000 coordinate system, projection 3^0, $108^0\,15'$ meridian.[1]

Calculation result is shown in table 2 as follows:

Table 2. Summary of surveying accuracy evaluation results

1. Unit weighted square error:	$M_0 = 1.000$		
2. Point position error:			
☐ Minimum:	$mp_{min} =$	0.008m	(Point: DHQN-A5)
☐ Maximum:	$mp_{max} =$	0.008m	(Point: DHQN-A5)
3. Edge relative error:			
☐ Minimum:	$ms/s_{min} =$	1/560305	(Edge: 875413_DHQN, S = 3226.9m)
☐ Maximum:	$ms/s_{max} =$	1/118902	(Edge: DHQN_DHQN-A5, S = 272.8m)
4. Azimuth error:			
☐ Minimum:	$ma_{min} =$	0.41"	(875408_DHQN)
☐ Maximum:	$ma_{max} =$	1.48"	(DHQN_DHQN-A5)
5. Elevation difference error:			
☐ Minimum:	$mdh_{min} =$	0.006m	(DHQN_DHQN-A5)
☐ Maximum:	$mdh_{max} =$	0.021m	(875413_DHQN-A5)
6. Edge length:			
☐ Minimum:	$S_{min} =$	272.800m	(DHQN_DHQN-A5)
☐ Maximum:	$S_{max} =$	3226.906m	(875413_DHQN)
☐ Medium:	$S_{tb} =$	3081.044m	

After calculation and preliminary evaluation of the surveying result as above, we continue to evaluate the accuracy of the traverse points. Evaluation result is shown in the table 3:

Table 3. Evaluation of the result of adjusting traverse points

Ordinal	The technical indicators	Allowed limitation of error [1]	Results	Evaluation
1	Point position error after adjusted	≤ 5 cm	0,8 cm	Satisfy
2	Edge relative error after adjusted	≤ 1/50000	1/118902	Satisfy
3	Azimuth error after adjusted	≤ 5"	1.48"	Satisfy
4	Elevation difference error after adjusted	≤ 10 cm	2,1 cm	Satisfy

Table 3 shows the result of general evaluation of the established traverse points that shows the technical specifications and the allowable limits of each indicator, and then compares with the result of the network after being adjusted and finally judges, evaluates whether to satisfy or not. Under the above evaluation result, the traverse points set up for Quy Nhon University gave surveying result with high accuracy, ensuring the permissible limit. The result of Table 3 also showed the progress of TBC software in the adjustment and accuracy assessment of surveying results.[1,5]

The final result of the elevation control network adjustment is the coordinates and elevation of the traverse points in field. This is an important data for the survey work of Quy Nhon University.

Table 4. Result of calculating flat coordinates and elevation after being adjusted

Ordinal	Point Symbol	Coordinate		Elevation
		X (m)	Y (m)	H (m)
1	875408	1524516.834	603058.892	127.943
2	875413	1518732.226	603855.356	98.386
3	DHQN-A5	1521758.520	604332.399	27.692
4	DHQN	1521877.165	604578.048	22.513

Table 4 summarizes the results of the coordinates and elevation of the control points traversed to Quy Nhon University after detailed adjustment, calculation and accuracy evaluation of the criteria of the network. These are the basic points serving the establishment of the fixed geodetic control network for Quy Nhon University.

3.2. Establishment of geodetic control network for Quy Nhon University

3.2.1. Establishment of coordinate control network for Quy Nhon University

❖ *Arrangement and surveying of theodolite traverse*

Based on the available data in combination with the field investigation, the establishment of geodetic control network for Quy Nhon University is conducted. Firstly, based on the distribution of the existing basic points in combination with topographic conditions to subdivide to establish geodetic control network types. Arrange appropriate control networks depending on the actual topographic conditions of each area, the geodetic control network

established for Quy Nhon University is a network with a closed graph.

The geodetic control network for the entire area of Quy Nhon University includes 11 points, of which 2 points of QNU.01 and QNU.02 subject to traverse coordinates and elevation surveying by GNSS technology from QNU-A5 point are used as the starting points for the traverse types. The coordinate network is surveyed under total station method with

2 turns of forward and backward surveying, with 2 halves of a surveying turn, ensuring the process and rules as specfied by the Ministry of Natural Resources and Environment of Vietnam. In addition, in order to determine the elevation of the control points, the middle geometrical elevation surveying is carried out, the surveying result is closely adjusted, ensuring accuracy as regulated by the Ministry of Natural Resources and Environment.[1,6]

Table 5. Coordinates and elevation of the traverse points as the starting point

Ordinal	Point Symbol	Coordinate		Elevation
		X (m)	Y (m)	H (m)
1	QNU.01	1521725.116	604460.212	5.812
2	QNU.02	1521708.434	604535.057	6.135

❖ *Control network surveying*

The coordinate control network of the entire area of Quy Nhon University includes 11 points, of which 2 original points that have the coordinates traversed are used as starting points for the traverse network. The network is built under total station method with 2 turns of forward and backward survey with 2 halves of a surveying turn, ensuring compliance with the process and rules of the Ministry of Natural Resources and Environment.[1,8]

After the control points in the traverse are designed, we use TOPCON-GTS 230N electronic total station to survey the traverse under total station method. A traverse twice, forward and backward survey with 4 halves of a bidirectional surveying turn. The surveying result is averaged and adjusted by ProNet software, the adjustment result in the data sheet is attached with accuracy evaluation sheet of the surveying result.[7] Surveying result is shown in Table 6.

Table 6. Result of coordinate control network survey of Quy Nhon University

Measuring station	Point	horizontal angle reading		2C (<15")	Horizontal angle	Distance (m)		Average distance
		Right	Left			Right	Left	
QNU.01	QNU.10	00 00 00	180 00 00	0	201 15 20	64.639	64.640	64.639
	QNU.02	201 15 19	30 15 21	2		73.541	73.541	73.541
QNU.02	QNU.01	00 00 00	180 00 05	5	78 25 19	73.540	73.541	
	QNU.03	78 25 21	258 25 22	1		97.242	97.241	97.242
QNU.03	QNU.02	00 00 00	179 59 55	5	106 32 22	97.241	97.242	
	QNU.04	106 32 24	286 32 29	5		94.291	94.291	94.291
QNU.04	QNU.03	00 00 00	180 00 00	0	268 40 35	94.291	94.292	
	QNU.05	268 40 32	88 40 38	5		86.170	86.171	86.170
QNU.05	QNU.04	00 00 00	180 00 06	6	205 15 46	86.169	86.171	

Measuring station	Point	horizontal angle reading		2C (<15")	Horizontal angle	Distance (m)		Average distance
		Right	Left			Right	Left	
QNU.06	QNU.06	205 15 44	25 15 52	8	35 20 18	77.143	77.143	77.143
	QNU.05	00 00 00	180 00 04	4		77.142	77.143	
	QNU.07	35 20 19	215 20 21	3		134.791	134.792	134.791
QNU.07	QNU.06	00 00 00	180 00 00	0	105 34 47	134.791	134.791	
	QNU.08	105 34 49	285 34 45	4		135.412	135.412	135.412
QNU.08	QNU.07	00 00 00	180 00 05	5	196 35 19	135.412	135.411	
	QNU.09	196 35 20	16 35 23	3		126.703	126.703	126.703
QNU.09	QNU.08	00 00 00	180 00 00	0	83 24 45	126.703	126.702	
	DC-II.2	83 24 44	263 24 46	2		90.589	90.588	90.589
DC-II.2	QNU.09	00 00 00	180 00 03	3	257 41 49	90.590	90.589	
	QNU.10	257 41 48	77 41 53	5		33.418	33.417	33.418
QNU.10	DC-II.2	00 00 00	180 00 04	4	81 13 25	33.418	33.418	
	QNU.01	81 13 26	261 13 28	2		64.640	64.639	64.639

❖ *Calculation of the traverse network adjustment*

After finishing coordinate control network surveying of Quy Nhon University and obtaining specific data on aspects in the network, we use Pronet software to conduct the summary as well as detailed adjustment of the surveying control network.

```
        THEODOLITE TRAVERSE CHECK
        ============***===========
1.Route:  QNU.01_QNU.02_QNU.03_QNU.04_QNU.05_QNU.06_QNU.07_QNU.08_
          QNU.09_DC-II.2_QNU.10_QNU.01_QNU.02
          Route length      [S] = 1013.939 (m)        N =  11
          Azimuth closure   Wb = -15"                 W(g/h) =  63.25"
          coordinate closure  fx = -0.007 (m)         fy    = -0.006 (m)
                              fp = 0.009 (m)           fs/[S] = 1/5400
          -------------------------------------------------------------
             Angular error (Ferero)    Mb =    1.364"
             Edge error                Ms =    1.041 (cm)
             average edge length       S(tb)=   92.176 (m)
          -------------------------------------------------------------
```

Figure 1. Result of control network summary

The entire coordinate control network of Quy Nhon University includes 11 control points, including 2 known points and 9 surveying points. The network has a closed traverse shape. The result of evaluating the result of the coordinate control network summary of Quy Nhon University are synthesized in Table 7:

Table 7. Evaluation of the result of coordinate control network summary

Ordinal	The technical indicators	Allowed limitation of error [1]	Results	Evaluation
1	Azimuth closure error	$\pm 30" \sqrt{n}$	$\pm 5"$ to $\pm 57"$	Satisfy
2	Coordinates closure error	1/2500	1/5400 – 1/3500	Satisfy

Table 7 showed that the results meet the required technical requirements, the calculation errors were much smaller than the allowed errors in the cadastral mapping regulations of the Ministry of Natural Resources and Environment, therefore the following steps can be adjusted to evaluate in a more detailed manner the errors of the control points in the traverse.[1]

After conducting the adjustment of the coordinate control network of Quy Nhon University on Pronet software, the result is summary tables of data on surveying value, adjustment value, coordinates of points and error types... The result of evaluating technical indicators of the geodetic control network of Quy Nhon University are synthsized in Table 8:

Table 8. Evaluation of the result of coordinate control network adjustment

Ordinal	The technical indicators	Allowed limitation of error	Results	Evaluation
1	Shortest side length	≥ 20 (m)	33.418 (m)	Satisfy
2	Longest side length	≤ 250 (m)	135.412 (m)	Satisfy
3	Mean square error easuring edge after adjustment	0,020 m	$\leq 0,015$ m	Satisfy
4	Minimum angle	$\geq 5°$	35°20'18"	Satisfy

The result of calculating traverse types in the coordinate control network of Quy Nhon University has technical indicators that meet the regulations of the Ministry of Natural Resources and Environment, which can be used to edit the geodetic control network for the area. The adjustment result is shown in Figure 2:

```
        RESULTS OF CALCULATION FOR THE SURVEY NETWORK
             ============****=============
 =================================================================
| Or | POINT  |        COORDINATE         |    LOCATION ERROR     |
| di | SYMBOL |---------------------------|-----------------------|
| nal|        |    X(m)     |     Y(m)    |  Mx  |  My  |  Mp   |
|====|========|=============|=============|======|======|======|
|  1 |QNU.03  | 1521817.346 |  604545.322 |0.008 |0.007 |0.012  |
|  2 |QNU.04  | 1521886.892 |  604481.665 |0.001 |0.009 |0.029  |
|  3 |QNU.05  | 1521956.453 |  604532.532 |0.007 |0.005 |0.014  |
|  4 |QNU.06  | 1521976.775 |  604606.939 |0.006 |0.003 |0.011  |
|  5 |DQN.07  | 1522012.403 |  604476.941 |0.007 |0.001 |0.011  |
|  6 |QNU.08  | 1521895.632 |  604408.385 |0.005 |0.001 |0.013  |
|  7 |QNU.09  | 1521810.974 |  604314.117 |0.005 |0.007 |0.010  |
|  8 |DC-II.2 | 1521764.286 |  604391.749 |0.005 |0.003 |0.012  |
|  9 |QNU.10  | 1521731.615 |  604398.724 |0.009 |0.006 |0.017  |
 =================================================================
```

Figure 2. Result of calculating the surveying control network by Pronet software

From the result of the coordinates of control points, it is possible to edit the surveying control network diagram for the area. The geodetic control network of Quy Nhon University consists of 11 points, the control points are distributed throughout the area, their density satisfies with the detailed surveying.
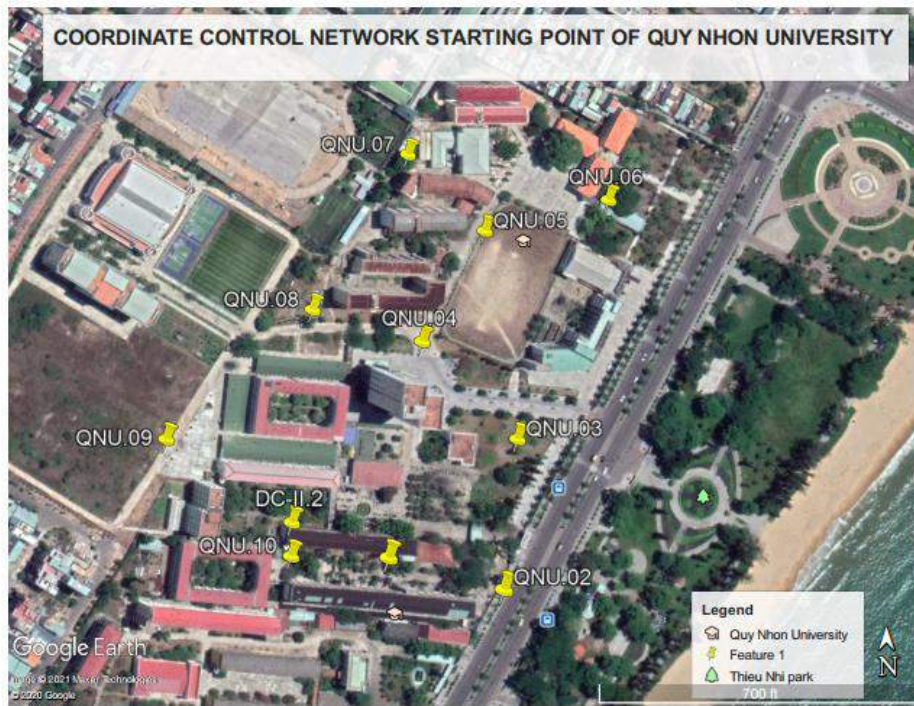
Figure 3. Coordinate control network starting point of Quy Nhon University

3.2.2. Establishment of elevation control network for Quy Nhon University area

❖ *Control network surveying*

Elevation control network for Quy Nhon University area is surveyed based on the established network points of the coordinate control network, thereby forming a fixed coordinate network system for the surveying area. Two datum points that have known elevation are QNU.01 and QNU.02.

The surveying of elevation control network and use of the level gauge to survey the middle geometric elevation for control points are conducted in accordance with the process and regulations. After surveying the elevation many times among the control points, the following result is obtained:

Table 9. Data of surveying of elevation control points

Measurement route	Point behind	Point forward	Distance (m)	Height difference (m)
QNU.01_ QNU.02	QNU.01	QNU.02	73.541	-0.003
QNU.02_ QNU.03	QNU.02	QNU.03	97.242	-0.053
QNU.03_QNU.04	QNU.03	QNU.04	94.291	-0.173
QNU.04_ QNU.05	QNU.04	QNU.05	86.170	1.684
QNU.05_ QNU.06	QNU.05	QNU.06	77.143	-0.934
QNU.06_ QNU.07	QNU.06	QNU.07	134.791	-0.809
QNU.07_ QNU.08	QNU.07	QNU.08	135.412	0.156
QNU.08_ QNU.09	QNU.08	QNU.09	126.703	0.188
QNU.09_ DC-II.2	QNU.09	DC-II.2	90.589	-0.048
DC-II.2_ QNU.10	DC-II.2	QNU.10	33.418	0.037
QNU.10_QNU.01	QNU.10	QNU.01	64.639	-0.045

Table 9 shows the result of field surveying with Pentax AP-281 level gauge with an accuracy of ± 2.0mm, the use of middle geometrical elevation surveying method to ensure high accuracy and in accordance with regulations of the Ministry of Natural Resources and Environment. The determination of the leveling elevation of newly established control points is performed by determining the elevation among the points, starting from the known cadastral point QNU.01. However, the process of determining the elevation among control points is not the same and it's required to arrange suitable surveying methods depending on the topography as well as the distance between the surveying stations. Only one surveying station is required for short surveying stations with favorable terrain while sub-stations are required to ensure accuracy for the stations with complicated topography and a long distance. After surveying in field, the data will be processed to gain the elevation among the established control points (Table 9).

❖ *Calculation of traverse network adjustment*

After collecting the necessary data and conducting field surveying, we use DPSurvey 3.2 software to process data. The result after the adjustment is shown in Table 10:

Table 10. Surveying value and quantities after adjustment

Ordinal	Point behind	Point forward	Measured value	Correction number	Adjustment value	Mean square error
	(i)	(j)	(m)	(mm)	(m)	(mm)
1	QNU.01	QNU.02	-0.003	-1.0	0.323	1.2
2	QNU.02	QNU.03	-0.053	-0.8	-0.453	1.5
3	QNU.03	QNU.04	-0.173	-1.4	0.516	1.5
4	QNU.04	QNU.05	1.684	-1.0	1.541	2.0
5	QNU.05	QNU.06	-0.934	-0.7	-1.326	1.5
6	QNU.06	QNU.07	-0.809	-0.3	-0.463	1.7
7	QNU.07	QNU.08	0.156	-0.2	0.352	1.0
8	QNU.08	QNU.09	0.188	-0.5	0.257	1.2
9	QNU.09	DC-II.2	-0.048	-0.3	0.147	1.1
10	DC-II.2	QNU.10	0.037	-0.3	0.166	1.8
11	QNU.10	QNU.01	-0.045	-0.8	-0.060	1.5

Table 10 shows the corrective number (SHC) of the surveying values and the result of calculating the elevation among the control points after being adjusted. In addition, it also calculates the mean squared error (MSE) of each surveying value. Elevation control network established for Quy Nhon University is an engineering elevation control network, thereby there is an allowed error: $f_{CF} = \pm 50\sqrt{L} = 50.347$ mm. The result of evaluating the accuracy of the result after the elevation control network adjustment shows that unit weighted MSE, MSE of the elevation and height of the weakest point are all very small compared to the allowed error. Thus, the surveying result ensure high accuracy and can be used to conduct the following calculation steps.[1, 9]

After calculating and preliminarily evaluating the surveying result as above, we continue to evaluate the accuracy of the established elevation control network. Evaluation result is shown in Table 11:

Table 11. Evaluation of elevation network adjustment result

Ordinal	The technical indicators	Allowed limitation of error[1]	Results	Evaluation
1	The length of the edge	≤ 150 (m)	135.412 (m)	Satisfy
2	The difference between the machine and the two yards	≤ 5 (m)	4.173 (m)	Satisfy
3	Accumulate the distance difference on the route	≤ 50 (m)	24.532 (m)	Satisfy
4	Beam height compared to the ground	≥ 0.2 (m)	0.212 (m)	Satisfy
5	High margin of error	$\leq \pm 50 \sqrt{L\,(km)}$ $= 50.347$ (mm)	± 10 (mm)	Satisfy

Table 11 shows the result of the general evaluation of the established elevation control network, where technical indicators and allowed limits of each indicator are presented, then compared with the result of the network after adjustment and finally make judgment and evaluation whether to satisfy or not. According to the above evaluation result, the elevation control network established for Quy Nhon University area obtained surveying result with high accuracy, exceeding the permissible norms.

The final result of the elevation control network adjustment is the leveling height of the control points in field, together with the height of points is the mean error of each point.

Table 12. Elevation of point after adjustment

Ordinal	Point symbol	H(m)	Mean square error (mm)
1	QNU.01	5.616	0.0
2	QNU.02	5.613	0.0
3	QNU.03	5.560	1.7
4	QNU.04	5.387	2.1
5	QNU.05	7.071	1.4
6	QNU.06	6.137	1.5
7	QNU.07	5.328	1.2
8	QNU.08	5.484	1.3
9	QNU.09	5.672	1.4
10	DC-II.2	5.624	1.2
11	QNU.10	5.661	1.6

After the coordinates and leveling height of the points are obtained, we edit the geodetic control network for the study area using Microstation SE software, then conduct field check, survey and review in field, adjust the result and produce the map of fixed geodetic control network of Quy Nhon University area with the coordinate system and elevation of points as follows:

Table 13. Summary of coordinates and leveling height of geodetic control points

Ordinal	Point symbol	Coordinate		Elevation
		X	Y	H (m)
1	QNU.01	1521732.075	604463.364	5.616
2	QNU.02	1521720.562	604536.001	5.613
3	QNU.03	1521817.350	604545.326	5.56
4	QNU.04	1521886.895	604481.660	5.387
5	QNU.05	1521956.450	604532.530	7.071
6	QNU.06	1521976.768	604606.942	6.137
7	QNU.07	1522012.407	604476.945	5.328
8	QNU.08	1521895.635	604408.380	5.484
9	QNU.09	1521810.979	604314.112	5.672
10	DC-II.2	1521764.292	604391.743	5.624
11	QNU.10	1521731.610	604398.729	5.661

Figure 4. Diagram of the coordinate control network of Quy Nhon University

4. CONCLUSION

Through the process of researching, we built the fixed survey marks for QNU area with 11 starting points of solid concrete and a centralized insulator cap. These starting points have coordinates traversed by GNSS technology and total station technology in combination with middle geometrical elevation surveying method, then calculated and closely adjusted, ensuring compliance with the regulations of the Ministry of Natural Resources and Environment. The research result established a fixed geodetic network for GNU area with a system of control points having coordinates and leveling height determined exactly in field. The research result also established important documents for teaching and scientific research, and at the same time serving the planning and construction of items and works for Quy Nhon University area.

REFERENCES

1. Ministry of Natural Resources and Environment. Regulation of establishing cadastral map, Decision No. 25/2014/TT-BTNMT 19/5/2014.

2. Truong Quang Hien, Ma Cai Xue, He Li Yuan. Techniques of surveying and Cadastral mapping in Vietnam, *International journal of scientific and research publications,* **2015**, *5*(2), 1-7.

3. Truong Quang Hien, Nguyen Trong Doi, Ngo Thi Quynh. Information technology applications in the establishment of cadastral map method of total station in Phuoc Loc Commune, Tuy Phuoc District Binh Dinh Province, *Journal of science and development 2014, Hanoi agricultural University, Vietnam,* **2014,** *12*(2), 187-196.

4. Truong Quang Hien, Nguyen Huu Xuan, Ngo Anh Tu, Nguyen Trong Doi. GNSS technology applications in geodesic and construction of data system to serve dike management and disaster prevention for Lai Giang river downstream areas, Binh Dinh Province, *Geography 2016 nationwide conference proceedings,* **2016,** 1228-1236.

5. Ministry of Natural Resources and Environment, Circular No. 05/2009/TT-BTNMT, June 1, 2009 about guiding inspection, appraisal and acceptance of works, measurement products and maps.

6. Truong Quang Hien, Luu Thi Ngoc Dieu, Le Ngoc Vu, Nguyen Thi My Liem, Pham Ngoc Quy. Established hight control serving the topographic mapping for Ghenh Rang Resort, Quynhon City, Binhdinh Province, *Journal of science- Can Tho University,* **2014,** *2014*(30a), 115-124.

7. Truong Quang Hien, Tran Van Lanh. Application of GNSS establishing the basic cadastral control network to serve cadastral surveying in Vinh Kim Commune, Vinh Thanh District, Binh Dinh Province, *GIS 2017 Nationwide conference proceedings,* **2017,** 810 – 818.

8. Nguyen The Phuong. Cadastral mapping method by total station. Teaching Resources for Land Administration majors, Natural sciences university, Hanoi, Vietnam, 2011.

9. Truong Quang Hien. The effects of design of mesh control measure of ground to distribution of errorsin geodesic, *Journal of science, Quy Nhon University,* **2013**, *6*(1), 125-138.

Xây dựng và khảo sát sự thay đổi của các thông số lò hồ quang điện dựa trên mô hình bảo toàn năng lượng bằng phần mềm Pscad

Đoàn Đức Tùng, Lương Ngọc Toàn*

Khoa Kỹ thuật & Công nghệ, Trường Đại học Quy Nhơn, Việt Nam

TÓM TẮT

Phân tích thực tế cho thấy dòng điện lò hồ quang có chứa nhiều sóng hài gây ảnh hưởng xấu đến chất lượng điện năng. Có nhiều báo cáo trong và ngoài nước về mô hình hóa và đánh giá ảnh hưởng của EAF đến lưới điện dựa trên các mô hình khác nhau. Tuy nhiên việc lựa chọn công suất của EAF để nghiên cứu và áp dụng các thiết bị cải thiện chất lượng điện năng phù hợp với mức công suất vẫn chưa được đề cập, các mô hình này chủ yếu được xây dựng trên phần mềm Matlab Simulink nên chủ yếu mang tính học thuật. PSCAD là một trong những phần mềm được sử dụng rộng rãi cho việc mô phỏng hệ thống điện và được các công ty lớn sử dụng như ABB, tập đoàn điện lực Hàn Quốc Kepco. Xây dựng mô hình EAF bằng phần mềm PSCAD sẽ làm tăng khả năng áp dụng kết quả mô phỏng vào thực tiễn. Mục tiêu của bài báo đi vào xây dựng mô hình lò hồ quang điện dựa trên mô hình bảo toàn năng lượng bằng phần mềm PSCAD, từ đó đánh giá sự thay đổi của các thông số trong mô hình và ảnh hưởng của phụ tải này đến lưới điện trong quá trình vận hành.

Từ khóa: *Lò hồ quang điện, chất lượng điện năng, mô hình phi tuyến, pscad.*

Tác giả liên hệ chính.
Email: lntoan@ftt.edu.vn

Construction and survey of changes in electric arc furnace parameters based on energy conservation model using Pscad software

Doan Duc Tung, Luong Ngoc Toan[*]

Faculty of Engineering and Technology, Quy Nhon University, Vietnam

ABSTRACT

Actual analysis showed that the arc furnace current contains many harmonics that adversely affect the power quality. There are many domestic and foreign reports on modeling and assessing the impact of EAF on the grid based on different models. However, EAF's selection of capacity for research and application of power quality improvement devices suitable to the power level has not been mentioned. These models mainly built on Matlab Simulink software are primarily academic. PSCAD is one of the widely used software for electrical system simulation and is used by large companies such as ABB, Korean power corporation Kepco. Building EAF model with PSCAD software will increase the ability to apply simulation results into practice. The objective of the paper is to build an electric arc furnace model based on the energy conservation model with PSCAD software, thereby assessing the change of parameters in the model and the effect of this load on electricity grid during operation.

Keywords: *Electric arc furnace, power quality, nonlinear model, pscad.*

1. INTRODUCTION

Electric arc furnaces (EAFs) use the heat to fuse metal produced by an electrical discharge between electrodes or between an electrode and a metallic material to melt. When the electric arc furnace is in operation, the current causing the arc current to constantly change with the molten metal, at the same time due to the operation of the melted material that changes the distance between the electrode and the material, when adjusting the electrodes, blowing oxygen into the furnace also makes the arc currents change rapidly in a wide range and not stable. Electric

arc furnaces also consume the active and reactive power of the grid.

The EAF model is built on the arc characteristic of the furnace, which represents the arc current and voltage value during operation. The actual EAF model data is difficult to obtain because the equipment working environment is arc environment with very large currents. However, precise arc values are really necessary for the design process.

2. ARC CHARACTERISTICS

The nature of the electric arc is radioactive phenomenon with a very large current density.[1]

---

[*]*Corresponding author.*
Email: lntoan@ftt.edu.vn
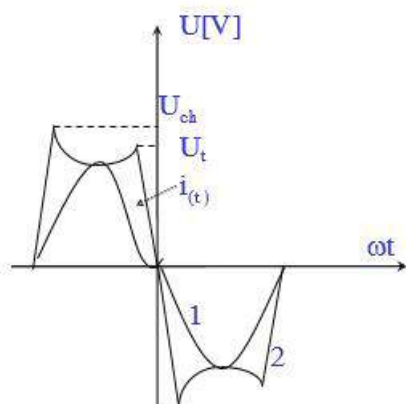
Figure 1. Wave voltage and current of the arc

In alternating electric arcs, the supply current and voltage fluctuate periodically with the grid frequency. Since the arc is a nonlinear resistance, the current and voltage of the arc are in phase. From the actual measurement results shown in Figure 2, the current has a waveform that is almost like a sine wave, and the voltage has two peaks in half a cycle corresponding to the two values of the burn voltage (Uch) and the off voltage (Ut) of the electric arc.[1,2]
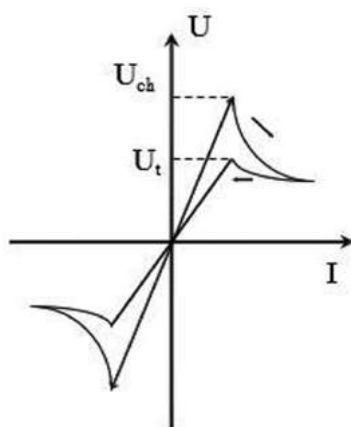
Figure 2. Volt-ampere characteristics of alternating electric tanks.

During the first cycle, the arc voltage increases rapidly to the burn value (according to the supply voltage). When the arc burns, the voltage gradually decreases. The current increases from 0 to the point of fire, the current increases sharply and when t = T/4, the current reaches its maximum value and the arc voltage is almost constant. In the following cycle, the current

gradually decreases, by the time of shutdown, the arc voltage increases, then declines to zero and the current also returns to zero.

3. MATHEMATICS MODEL OF ARC FURNACE

To study the properties of the EAFs, it is necessary to build an accurate three-phase model for steady-state analysis and oscillation analysis. The arc melting is a fixed random process, so it is very difficult to make an exact model which leads to many different acrobatic models being built to simulate electric arc furnaces.[3]

The factors that influence the operation of the arc furnace are the molten or refined materials, electrode position, electrode arm control scheme, and the voltage and impedance of the supply system. Therefore, the description of the arc furnace load depends on the following values: arc voltage, arc current, and arc length (determined by the position of the electrode). In general, different methods for arc furnace modeling can be classified into "time domain" and "frequency domain" methods.

Frequency domain analysis method represents the arc voltage and arc current by its harmonic components. These models use several test parameters to reflect arc furnace performance. Since these parameters are experimental and inaccurate, these models are not widely used

Since the arc current is a different nonlinearity and time phenomenon, it is easier to describe its behavior in the time domain than in the frequency domain. The real-time method is the basis for analyzing oscillation processes in electric arc furnaces.

3.1. Hyperbolic model

In this model, the V - I characteristic of the EAF is taken as a voltage function according to the current V = V (I) as shown in Equation (1).[4,5]

$$V(i) = Vat + (C / D + i) \qquad (1)$$

where i and V are the arc current and voltage of a given phase. In addition, Vat is the magnitude

of the voltage at the time of the electrode approach that increases current, which depends on the arc length. Constants C and D are two coefficients that depend on the arc power and the arc current related to the sign of the arc current derivative and they can have different values. Since (1) is similar to the hyperbolic function, it is named the hyperbolic model.

3.2. Exponential model

The V- I characteristic of the electric arc furnace in this model is determined exponentially as follows:[4,5]

$$V(i) = Vat + (1 - e^{i/I_0}) \qquad (2)$$

In the equations describing this model, constant current (I_0) is used to simulate the slope of the positive and negative current, and the exponential function is used to describe the characteristic V - I of the arc. This model can be used in the matter of EAF optimization and reliability.

3.3. Energy conservation model

Because of the importance of the EAF, many characterization models are offered throughout the operation of the equipment. Each model will give a characteristic under different conditions. However, the simulation results of the reference[6] are particularly useful with results that are close to the actual model and can be easily built in other software. Therefore, this model can be applied in research conditions and this result can be used for analysis and evaluation.

We build the dynamic model of the arc according to the differential equations based on the conservation of energy principle.

Equation of the power balance of the arc:

$$p_1 + p_2 = p_3 \qquad (3)$$

Where:

p_1: Capacity to transfer heat from arc furnace to the outside environment.

p_2: The power inside the arc when the arc energy changes, corresponding to the change in the arc radius.

p_3: Total power when the arc is formed and converted to heat.

Based on formula (3) we see that the cooling effect of the arc furnace depends only on the radius r of the arc. Therefore:

$$p_1 = k_1 r^n \qquad (4)$$

This effect is, in fact, related to the temperature of the arc, so this dependency is considered negligible for the simplification of the model. Hence the radius of the arc is treated as a state variable. If the arc surroundings are hot, cooling the arc can be considered independent of the furnace radius. In this case $n = 0$. If the ambient is not hot and the furnace arc is considered to be long then cooling is primarily its side surface and $n = 1$. If the arc radius is short then $n = 2$. [7]

The power component is proportional to the derivative of the energy within the arc radius.

$$p_2 = k_2 r \frac{dr}{dt} \qquad (5)$$

From there we have the final formula for the total capacity:

$$p_3 = vi = \frac{k_3 / r^m}{r^2} i^2 \qquad (6)$$

In this equation the resistivity of the arc is assumed to be inversely proportional to where m has a value between 0 and 2. This reflects the fact that the arc inside the furnace can get hotter if the tank radius optical larger.

Replacing these equations with equation 3, we get the differential equation of electric arc furnaces like (7):

$$k_1 r^n + k_2 r \frac{dr}{dt} = \frac{k_3}{r^{m+2}} i^2 \qquad (7)$$

Arc Radius:

$$r = \int \left(\frac{k_3}{k_2} \frac{i^2}{r^{m+3}} - \frac{k_1}{k_2} r^{n-1} \right) dt \qquad (8)$$

We have arc voltage:[6]

$$v = \frac{k_3}{r^{m+2}} i = R.i \qquad (9)$$

Where: k_1, k_2, k_3, m, n are the constants of the model, r is the radius of the arc in centimeters.

Conceptually, the arc furnace model will simulate the random nature of the arc length. The relationship between the voltage value and the electric arc length is given by (10).[8]

$$e_{arc} = a + bl_{arc} \qquad (10)$$

Where :

e_{arc} : is the instantaneous voltage of the arc

a: is a constant with a value of 40V

b: is the amplification factor from 3.9 to 11.8V

l_{arc} : is arc length

4. MODEL OF ELECTRIC ARC FURNACE SYSTEM

The schematic diagram of the power supply to the EAF is illustrated in Figure 3. In this figure, node 3 (PCC) is the low-voltage busbar that powers the arc furnace and other equipment in the system. To change the active input power of the EAF, we use transformer T_F, (MV / LV). This transformer is equipped with a converter located on the secondary winding so that it is possible to change the voltage of the furnace. In this figure, X_n is the supply reactance and Z_{dz} is the impedance of the cable connected to the transformer TF. The model parameters are shown in Table 1.
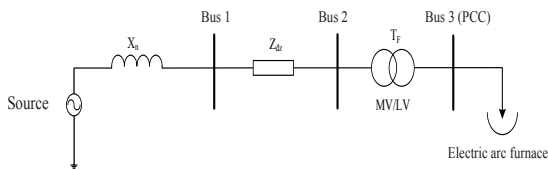
Figure 3. The schematic of the EAF connected to the electrical system

Table 1. Parameter schematic EAF connected to electrical system

Device	Parameter
Source	U = 22 kV; f = 50 Hz; S_{cb} = 100 MVA, X_n = 3 Ω
Line	R = 0,783 Ω/m; X_L = 3,9226 Ω/m; X_C = 4,08 MΩ.m, L = 10 km
Transformer T_F	S_{dm} = 25 MVA; U_1 = 22 kV; U_2 = 0,4 kV; Y/Δ; X = 0,0636pu; X_{st} = 0,2pu; I_o = 0,4%
Electric arc furnace	k_1 = 2.600, k_2 = 0,5, k_3 = 30 [9]

Based on equations (4) to (10) and parameters in Table 1, building the model in Pscad software, we have the results as shown in Figure 4.
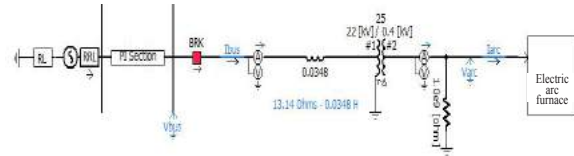
Figure 4. Circuit diagram of electric arc furnace in Pscad software

5. SIMULATION RESULTS

5.1. No voltage fluctuation

The arc furnace model in the paper is generally built as a symmetric three-phase model. For viewing convenience, the selected EAF voltage, current and V-I characteristic values are displayed per phase. From the Formulas (7), (8), (9), after running the simulation, we have arc properties as shown in Figure 5.
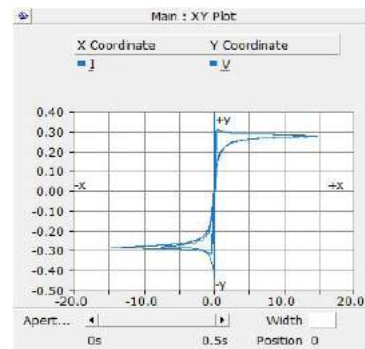
Figure 5. Features V - I electric arc furnace

Figure 6 shows the results of current, voltage and arc resistance corresponding to the model.
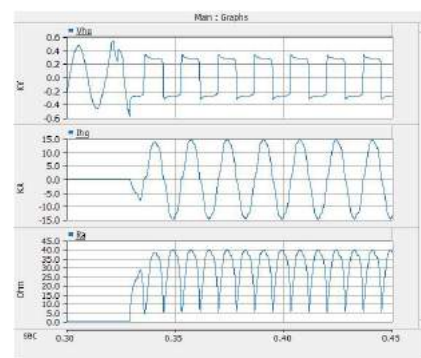
Figure 6. Characteristics of voltage, current and electric arc furnace resistance

The arc voltage has a waveform similar to the square pulse and the current is shaped like a sine wave, but it includes the harmonic components. As shown in Figure 7, the harmonic composition consists of the 1st fundamental harmonic and components Level 3, 5, 7. It has been shown that the model has reflected in detail the properties of electric arc furnaces and it can be used for simulation in the three-phase case.
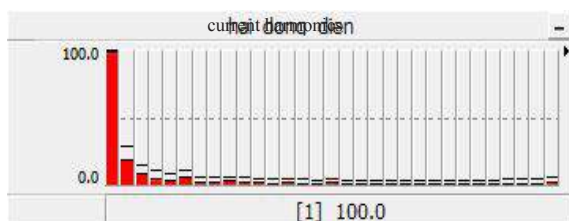

Figure 7. Current harmonic order

With the value of current and arc power, we have the results of active and reactive power as shown in Figure 8. Based on the simulation results, we can see that the arc furnace both consumes active and reactive power. From equation 8, we see that the arc radius depends on the coefficients k_1, k_2, k_3. And when these coefficients change, the active and reactive power will change as shown in Figure 9.
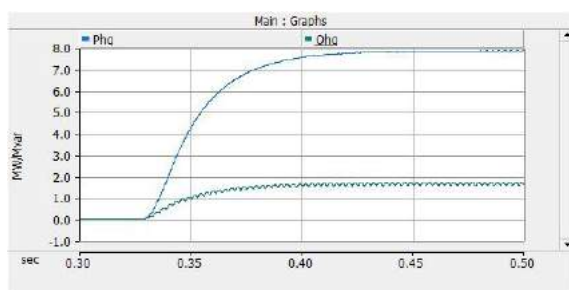
Figure 8. Active and reactive power of electric arc furnaces
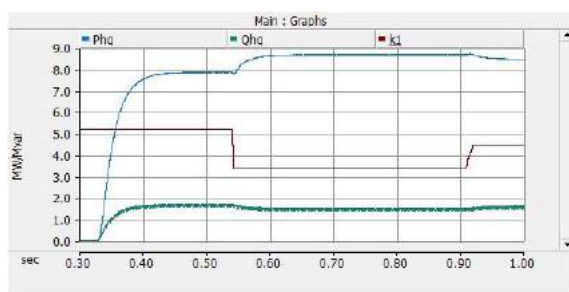
Figure 9. Change the active and reactive power of the electric arc furnace according to the k_1 value

The arc furnace voltage has a square pulse shape, but the voltage on the primary side of transformer TF has a near-sine waveform as shown in Figure 10 and it contains the 3rd, 5th, and 7th harmonic components as shown in Figure 11.
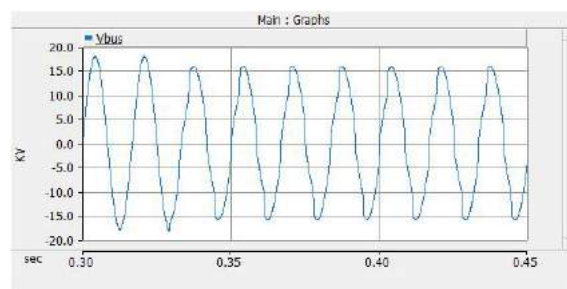
Figure 10. The voltage characteristic on the primary side of transformer T_F
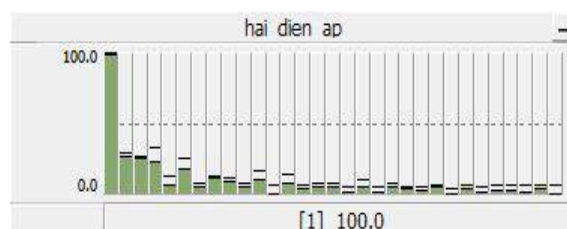
Figure 11. Voltage harmonic order

5.2. Parameter change in electric arc furnace model

We know that arc furnaces' capacity in fact depends on their size. However, to serve the research and simulation process, from Equation (7) we see that the arc furnace capacity is related to the coefficients k_1, k_2, k_3. With k_1, k_2 is constant related to the heat transfer capacity from the arc furnace to the outside environment and the power of the change in arc energy in the furnace. When these values change, the furnace parameters such as voltage, current, and capacity will be affected.

We will examine two change cases k_1 and k_2 starting the simulation with the values $k_1 = 1000$, $k_2 = 0.5$, $k_3 = 30$ and then making incremental adjustment k_1 with the values: 2.000, 3.000, 4.000, 5.000. For easy assessment, ki's impression rate is 1/500 and Vhq_A's impression rate is increased by 10 times. We have the result as shown in Figure 12.
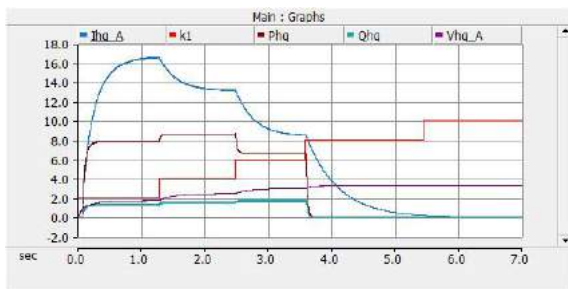
Figure 12. The influence of k_1 on EAF parameters

Based on the graph in Figure 12 we see that when k_1 increases from 1.000 to 3.000 current and active power will decrease. Meanwhile the arc voltage and reactive power will increase. However, when k_1 increases to a value greater than 3.000, the arc voltage will not increase but it remain at a constant value and the active power, reactive power and current will decrease to a very small value.

Similar to k_2, we also start the simulation with $k_1 = 2.600$, $k_2 = 0.5$, $k_3 = 30$ then let k_2 increase with different levels and we have the results as shown in Figure 13.
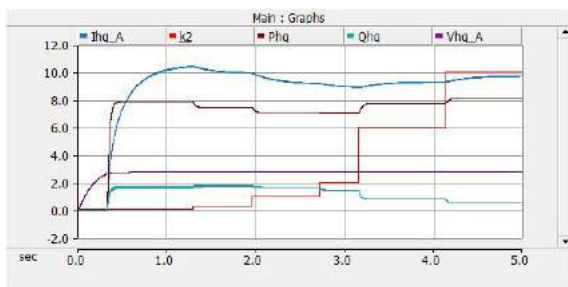
Figure 13. The influence of k_2 on EAF parameters

When k2 increases from 0.5 to 2, current and power will decrease, but when k_2 is greater than 6, active current and power tend to increase again and reactive power continues to decrease. During the k_2 increase, the arc voltage does not change.

5.3. Voltage fluctuations

One of the most common negative effects an arc furnace causes is voltage flicker or flicker. Flicker is caused by rapid change in the load side, namely the operating characteristics of the arc furnace. During the arc furnace operation, the electrodes are short-circuited and generate an extremely large peak current, which then flows into the distribution system and causes extremely rapid fluctuations and voltage instability.

Follow Equation (10) changing the arc length will cause voltage fluctuation. The change of parameter r will affect the parameters during the simulation. The amplitude of r will be adjusted to a sinusoidal signal combined with the noise we can tune. After r changes, the arc voltage value will be recalculated and fed into the system.

* The oscillating component is cyclic

The variation of the parameters in the model will depend on the sinusoidal signal as shown in Equation (11).

$$r_s = r.\left[1 + m_s.\sin(\omega t)\right] \qquad (11)$$

Where :

m_s : Range of oscillation.

ω : Vibration frequency.

* Random oscillation

The model reflects the random change of the arc length close to the Gaussian change due to the fact that metal materials contained in the arc furnace are considered to be randomized even if melting is considered metal caused by the electrode.

Hence a random signal characterizing this arrangement will be used to adjust the amplitude of the arc radius obtained from Equation (12) based on (11)

$$r_g = r_s.\left[1 + m_g.g_n\right] \qquad (12)$$

This randomized signal has a Gausser distribution of g_n and an amplitude of m_g. After running the simulation, we get the results of voltage fluctuations according to the cyclical component (Figure 14), and the case of the periodic oscillation with random oscillation (Figure 15).
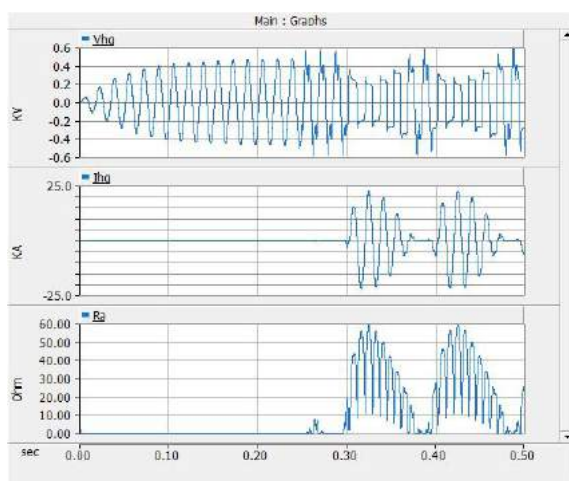
Figure 14. Characteristics of voltage, current and electric arc furnace resistance when the arc radius oscillates are in a sinusoidal cycle
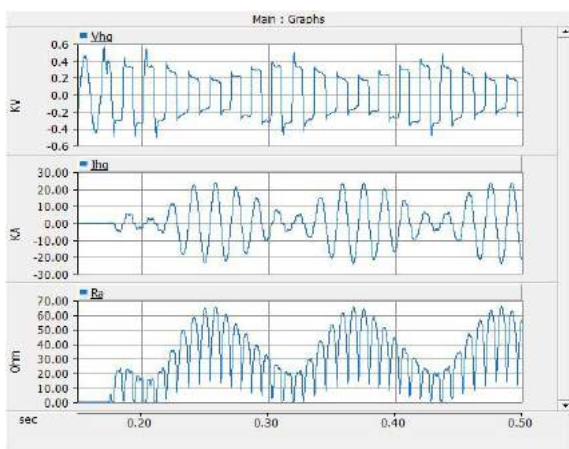

Figure 15. Electric arc furnace voltage, current and resistance characteristics when the arc radius oscillates are in a sinusoidal cycle combined with random oscillation

This change in arc radius also causes voltage and current at the connection point to fluctuate as well. As shown in Figures 16 and 17.
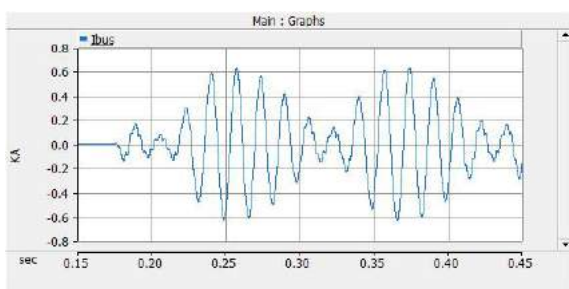

Figure 16. Current characteristics of the primary side transformer when fluctuating voltage
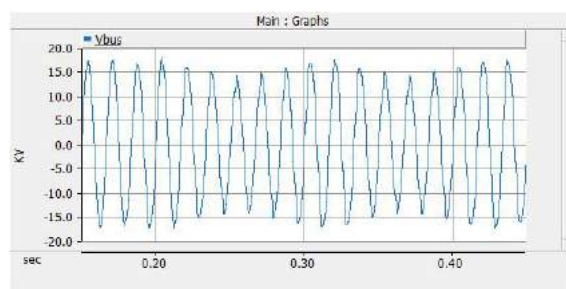
Figure 17. Current characteristics of the primary side transformer when fluctuating voltage

From the simulation results of current and voltage at the connection point as shown in Table 2, we see that the power quality is greatly affected, the voltage THD value difference is about 1,248. THD value of current has a large change about 8.6325. This will affect other devices that connect to this PCC point and cause them to fail quickly.

Table 2. Harmonics results in normal operating state and voltage fluctuation

THD	Normal operating status	Voltage fluctuation	THD value changes with voltage fluctuation
Voltage	51.6088	52.856	1,248
Electric	23.63	32.2652	8,6325

6. CONCLUSION

From the simulation results, it was shown that the operation states of the photovoltaic furnace are based on power balance and voltage fluctuation when the arc radius changes.

In the normal operating state, the electric arc furnace both consumes active and reactive power, and harmonic components when the furnace is operating are also brought to the grid. These values will be large when the arc radius changes, causing voltage fluctuations.

To improve the power quality of electric arc furnaces we can use passive, active filters at low voltage levels such as 22, 0.4 kV and use SVC at higher voltage levels.

REFERENCES

1. P. V. Choi, B. T. Huu, N. T. Ton. *Electrical Instruments*, Scientific and technical publishing, 2006.

2. P. E. King, T. L. Ochs, A. D. Hartman. Chaotic Responses in Electric Arc Furnace, *Journal of appied. physics*, **1994**, *76* (4), 2059-2065.

3. R. Horton, T. Haskew and R. F. Burch. A time domain AC electric arcfurnace model for flicker planning studies, *IEEE Trans. power delivery*, **2009**, *24*, 1450-1457.

4. Golkar, M. A., M. Tavakoli Bina, and S. Meschi. A novel method of electrical arc furnace modeling for flicker study, *In International conference on renewable energies and power quality*, **2007**, 1-8.

5. D. C. Bhonsle and R. B. Kelkar. Simulation of electric arc furnace characteristics for voltage flicker study using matlab, *2011 International conference on recent advancements in electrical, electronics and control engineering*, IEEE, **2011**, 174-181.

6. Hariyanto, Nanang, and M. Nurdin. *Characteristic study of three-phase AC electric arc furnace model,* The 2nd IEEE conference on power engineering and renewable energy (ICPERE) 2014, IEEE, 2014.

7. E. Acha, A. Semlyen, and N. Rajakovic. A harmonic domain computational package for nonlinear problems and its application to electric arcs, *IEEE transactions on power delivery* 5.3, **1990**, 1390-1397.

8. Paschkis, Victor, and J. Persson. *Industrial electric furnaces and appliances*, Interscience Publishers, 1960.

9. Kashani, M. Ghapandar, S. Babaei, and S. Bhattacharya. SVC and STATCOM application in Electric Arc Furnace efficiency improvement, *2013 4th IEEE International symposium on power electronics for distributed generation systems (PEDG),* IEEE, 2013.

Xác định phân bố điện áp trên dây quấn của máy biến áp bằng phương pháp biến trạng thái

Đoàn Thanh Bảo¹, Phạm Quốc Vũ², Phạm Trung Duy³

¹Khoa Kỹ thuật và Công nghệ, Trường Đại học Quy Nhơn, Việt Nam
²Điện lực Phù Mỹ, Công ty Điện lực Bình Định, Việt Nam
³Hạt Quản lý giao thông - công chính huyện Phù Mỹ, Bình Định, Việt Nam

TÓM TẮT

Sự cố quá điện áp thoáng qua ở đầu cực máy biến áp tạo ra dao động điện áp tần số cao xâm nhập vào máy biến áp. Những dao động này có thể gây ra thiệt hại cho cách điện của máy biến áp. Đây thuộc dạng sự cố nặng nề, khó khắc phục và sửa chữa. Chính vì vậy, việc bảo vệ quá áp cho máy biến áp trở thành một vấn đề cấp thiết. Bài báo đã chỉ ra rằng việc sử dụng dây quấn đan xen có điện dung nối tiếp giữa các bánh dây lớn hơn dây quấn xoắn ốc liên tục, có tác dụng phân bố đều điện áp giữa các bánh dây và làm tăng khả năng chịu quá áp. Đồng thời, bài báo đã xác định điện áp trên từng vị trí của bối dây khi chịu xung sét tác động vào đầu cực máy biến áp và phân bố điện áp trên cuộn dây đan xen tại thời điểm khi xung sét có giá trị cực đại. Từ đó kết luận về tính hiệu quả của phương pháp quấn dây đan xen khi sử dụng làm dây quấn máy biến áp.

Từ khóa: *Quá điện áp, dây quấn đan xen, máy biến áp, xung sét, điện dung.*

---

*Tác giả liên hệ chính.
Email: dtbao@ftt.edu.vn

Determination of voltage distribution on winding of transformer by state variable method

Doan Thanh Bao[1,*], Pham Quoc Vu[2], Pham Trung Duy[3]

[1]*Faculty of Engineering and Technology, Quy Nhon University, Vietnam*
[2]*Phu My power, Binh Dinh power company, Vietnam*
[3]*Traffic management station - Public works, Phu My district, Binh Dinh, Vietnam*

ABSTRACT

A transient overvoltage incident at the transformer terminal generates high-frequency voltage fluctuations that have negative impacts on the transformer. These oscillations may cause damage to the insulation of transformers. It is difficult to restore, and repair these serious problems. Therefore, overvoltage protection for the transformers is essential. This paper pointed out that the interleaved disk winding has a larger capacitance than that of continuous disk windings. Therefore, the use of interleaved disk winding has the effect of making the voltage distribution on the winding wheels more even and increasing the overvoltage resistance of the transformer. In addition, the value of the voltage at each position of the winding when lightning impulses on the transformer terminal and the voltage distribution on the interleaved disk winding at the time when the lightning impulse has maximum value are also presented in the article. On that basis, the effectiveness of using the interleaved disk winding method in the transformer will be analyzed in detail.

Keywords: *Over voltage, interleaved disk-type winding, transformer, lightning strike, capacitance.*

1. INTRODUCTION

Among the types of transformer faults, the fault caused by overvoltage is the most serious, difficult to fix and repair. Atmospheric overvoltage usually occurs in a very short period of time, but the voltage applied to the terminal has a great amplitude and slope values which are very dangerous for the transformer windings. Therefore, the overvoltage protection for transformers becomes an urgent issue in the process of designing, manufacturing, testing and operating transformers.[1] The methods of overvoltage protection used today are discharge electrodes, lightning arresters or capacitive rings.[2]

At industrial electrical frequencies, the role of capacitive elements is negligible and often ignored. When a voltage pulse acts on the terminal of the transformer windings, which contains high-order harmonic elements, the role of the capacitive elements becomes much more significant.[3] At this time, the voltage acts on the winding terminals are greatly reduced on a few first gallet. Therefore, these gallets usually increase the insulation or they are connected in parallel with an equipotential electrode known as a capacitive ring.[4,5]

The capacitive ring works to increase the capacitance of the winding at the terminal position. However, with large capacity

Corresponding author.
*Email: dtbao@ftt.edu.vn*

transformers, high voltage and high production costs, it is also necessary to increase the capacitance value of the inner coils. That is the method of interleaved disk winding.[5,6]

The paper calculated the series and parallel capacitance of types of continuous disk windings and interleaved disk windings when they are of the same geometric size. The results showed that the interleaved disk winding has a greater capacitance than continuous disk winding. Furthermore, the paper used the equivalent circuit model and the state variable method solved on Matlab Simulink software to determine the voltage distribution across the nodes of the winding at the time when the value of lightning impulse voltage is maximum. The distribution of the voltage on the interleaved disk winding at the moment when the lightning impulse is maximum value is also determined by this measure.

2. BUILDING MODEL OF THE WINDING

2.1. Initial voltage distribution

When a voltage pulse acts on the terminals of the transformer winding, the voltage at the initial time distributed in the windings depends on the capacitance between the rings, the capacitance between the winding wheels, the capacitance between the windings each other and between the windings and ground.[7] The inductance and inductor of the winding have no effect on the initial voltage distribution. Therefore, inductance does not allow current to flow and the voltage distribution is determined by the capacitive network. When the impulse voltage remains for a sufficiently long time (50 - 100 μs), current begins to flow through the inductance significantly. Eventually, this forms a stable voltage distribution. Thus there is a difference between the initial voltage distribution and the stable voltage distribution, the values of voltage are shown in Figure 1.[1,4]
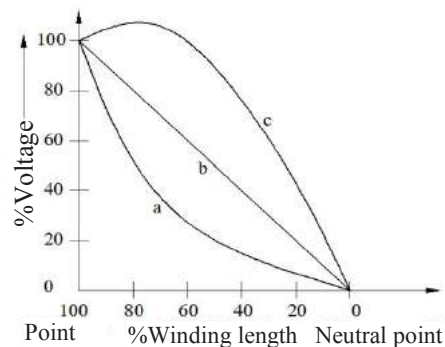
a) Initial voltage distribution; (b) The stable voltage distribution; (c) Maximum voltage

Figure 1. Voltage distribution in the winding[1,4]

In Figure 1, it is seen that at the beginning, the voltage drops suddenly at a point about 20% of the length of the winding, then slowly decreases in the rest. Hence the intensity of electrical current between the first gallets of the windings (2 - 5 first gallets) is much greater than that between the rest of the gallets. In addition, there are times when the maximum voltage value at a certain point on the windings are greater than the applied voltage. Therefore, in order to increase the ability of overvoltage of the windings, it is necessary to make the initial voltage distribution closer to the stable voltage distribution.[6]
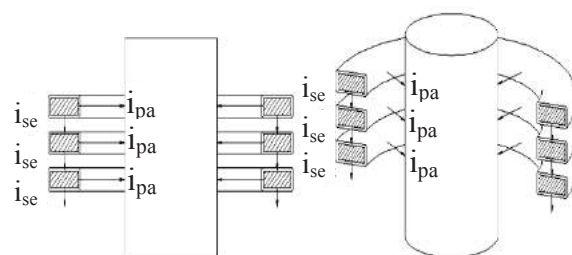

Figure 2. Capacitance current distribution of single-layer winding

The voltage distribution across the rings now depends on the capacitance value of the windings (between windings and ground or between the rings).

Where, C_{se} is the sum of the series capacitance between the rings and the capacitance between the gallets or the capacitance between

parts of the winding; C_{pa} is the sum of parallel capacitance between the windings and steel core, the capacitance between the windings and the machine shell.

The initial voltage distribution was determined by the distribution coefficient:[8, 9]

$$\alpha = \sqrt{\frac{C_{pa}}{C_{se}}} \qquad (1)$$

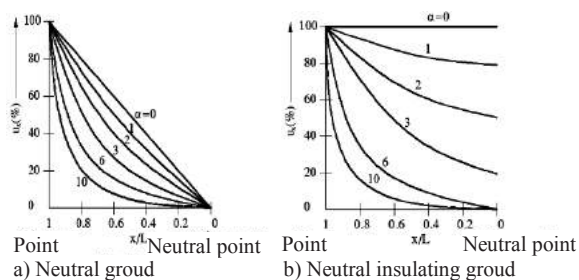For different values of α, the initial voltage distribution is shown in Figure 3.

Point   Neutral point   Point   Neutral point
a) Neutral groud   b) Neutral insulating groud

Figure 3. The initial voltage distribution[1,4]

The coefficient α indicates the deviation of the original voltage distribution line from the stable voltage distribution line. The higher the coefficient α is, the larger the difference is. In order to reduce the distribution coefficient α, there are two ways. One solution is that the value of C_{pa} must be decreased, and another one is that the value of C_{se} must be increased. However, the reduction of value in C_{pa} involves varying the spacing between the strings, which is often fixed by early design requirements. Therefore, it is common to choose to increase C_{se} by changing the winding method. The method of interleaved disk winding is an effective method used today.[6]

Figure 4. A pair of gallets of interleaved disk winding

Figure 4 shows a simple interleaved disk winding model, consisting of a single 2-gallet circuit, 8 turns per gallet, the number of turns per gallet equivalent to a spiral winding. However, the performance of winding the interlacing pattern is more complicated because welding is required on each pair of gallet and the insulation between the coils of the winding is also required higher.

2.2. Calculating parallel capacitance

The parallel capacitance between the gallets and the steel core is the capacitance of a cylindrical capacitor with one side being the innermost ring, the other side being the steel core. This capacitor is filled with two dielectric zones, the insulating paper and the transformer oil. Applying the formula to calculate the capacitance of the capacitor in a homogeneous atmosphere the capacitance between two concentric wires, or between the inner coils and the steel core is calculated as follows:[4,8]

$$C_{pa} = \frac{C_{ins}.C_{oil}}{C_{ins} + C_{oil}} \qquad (2)$$

$$\text{with } C_{ins} = \varepsilon_0.\varepsilon_{ins} \frac{\pi D_m h}{d_{ins}} \qquad (3)$$

$$\text{and } C_{oil} = \varepsilon_0.\varepsilon_{oil} \frac{\pi D_m h}{d_{oil}} \qquad (4)$$

Where,

D_m is the mean diameter of the gap between the two windings

d_{oil} and d_{ins} are the thickness of the oil and the insulation between the two windings, respectively

h is the height of the wire wheel in the axial direction

ε_0, ε_{oil} and ε_{ins} are the dielectric constants of the vacuum, the oil and the insulation paper, respectively.

These dimensions are shown in Figure 5

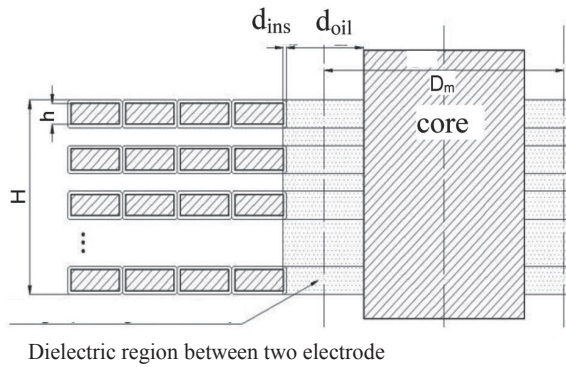Dielectric region between two electrode

Figure 5. Cross-section of inner winding and core

From (3) and (4), we have:

$$C_{pa} = \frac{\varepsilon_0 \pi D_m h}{\dfrac{d_{ins}}{\varepsilon_{ins}} + \dfrac{d_{oil}}{\varepsilon_{oil}}} \qquad (5)$$

The formula is used to determine the capacitance between the outer winding and one side of the transformer's shell:

$$C_{pa} = \frac{\varepsilon_0 \pi D_m h}{\cosh^{-1}(\dfrac{s}{R})} \left[\frac{d_{oil} + d_{ins}}{\dfrac{d_{ins}}{\varepsilon_{ins}} + \dfrac{d_{oil}}{\varepsilon_{oil}}} \right] \qquad (6)$$

Where,

h and R are the heights and radius of the winding, respectively.

s is the distance from the center of the wire to the shell.

2.3. Serial capacitance calculation

2.3.1. Series capacitance in continuous disk winding

Similar to the calculation of parallel capacitance, the axial capacitance between two physically adjacent gallets is the capacitance of three capacitors connected in series as shown in Figure 6.[4,10]
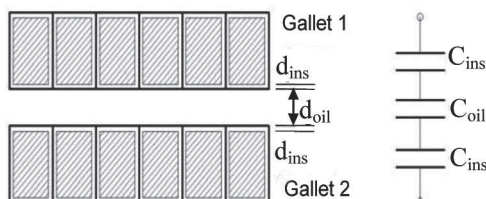
Figure 6. Capacitance between two gallets

The capacitance between coils is calculated by the formula:

$$C_V = \frac{\varepsilon_0 . \varepsilon_{ins} \pi D_m h}{2 d_{ins}} \qquad (7)$$

The capacitance of the capacitor, which the dielectric is the insulating paper and the transformer oil, is calculated by the formula:

$$C_{DA} = \frac{\varepsilon_0 \pi D_m R}{\dfrac{2 d_{ins}}{\varepsilon_{ins}} + \dfrac{d_{oil}}{\varepsilon_{oil}}} \qquad (8)$$

Where R is the radial thickness.

Assume that C_V and C_B are capacitance between physically adjacent turns and between two opposite turns of a pair of gallets as shown in Figure 7.
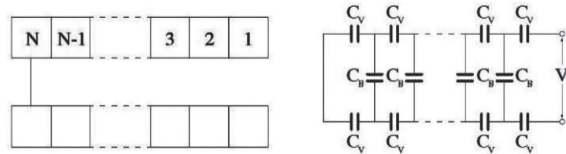

Figure 7. A pair of gallets in continuous disk winding

The total series capacitance of a pair of gallets is:

$$C_{se} = \frac{C_V}{2N^2}(N-1) + \frac{(N-1)(2N-1)C_B}{6N} \qquad (9)$$

or $\qquad C_{se} = \dfrac{C_V}{2N^2}(N-1) + \dfrac{C_{DA}}{3} \qquad (10)$

2.3.2. Series capacitance in interleaved disk winding

With the interleaved disk winding shown in Figure 4, the voltage acts on N (turns of a gallet) is V/2, and the voltage acts on (N-2) (turns of a gallet) is [(N-1)/2N]*V, the total energy in gallets is [2]:

$$E_n = \frac{1}{2} C_V \left(\frac{V}{2}\right)^2 N + \frac{1}{2} C_V \left(\frac{N-1}{2N} V\right)^2 (N-2) \qquad (11)$$

In addition to this: $E_n = \dfrac{1}{2} C_{Vtd} V^2$

Therefore, we have:

$$C_{Vtd} = \frac{C_V}{4} \left[N + \left(\frac{N-1}{N}\right)^2 (N-2) \right]$$

If N >> 1, the series capacitance between the two wire wheels is:

$$C_{se} = C_{Vtd} = \frac{C_V}{2}(N-1) \qquad (12)$$

2.4. Calculation of inductance between the rings

The formula for calculating the inductance between two rings have the small cross-section, coaxial is calculated by [3] [4]:

$$L_{AB} = \frac{2\mu_0}{k} N_A.N_B\sqrt{R_A R_B}\left\{\left[1-\frac{k^2}{2}\right]K(k)-E(k)\right\} \quad (13)$$

Where,

$$k = \sqrt{\frac{4R_A R_B}{(R_A + R_B)^2 + S^2}}$$

R_A, R_B are the radius of the two winding A and B, respectively

S is the distance between the two rings

N_A and N_B are the number of winding A and wingding B, respectively

K(k) and E(k) are complete elliptic integrals of types 1 and 2.

$$K(k) = \int_0^{\frac{\pi}{2}} \frac{d\theta}{\sqrt{1-k^2\sin^2\theta}} \text{ and } E(k) = \int_0^{\frac{\pi}{2}} \sqrt{1-k^2\sin^2\theta}\ d\theta$$
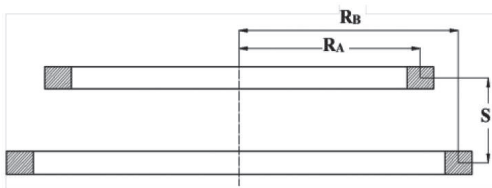
Figure 8. Cross section of two coaxial rings

3. CALCULATION OF VOLTAGE DISTRIBUTION

3.1. Equivalent circuit model

The equivalent circuit model of the transformer windings is depicted in Figure 9. Conductor G has an extremely small value and does not affect the initial voltage distribution, because at the initial moment the current flowing through

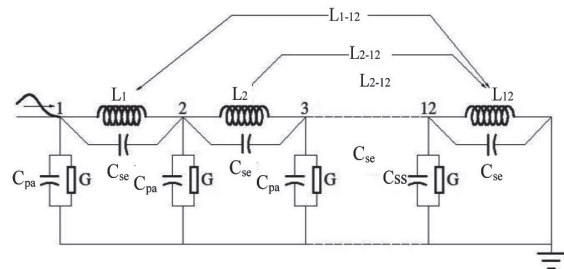the inductor is almost zero, only current flows through capacitance.

Figure 9. Equivalent circuit of the windings

The equivalent circuits include the following components:

C_{se} is the series capacitance between the wire wheels,

C_{pa} is the parallel capacitance between the wire wheels,

L_i, L_{ij} are the inductance of the wire wheels and the mutual inductance between the wire wheels, respectively,

G is conductance of the wire wheels.

Considering of an transformer with following parameters, S = 2.200 kVA – 22/0.4 kV. Wire wheel dimensions (in centimetres) of this transformer are shown in Figure 10.
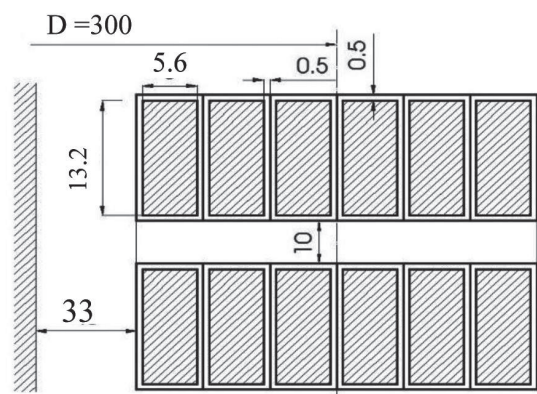

Figure 10. Surveyed transformer's dimensions of wire wheel

Using equations (2), (10) and (12) to calculate for transformer whose parameters are supplied in Figure 10, obtained results are shown in Table 1.

Table 1. Parallel and series capacitance

Obtained results	C_{pa} (Parallel capacitance)	C_{secw} (Series capacitance in a continuous disk winding type)	C_{seiw} (Series capacitance in interleaved disk winding)
Capacitance (F)	$0.551*10^{-7}$	$1.46*10^{-7}$	$36.0*10^{-7}$

Similarly, using equation 13 to calculate for transformer whose parameters are supplied in Figure 10, results calculated by Matlab/ Simulinks software are shown in Table 2.

Table 2. The inductance of the wire wheels and the mutual inductance between them (the unit of measure is the Herry)

$L_{1-1} = 5.1957*10^{-5}$	$L_{1-5} = 2.1926*10^{-5}$	$L_{1-9} = 1.5060*10^{-5}$
$L_{1-2} = 3.6287*10^{-5}$	$L_{1-6} = 1.9575*10^{-5}$	$L_{1-10} = 1.4076*10^{-5}$
$L_{1-3} = 2.9391*10^{-5}$	$L_{1-7} = 1.7733*10^{-5}$	$L_{1-11} = 1.3262*10^{-5}$
$L_{1-4} = 2.5033*10^{-5}$	$L_{1-8} = 1.6258*10^{-5}$	$L_{1-12} = 1.2584*10^{-5}$

3.2. Calculation of voltage distribution by the state variable method
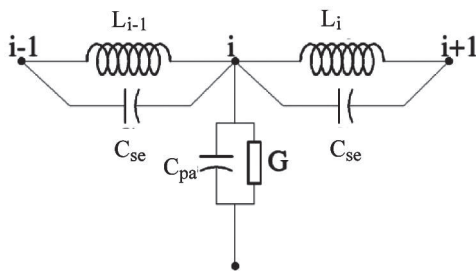

Figure 11. Any node from an equivalent circuit

Choose a random node from the equivalent circuit shown in Figure 11.

The general equation of the equivalent circuit is shown as follows [4]:

$$\hat{C}\ddot{y}(t) + \hat{G}\dot{y}(t) + \hat{\Gamma}\hat{y}(t) = 0 \tag{14}$$

Where,

$\hat{C}$ is the node capacitance matrix,

$\hat{G}$ is the node conductance matrix,

$\hat{\Gamma}$ is the inverse node inductance matrix,

$\hat{y}(t)$ is the voltage vector at the nodes.

The relationship between the node matrices and the branch matrices is shown as follows:

$$\hat{C} = Q_C C_b Q_C^T \tag{14a}$$

$$\hat{G} = Q_G G_b Q_G^T \tag{14b}$$

$$\hat{\Gamma} = Q_L L_b^{-1} Q_L^T \tag{14c}$$

Where, Q_C, Q_L and Q_G are interdependent matrices between the node and branch with capacitance, inductance and conductivity. C_b, L_b, G_b are the branch capacitance matrix, inductance matrix and branch inductance matrix, respectively.

3.2.1. State variable model

The system of equations of state variables describing the voltage distribution in the transformer is shown in Equation 15

$$\begin{aligned} \dot{X}(t) &= AX(t) + Bv(t) \\ y(t) &= FX(t) + Dv(t) \end{aligned} \tag{15}$$

Where,

X (t) is state variable vector,

A, F are constant coefficient matrix,

F, D are column matrix of the constant coefficients,

v (t) is input pulse voltage vector,

y(t) is output node voltage vector.

3.2.2. Input voltage block

The voltage applied to the winding terminals is assumed to be a standard lightning impulse voltage 1/50. This is the most common type of lightning wave and causes many problems for lines and transformer stations. The values of lightning impulse voltages are expressed algebraically as follows:

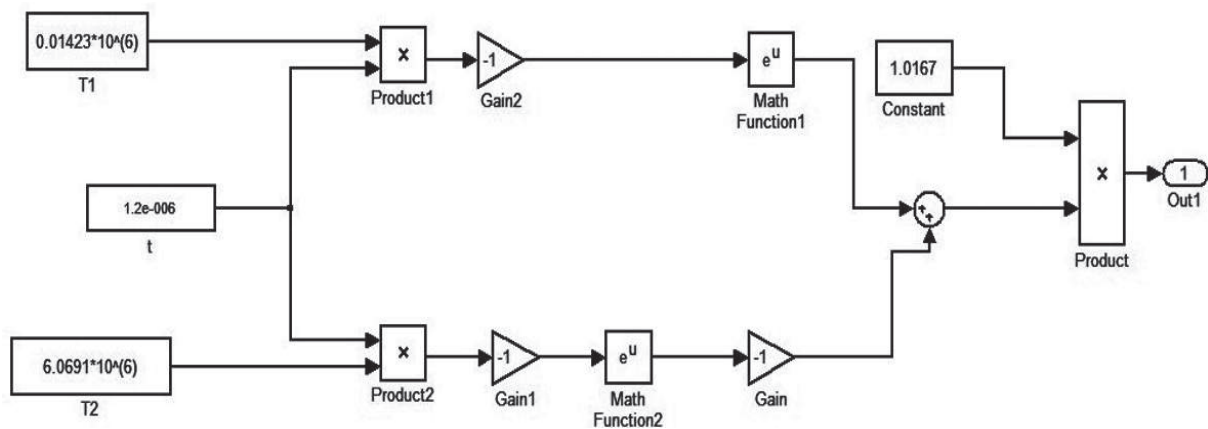$$x(t) = 1,0167U(e^{-0,01423t} - e^{-6,6091t}) \tag{16}$$

Figure 12. Lightning impulse voltage stimulating block

To build the input voltage model, blocks in the Matlab/Simulink software are used. The output of the block model (Figure 12) is the unit lightning impulse voltage value. This result is shown in Figure 13.
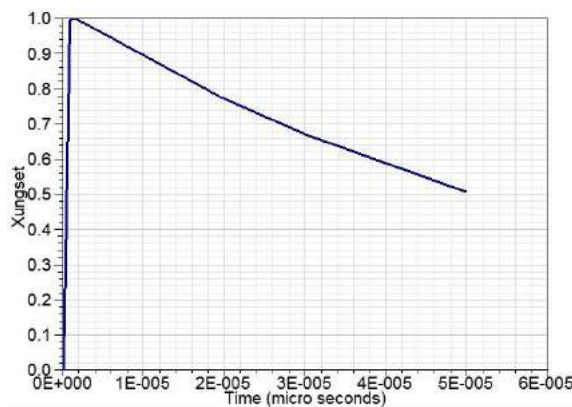

Figure 13. Type of output voltage of lightning impulse block

3.2.3. Simulation model

Parametric matrices A, B, F, D in the system of equations 15 are solved by matlab programming code. State-Space blocks and sub-blocks are also built on Matlab Simulink software. The full simulation diagram is shown in Figure 14.
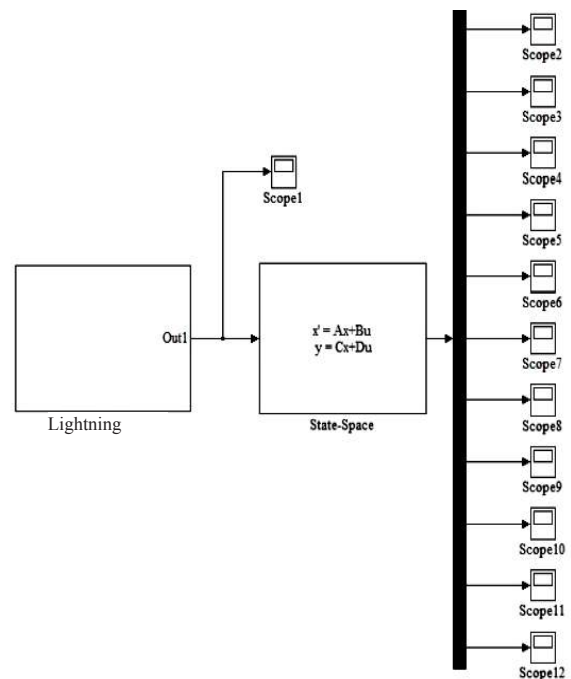

Figure 14. Full block diagram in Matlab Simulink software

The simulation diagram in the Matlab Simulink software (Figure 14) is used to determine the voltage distribution on both continuous disk windings and interleaved disk winding.

3.2.4. Obtained simulation results for continuous disk winding

Table 3. Voltage values at 12 nodes on continuous disk winding

Node 1	Node 2	Node 3	Node 4	Node 5	Node 6
1.0000	0.3023	0.0906	0.0275	0.0076	0.0021
Node 7	Node 8	Node 9	Node 10	Node 11	Node 12
0.0007	0.0002	0.0001	0.0001	0.0001	0.0002

The obtained simulation result of the voltage at node 2 of the continuous disk winding is showed in Figure 15.
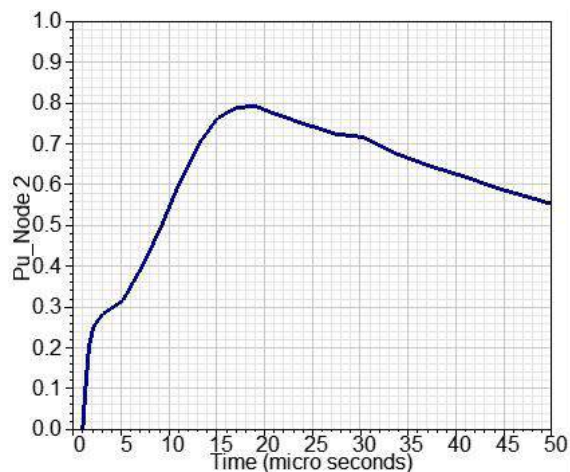

Figure 15. The voltage at node 2 - Type of continuous disk winding

Similarly, Table 3 shows the simulation results of voltage values at the remaining 11 nodes at the time of 50 μs. The voltage pattern at the nodes is the same and has a value decreasing with the length of the winding. To find out the rate of decline, the values of voltage at the nodes at the same time to be 1 μs (the time when the voltage impulse reaches its maximum and is the most dangerous) are simulated by Matlab/Simulink software. These voltage values are shown in Table 3.
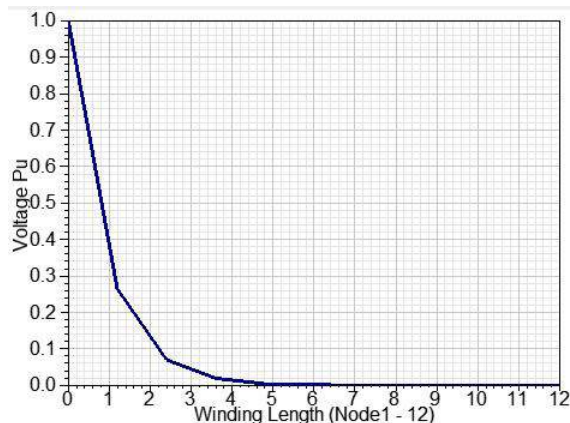
The voltage values at the 12 nodes are shown in Figure 16.

Figure 16. Voltage distribution at the 12 nodes at the time 1μs - continuous disk winding

Figure 16 shows that the initial voltage distribution of a continuous disk winding is in the form of a hyperbolic line which is different from the established voltage distribution line (straight line). The voltage has a very large value at the winding area between node 1 and node 2 (70%), this is the first gearing position. The rest of the winding is focused on 30% of the voltage. Uneven voltage distribution over a short period of time at the moment of transition causes insulation breakdown and failure in the transformer.

3.2.5. Obtained simulation results for interleaved disk winding type

Conducting the simulation for the case of interleaved disk winding type, the values of output voltage at the nodes depicted in Figure 17.
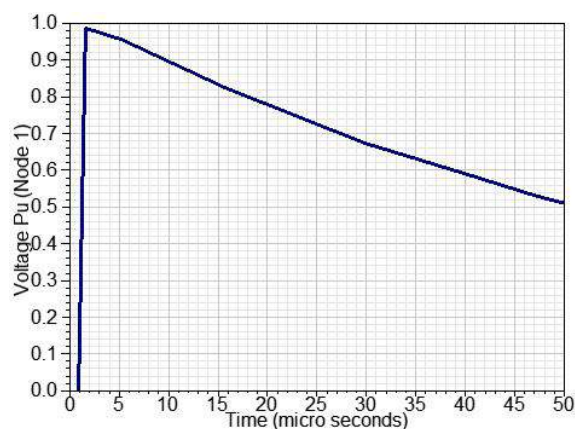

Figure 17. Voltage values at node 1 - Interleaved disk winding

Similarly, voltage values at the remaining 11 nodes are shown in Table 4.

Table 4. Voltage values at 12 nodes on interleaved disk winding

Node 1	Node 2	Node 3	Node 4	Node 5	Node 6
1.0000	0.7765	0.5968	0.534	0.4366	0.3023
Node 7	Node 8	Node 9	Node 10	Node 11	Node 12
0.213	0.1326	0.112	0.0856	0.0501	0.0324

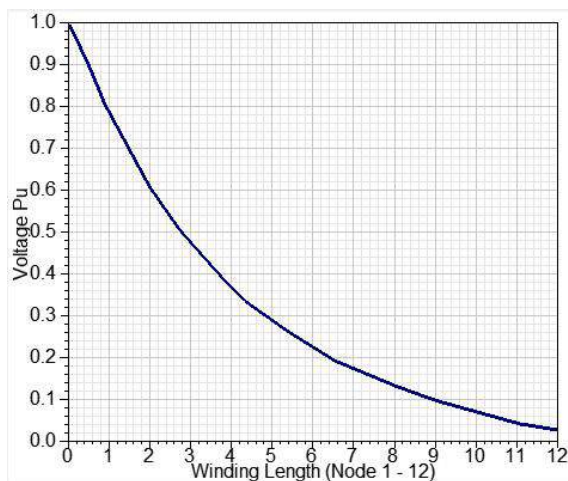The voltage values at the 12 nodes on the winding are shown in the graph in Figure 18.

Figure 18. Voltage distribution at the 12 nodes at the time 1μs - interleaved disk winding

Figure 18 shows that the initial voltage distribution of the interleaved disk winding is close to the linearly stable distribution line. Compared with continuous disk winding, the voltage distribution on interleaved disk winding is better.

4. CONCLUSION

The paper used the state variable method solved on Matlab Simulink software to determine the voltage distribution across the nodes at any time and the voltage distribution across the winding at the time the lightning pulse voltage reaches its maximum value.

The paper has presented visual comparison results of the voltage distribution across two windings - continuous disk winding and interleaved disk winding. The results showed that the interleaved disk winding method has an initial voltage distribution close to that of a linearly stable distribution line. This means that the voltage distribution on the interleaved disk winding *is* more uniform than that on the continuous disk winding.

Compared with capacitance-related methods: using a capacitive ring, an electrostatic membrane, or adding capacitors to the winding, the interleaved disk winding method is much more effective in terms of improving the initial distribution voltage on the winding. Therefore, this method is commonly used for transmission transformers which are frequently affected by high voltage impulses or switching transients.

REFERENCES

1. Pham Van Binh and Le Van Doanh. Transformers - theory - operation - maintenance - test, Science and Technology publishing, Hanoi, 2011.

2. R. M. Del Vecchio, B. Poulin, R. Ahuja. Calculation and measurement of winding disk capacitances with wound-in-shields, *IEEE transactions on power delivery*, **1998**, *13*(2), 503–509.

3. J. H. McWhirter, T. M. Ising, K. S. Kirk. Calculation of impulse voltage stresses in transformer windings, *IEEE proceedings transmission and distribution conference*, **1996**, 579–585.

4. S. V. Kulkarni, S. A. Khaparde. Surge Phenomena in Transformer, *Transformer engineering design and practice*, Indian Institute of Technology, Bombay, Mumbai, India, 2000, 277–326.

5. T. Wang, Z. Wang, Q. Zhang, L. Li. Measurement method of transient overvoltage distribution in transformerwindings, *2013 Annual report conference on electrical insulation and dielectric phenomena*, 1093–1096.

6. O. Moreau, P. Guuinic, R. Dorr, Q. Su, Comparison between the high frequency characteristics of transformerinterleaved and ordinary disk windings, *IEEE power engineering society winter meeting*, **2000**, *3*, 2187–2192.

7. M. Heidarzadeh, M. R. Besmi. Influence of transformer layer winding parameters on the capacitive characteristic coefficient, *International journal on technical and physical problems of engineering*, **2013**, *5*(15), 22-28.

8. M. Bagheri, A. Hekmati; R. Heidarzadeh; M. Salay Naderi, Impulse voltage distribution in intershield disk winding VS interleaved and continuous disk winding in power transformer, *IEEE 2nd International power and energy conference*, **2008**, 387-392.

9. M. Bagheri, M. S. Naderi, T. Blackburn, D. Zhang. Transformer Frequency Response Analysis: A mathematical approach to interpret mid-frequency oscillations, *2012 IEEE International conference on power and energy (PECon)*, 962–966.

10. M. Bagheri, B. T. Phung, T. Blackburn. Transformer frequency response analysis: mathematical and practical approach to interpret mid-frequency oscillations, *IEEE transactions on dielectrics and electrical insulation*, **2013**, *20*(6), 1962–1970.

Nghiên cứu một số đặc điểm sinh học và khả năng sản xuất của nấm Milky *(Calocybe indica)* trồng trên các giá thể khác nhau tại Trường Đại học Quy Nhơn

Ngô Hồng Đức[1,*], Lê Vương Hải Nguyệt[2]

[1]Khoa Khoa học Tự nhiên, Trường Đại học Quy Nhơn, Việt Nam
[2]Khoa Sư phạm, Trường Đại học Quy Nhơn, Việt Nam

TÓM TẮT

Mục tiêu nghiên cứu của đề tài nhằm xác định khả năng sinh trưởng và năng suất nấm Milky (*Calocybe indica*) trong điều kiện nuôi trồng ở thành phố Quy Nhơn, tỉnh Bình Định. Nấm Milky được trồng trên 4 công thức, CT1: mùn cưa + đất phù sa; CT2: mùn cưa + đất phù sa + tro trấu nung; CT3: mùn cưa + đất cát pha; CT4: mùn cưa + đất cát pha + tro trấu nung vào mùa mưa và mùa nắng trên đơn vị diện tích là 30m². Kết quả cho thấy nấm Milky nuôi trồng được quanh năm trong điều kiện thời tiết Bình Định. Năng suất cao nhất là ở CT2, mùa mưa năng suất đạt 640,93 kg/1.000 bịch phôi, lợi nhuận đạt là 17.927.200 đồng, mùa nóng năng suất đạt 590,40 kg/1.000 bịch phôi, lợi nhuận đạt là 15.906.000 đồng trong vòng 3,5 tháng. Nhìn chung kết quả nghiên cứu cho thấy nấm Milky (*Calocybe indica*) thích hợp với điều kiện nuôi trồng tại thành phố Quy Nhơn, tỉnh Bình Định, góp phần làm phong phú thêm các loại nấm ăn nuôi trồng ở tỉnh.

Từ khóa: *Nấm Milky, Calocybe indica, cơ chất, khả năng sinh trưởng, năng suất.*

---

[*]Tác giả liên hệ chính.
Email: ngohongduc@qnu.edu.vn

Study on some biological characteristics and yield capacity of milky mushroom (*Calocybe indica*) cultivated on different substrates at Quy Nhon University

Ngo Hong Duc[1],*, Le Vuong Hai Nguyet[2]

[1]Faculty of Natural Science, Quy Nhon University, Vietnam
[2]Faculty of Pedagogical Sciences, Quy Nhon University, Vietnam

ABSTRACT

The aim of this study was to determine the ability of growth, and yield for Milky mushroom (*Calocybe indica*) cultivated under climatic conditions in Binh Dinh province. Milky mushroom was cultivated on four different substrates: sawdust + alluvial soil (treatment 1); sawdust + alluvial soil + rice husk ash (treatment 2); sawdust + loamy soil (treatment 3); sawdust + loamy soil + rice husk ash (treatment 4). The experiment was carried out in an area of 30 squarre metres in two seasons: rainy and sunny season. The highest economic yields obtained were 640.93 kg/1000 spawned bags with net profit of 17.927.200 VND for treatment 2 in rainy season and 590.4 kg/1000 spawned bags with 15.906.000VND profit in the duration of 3.5 months. Generally, research results showed that Milky mushroom is suitable with cultivated condition in Quy Nhon of Binh Dinh province, contributing to the enrichment of mushroom cultivated in province.

Keyword: *Milky mushroom, Calocybe indica, substrate, growth ability, yield.*

1. INTRODUCTION

Like other mushrooms, milky mushroom (*Calocybe indica* P&C) have sweet taste and coldness. The nutrition values of Milky mushrooms are rich in protein, vitamins and minerals. Krishnamoorthy *et al.* reported 32.2% protein (dry weight) in a medium sized milky mushroom.[1] Vitamin content of Milky mushroom is higher than that of Abalone mushrooms (Oyster mushroom).[1,2] Most of the mushrooms are rich in B complex vitamins (thiamine, riboflavin, pridoxine, pantothenic acid, nicotinic acid, nicotinamide, folic acid, and cobalamin); as well as ergosterol and biotin, vitamin A in fresh and dry Milky mushrooms have been reported to be

0.35 mg and 0.275 mg.g^{-1}, respectively.[3] Water soluble vitamin C (a free radical scavenger and a well-known antioxidant and inhibitor of lipid peroxidation has been reported in fresh and dry white milky mushrooms (1.03 and 0.4 mg/100 g, respectively).[4] Mushrooms are a good source of biological active compounds that protect the human body against several chronic and degenerative diseases. Milky mushrooms are rich in ergothioneine (an antioxidant that protects body parts for fighting against free radical). The beta-glycans present in dietary fibers of mushrooms are reported to have stimulatory effect on immune system with anti-mutagenic, anticancer and antitumor activities.[5] Mushrooms

*Corresponding author.
Email: ngohongduc@qnu.edu.vn

are good sources of minerals (Ca, K, Mg, Na, and P), trace elements (Cu, Fe, Mn, and Zn) and sometimes, toxic heavy metals (Cd and Pb) as compared to vegetables.[6]

Milky mushroom was introduced to Vietnam in 2007, and grown widely in many provinces such as Hanoi, Ninh Binh, Da Nang, Ho Chi Minh city, etc. But the study on biological characteristics of this mushroom is very limited[7]. In 2015, Milky mushroom was introduced and cultivated at the Center for Applied Science and Technology of Binh Dinh province in the first study and evaluation of its biological characteristics. However, the research was carried out in small-scale at one season.

Based on the listed reasons, it is necessary to study some biological characteristics and yield capacity of Milky mushroom grown on different substrates at Quy Nhon University.

2. MATERIALS AND METHODS

2.1. Experimental design

First grade mycelia were cultured in vitro on PGA (potato, glucose, agar) medium, and secondary grade mycelia were cultured in sterilized paddy grains. For sprawn media, base substrate (BS) of 250 kg of sawdust + 5 kg of lime powder + 20 kg of rice bran + 100 liters of water. The experiment consists of treatments: Treatment 1: 51 kg of BS + 5 kg of alluvial soil; Treatment 2: 51 kg of BS + 5 kg of alluvial soil + 2 kg of rice husk ash; Treatment 3: 51 kg of BS + 5 kg of sandy soil; Treatment 4: 51 kg of BS + 5 kg of sandy soil + 2 kg of rice husk ash.

Sterilized substrates were mixed according to the ratio of each treatment. The substrate was then transferred into polypropylene bags of 20 x 36 cm in sizes, the openings of the bags were plugged with cotton and secured with plastic rings. The average weight of spawn bag is from 1.6 kg to 1.7 kg. Each treatment includes 30 spawn bags. The experiment was conducted in rainy season (RS) from September to November and dry season (DS) from May to July.

2.2. Indicator measurements

Contamination rate (%) – the rate of contaminated bags, length and diameter of stalk (cm) – measure on fruiting bodies at harvest, thickness of mushroom pileus (cm) – measure at thickest pileus part, biological yield (g/spawned bag) – total fresh mass of harvested fruiting bodies, economic profit (VND/1000 bags) – the income after deducting expenses.

2.3. Statistical analysis

The data of experiment were statistically analyzed using MS. Excel and Statistix 8.0.

Table 1. Contamination rate of culture media (%)

Media for	Bag total	Amount of contaminated bags	Amount of uncontaminated bag	Contamination rate (%)	Successful rate (%)
Grade 1 mycelia	20	1	19	5	95
Grade 2 mycelia	20	2	18	10	90
Spawning in RS	150	4	146	3.3	96.7
Spawning in DS	150	5	145	4	96

The data from Table 1 shows that the contamination rates differ from the different media: PGA medium for grade 1 mycelia (5%), sterilized paddy for grade 2 mycelia (10%), spawn media in rainy season (3.3%) and in dry season (4%). The results showed that Milky mushroom has high resistance in local condition. The rate of spawning success could search to 96.7%.

3. RESULTS AND DISCUSSIONS

3.1. Contamination rate

The contamination rate of cultivation media is one of the criteria to evaluate the mushroom adaptability. The results are presented in Table 1.

3.2. Mycelial growth rate of Milky mushroom

The mycelial growth rate of mushroom is assessment indicator of growth and development in mushroom cultivation. The results of mycelial growth on cultural media are presented in Table 2.

Table 2. Mycelial growth rate of Milky mushroom (days)

Media for	Half mycelial colonization	Complete mycelial colonization
Grade 1 mycelia	12	21
Grade 2 mycelia	20	35
Spawn bags	29	47

The data shows that the mycelial growth rate of Milky mushroom is different in the culture media: PGA medium for grade 1 mycelia (21 days), sterilized paddy for grade 2 mycelia (35 days), and spawn bag (47 days). Thus, the mycelial growth rate of Milky mushrooms is relatively slow in comparison with other mushrooms, such as abalone mushroom: 15 - 16 days, 20 - 25 days, and 25 - 26 days respectively.

3.3. Growth time period of Milky mushroom

The collected data of growth periods (Table 3) show that the growth time of Milky mushroom ranged from 19 to 21 days in the rainy season, and 21 to 24 days in the dry season. The growth time of Treatment 2 was faster than that of other Treatments 1 - 2 days in rainy season and 1 - 3 days in dry season. Treatment 3 has the slowest growth rate.

Table 3. Growth and development time period of Milky mushroom (days)

Treatment	Rainy season				Dry season			
	Complete mycelia in spawn	Fruiting body initiation	Mushroom fruiting body production	Harvesting	Complete mycelia in spawn	Fruiting bodies initiation	Mushroom fruiting body production	Harvesting
Treatment 1	1	8	10	20	1	10	12	22
Treatment 2	1	7	9	19	1	9	11	21
Treatment 3	1	9	11	21	1	12	14	24
Treatment 4	1	9	11	21	1	11	13	23

3.4. Growth characteristics of Milky mushroom

There are many types of culture media with different nutrient compositions that can be used for the vegetative growth of mushrooms. In this experiment, four different culture substrates were screened to determine the suitable substrate for mycelial growth of Calocybe indica. As shown in Table 4, Milky mushroom was able to grow on all four types of substrate tested.

3.4.1. Length of stalk

The descriptive dimensions of fruiting bodies and yield of Milky mushroom in different substrates were presented in Table 4.

Table 4. Length of stalk, thickness of pileus and yield of Milky mushroom

Treatment	Rainy season			Dry season		
	Length of stalk (cm)	Thickness of pileus (cm)	Biological yield (g/bag)	Length of stalk (cm)	Thickness of pileus (cm)	Biological yield (g/bag)
Treatment 1	11.99b	2.59b	571.57bc	11.93b	2.57b	478.00b
Treatment 2	13.47a	2.81a	640.93a	13.20a	2.79ab	590.40a
Treatment 3	11.79b	2.44b	563.70c	11.30b	2.33bc	421.50b
Treatment 4	13.01ab	2.61ab	600.53bc	12,90a	2.57b	485.60b
CV(%)	13.51	13.39	1.32	10.78	14.16	14.42
LSD$_{0.05}$	1.07	0.21	56.22	0.83	0.30	36.90

In a column the same letters indicate that the values are not significantly different by LSD (least significant difference)'s test at significance level of 0.05; CV (coefficient variance).

The data from Table 4 shows that the length of mushroom stalks of treatments are different and Treatment 2 has the highest stalk (13.47cm and 13.20 cm, respectively in the rainy season and dry season). The difference of the length of mushroom stem in rainy and dry seasons is not statistically significant. The length of mushroom stalk would be not affected by weather conditions.

3.4.2. Diameter of stalk

The stem of Milky mushroom has bowling pin-like shape. The diameters of stalk were thus measured at three positions of stalk (the neck, the middle and the base of the mushroom stalk). The data of stalk diameter is shown in Table 5.

Table 5. Diameter of Milky mushroom stalk (cm)

Treatment	Rainy season				Dry season			
	Stalk neck	Middle stalk	Base stalk	Mean	Stalk neck	Middle stalk	Base stalk	Mean
Treatment 1	2.25b	2.77b	3.09b	2.70ab	2.15b	2.61b	3.12b	2.62ab
Treatment 2	2.68a	3.52a	3.93a	3.38a	2.46a	3.27a	3.92a	3.22a
Treatment 3	2.21b	2.65b	3.06b	2.64ab	2.11b	2.54b	3.05b	2.56ab
Treatment 4	2.67a	3.43a	3.84a	3.26a	2.20b	2.68b	3.21b	2.70ab
CV(%)	15.18	14.80	14.84	14.98	15.20	14.50	13.05	11.77
LSD$_{0.05}$	0.24	0.23	0.34	1.01	0.22	0.25	0.27	1.11

In a column the same letters indicate that the values are not significantly different by LSD (least significant difference)'s test at significance level of 0.05; CV (coefficient variance).

The results showed that the stalk diameter of Milky mushroom cultivated in different substrates varied from 2.64 to 3.38 cm in the rainy season and from 2.56 to 3.22 cm in the dry season. The diameter of stalk is highest in Treatment 2. There is not statistically significant difference between the treatments. However, the diameter of mushrooms stalk cultivated in rainy season is larger than that in dry season. Thus, the diameter of stalk would be affected by weather and the culture substrate has little effect.

3.4.3. Thickness of mushroom pileus

The thickness of the Milky mushroom pileus in the treatment is from 2.44 to 2.81 cm in the rainy season and from 2.33 cm to 2.79 cm in the dry season. There is not significant difference of the thickness of mushroom pileus that cultivated in rainy season and dry season, but the difference of thickness of mushroom pileus of treatments has statistically significant.

3.4.4. Biological yield of Milky mushroom fruiting bodies

The biological yield of mushrooms is an important criterion which is used to evaluate the cultivation and production capacity in local culture condition. Based on the biological yield, the economic efficiency is evaluated at the end of harvest. The collected data of are presented in Table 4.

The results indicate that the highest and lowest biological yields were Treatment 2 (640.93 g/spawned bag) and Treatment 3 (421.50 g/spawned bag). The difference of biological yield of mushroom that cultivated in rainy and sunny seasons is statistically significant. Thus, the substrate composition has an influence on harvested fruiting body mass. Specifically, the substrate which is added with rice husk ash and alluvial soil has highest biological yield. In addition, the growth capacity of Milky mushroom cultivated in the rainy season is better than that in the dry season. The lower temperature and higher air humidity in rainy season could be main factors. So, the rainy season is suitable for Milky mushroom cultivation.

4. ECONOMIC EFFICIENCY

Table 6. Economic efficiency of Milky mushroom production (calculation for 1000 spawn bags)

Treatment	Production cost (1000 VND)	Rainy season			Dry season		
		Yield (kg)	Revenue (1000 VND)	Profit (1000 VND)	Yield (kg)	Revenue (1000 VND)	Profit (1000 VND)
Treatment 1	7.710	571.57	22.862	15.152	487.00	19.120	11.410
Treatment 2	7.710	640.93	25.637	17.927	590.40	23.616	15.906
Treatment 3	7.710	563.70	22.548	14.838	421.50	10.860	9.150
Treatment 4	7.710	600.53	24.021	16.311	485.60	19.424	11.714

(Current price of milky mushroom: 40.000 VND/kg)

The analysis data indicate that the cost of 1000 spawn bags is same at different treatments (7.710.000 VND). Treatment 1 has the highest profit (17.927.200 VND), followed by Treatment 4 (16.311.200 VND), Treatment 1 (15.152.000 VND) and Treatment 3 has the lowest profit (14.838.000 VND) in the rainy season cultivation. In the dry season cultivation, the highest profit reached to 15.906.000 VND at Treatment 2, then Treatment 4 (11.714.000 VND), Treatment 1 (11.410.000 VND) and Treatment 3 has the lowest profit (9.150.000 VND).

5. CONCLUSIONS

The survey results of Milky mushroom cultivation in four different substrates conclude that Milky mushroom has good resistance. The rate of spawning success of media could search to 96.7%. The substrate added 5 kg of alluvial soil and 2 kg of rice husk ash was considered to be the most suitable substrate to cultivate Milky mushroom to get the high yield and the good profit. Milky mushroom is suitable for the weather conditions in Binh Dinh province. Milky mushroom cultivation could thus realize in the duration of all year and become a livelihood for local farmers.

REFERENCES

1. A. S. Krishnamoorthy, M. T. Muthuswamy, S. Nakkeeran. Technique for commercial production of milky mushroom Calocybe indica P&C, *Indian journal of mushrooms*, **2000**, *18*, 19-23.

2. K. A. Subbiah and V. Balan. A Comprehensive Review of Tropical Milky White Mushroom (Calocybe indica P&C), *Mycobiology*, **2015**, *43*(3), 184-194.

3. N. Alam, R. Amin, A. Khan, I. Ara, M. J. Shim, M. W. Lee, T. S. Lee. Nutritional analysis of cultivated mushrooms in Bangladesh: Pleurotus ostreatus, Pleurotus sajor-caju, Pleurotus florida and Calocybe indica, *Mycobiology,* **2008**, *36*, 228-232.

4. S. Selvi, P. U. Devi, S. Suja, S. Murugan, P. Chinnaswamy. Comparison of non-enzymic antioxidant status of fresh and dried form of Pleurotus florida and Calocybe indica, *Pakistan journal of nutrition*, **2007**, *6*, 468-471.

5. S. T. Chang, Hayes WA, editors. Nutritional value. *The biology and cultivation of edible mushrooms*, Academic Press, New York, 1978, 137-165.

6. P. Mattila, K. Könkö, M. Eurola, J. M. Pihlava, J. Astola, L. Vahteristo, V. Hietaniemi, J. Kumpulainen, M. Valtonen, V. Piironen. Contents of vitamins, mineral elements, and some phenolic compounds in cultivated mushrooms, *Journal of agriculture food chemistry*, **2001**, *49,* 2343-2348.

7. Le Duy Thang. *Cultivation techniques of edible mushrooms* (Vol.1) (in Vietnamese). Agricultural Publishing House, Hanoi, 2001**.**

CONTENTS